

TECHNISCHE UNIVERSITÄT MÜNCHEN
Physik-Department E15

Quenching-Factor Measurements for Cryogenic Dark Matter Detectors

Chiara Coppi

Vollständiger Abdruck der von der Fakultät für Physik der Technischen
Universität München zur Erlangung des akademischen Grades eines

Doktors der Naturwissenschaften (Dr. rer. nat.)

genehmigten Dissertation.

Vorsitzender: Univ.-Prof. Dr. W. Weise

Prüfer der Dissertation:

1. Univ.-Prof. Dr. F. von Feilitzsch

2. Univ.-Prof. Dr. St. Paul

Die Dissertation wurde am 15.06.2009 bei der Technischen Universität
München eingereicht und durch die Fakultät für Physik am 13.07.2009
angenommen.

Abstract

During the last decade, convincing evidence for the presence of dark matter in the universe has been found. According to cosmological observations, non-baryonic dark matter accounts for 23% of the total energy-mass density of the universe. Many hypotheses on the nature of dark matter have been put forward. Presently, one of the most compelling arguments suggests that dark matter is composed of not yet identified weakly interacting massive particles (WIMPs).

The CRESST (Cryogenic Rare Event Search with Superconducting Thermometers) experiment aims at the direct detection of WIMPs via nuclear recoils. CaWO_4 single crystals are used as target material. Since the spin-independent interaction cross section of WIMPs is expected to be proportional to A^2 (where A is the mass number of the scattering nucleus) the presence of a heavy nucleus like tungsten makes CaWO_4 a particularly suitable target for the WIMP search. The expected event rate for WIMP interaction is of the order of 1 event per kg and day. To be sensitive to such a small rate, massive background reduction and discrimination is necessary. The experiment is located in the underground laboratory “Laboratori Nazionali del Gran Sasso” in Italy, with a residual muon flux of $\sim 1\mu/(m^2h)$.

In CRESST, background discrimination is achieved by the simultaneous measurement of the phonon and light signals produced by an interaction. The measurement of the two signals is performed using cryogenic techniques. Different kinds of interactions (for example electron or nuclear recoils) have different light yields. In this way electron recoil events originating from β and γ background radiation can efficiently be distinguished from possible nuclear recoil events due to WIMP interaction. Neutrons are still a serious

background since - as WIMPs - they cause nuclear recoils. However, due to kinematical reasons, neutrons mainly scatter from oxygen, whereas WIMPs are expected to mainly scatter from tungsten. The light output depends on the nuclear mass: the larger the mass, the weaker the light output. This provides a possibility to discriminate against neutron events. The parameter used to characterize the light output is the so-called quenching factor (QF). The measurements presented here were aimed at the determination of the QFs for oxygen, calcium and tungsten in CaWO_4 single crystals at mK temperatures.

To induce nuclear recoils in the CaWO_4 crystal, neutrons have been used. Neutrons have the advantage that the nuclear recoils are distributed throughout the complete volume of the crystal, so that bulk events can be produced and investigated. For the measurements of the QFs with neutrons, a new setup has been installed at the Maier-Leibnitz-Laboratorium in Garching including a dilution refrigerator to operate CRESST-like cryodetectors. In this way, cryodetectors can be irradiated with a monoenergetic 11 MeV neutron beam produced by the tandem accelerator. In addition, measurements with standard neutron sources (^{252}Cf and $^{241}\text{Am-Be}$) have been performed.

A detailed analysis of the data is presented, which gave the following values for the QFs for oxygen, calcium and tungsten:

$$\text{QF(O)} = 10 \pm 1, \quad \text{QF(Ca)} = 17.9 \pm 0.2, \quad \text{QF(W)} = 35 \begin{smallmatrix} +19 \\ -9 \end{smallmatrix}$$

These values of the QFs measured at ~ 50 mK for bulk nuclear recoils are in good agreement with values obtained previously with different measurement techniques at higher temperatures.

In addition, from a detailed study of the nuclear recoil spectrum, the value of the so-called phonon quenching was determined which accounts for the different amplitudes of the phonon signals for electron and nuclear recoil events of the same energy. It has been found that for the same recoil energy, electron recoil events have only $(92 \pm 5)\%$ of the energy of nuclear recoil events.

Contents

1	Dark Matter	1
1.1	Evidence	1
1.2	Candidates	6
1.3	Detection of Dark Matter	8
1.3.1	Indirect Detection	10
1.3.2	Direct Detection	11
1.3.2.1	Background Reduction	11
1.3.2.2	Background Discrimination	13
1.3.3	Direct Detection Experiments	14
2	CRESST	23
2.1	CRESST Detectors	23
2.2	Cryogenic Setup	27
2.3	Shielding against Background Radiation	28
2.4	Results of the CRESST-II Commissioning Run	32
3	Nuclear Quenching Factors	37
3.1	Neutron Background	37
3.2	Principle of Measurements of the Quenching Factors	41
3.2.1	Neutron Scattering with Fixed Kinematics	43
3.2.2	Ion Irradiation	44
4	Setup of the Scattering Experiment	47
4.1	Neutron Sources	47

4.1.1	Standard Neutron Sources	47
4.1.2	Expected Recoil Spectra	48
4.1.3	11 MeV Neutron Beam	52
4.2	Experimental Setup	59
4.2.1	Signal Response of the Crystal	60
4.2.2	Readout of the Signals	62
4.2.3	Phonon Detector	64
4.2.4	Light Detector	69
4.2.5	Mounting the Detector Module	71
4.2.6	Installation of the Cryostat	75
4.2.7	Data Acquisition	80
5	Measurements: Results and Discussion	83
5.1	Measurement of the Beam Profile	83
5.1.1	Profile of the Beam itself	85
5.1.2	Profile with Materials	86
5.2	Measurements with the Cryodetector	93
5.2.1	Phonon Channel	96
5.2.1.1	Pulse Shape	96
5.2.1.2	Electron Recoils	99
5.2.1.3	Nuclear Recoils	102
5.2.2	Light Channel	105
5.2.2.1	Calibration of the Light Detector	105
5.2.2.2	Electron Recoils	108
5.2.2.3	Nuclear Recoils	112
5.2.2.4	Inelastic Tungsten Recoils	114
5.3	Quenching Factors	116
5.3.1	Data Evaluation	116
5.3.2	Quenching Factors for Oxygen and Calcium	117
5.3.3	Quenching Factor for Tungsten	123
5.3.4	Overview of the Quenching-Factor Results	127
5.4	Phonon Quenching	129

<i>CONTENTS</i>	iii
6 Summary and Outlook	137
Acknowledgments	vii

Chapter 1

Dark Matter

The term “dark matter” was first used by F. Zwicky in the 1930s in relation to the observed velocities of the galaxies in the Coma cluster [1]: these velocities could only be explained by an amount of matter much larger than the visible matter of the cluster itself. The missing matter was then called “dark matter”.

Since then, more evidence for the presence of dark matter has been found. In this chapter an overview of the evidence for dark matter is given. Some of the particle candidates and of the detection experiments are described.

1.1 Evidence

The observations that point into the direction of the presence of a big amount of dark matter in the universe can be summarized as follows

- **Velocities of galaxies in clusters:**

From the observation of the velocities of galaxies in clusters came the first evidence for the presence of dark matter in the universe (Zwicky, [1]). By means of the virial theorem, that relates the kinetic energy to the potential energy of a system, the total mass of the cluster could be calculated from the measurement of the velocities of the galaxies. The comparison between the calculated mass and the luminous matter,

showed a huge discrepancy: the mass of the cluster had to be ~ 100 times the luminous mass.

More recently, observations of the X-ray emissions from galaxy clusters (not possible at the time of the observations of F. Zwicky) have revealed the presence of hot gas, the mass of which can be of the order of 10 times the luminous mass [2]. This explains part of the missing matter deduced from the virial theorem; still a mass about 10 times the visible (luminous plus gaseous (X-ray emitting)) matter is unexplained.

Moreover, the gravitational force produced by the luminous matter would not be enough to bind the hot gas to the cluster. Only with the presence of additional matter, the presence of the gas in the clusters can be explained.

The ratios between the different kinds of matter has turned out to be quite similar for all clusters observed. The mass from the stellar component contributes $\sim 1\%$ - 2% [3] to the total mass, while $\sim 5\%$ - 15% [2] [4] of the total mass consist of hot plasma.

- **Rotation curves of spiral galaxies:**

The measurements of the rotation curves of spiral galaxies provide the evidence for the presence of dark matter at galactic scales. These curves show the expected Keplerian behavior for small radii. Following the Newtonian gravity a decrease of the velocity proportional to $1/\sqrt{r}$ is expected where no significant amount of matter is present any more. This, however, is not the observed behavior. The measurements of rotation curves for most galaxies, up to the biggest measured radii, show a similar behavior: after a linear rise, the velocities reach a value of around 200 km s^{-1} and stay nearly constant up to the maximum measured radii. In Fig.1.1, an example of a measured rotation curve is shown, together with the different contributions that produce the measured curve shape.

To explain this in the frame of Newtonian gravity, it is necessary that

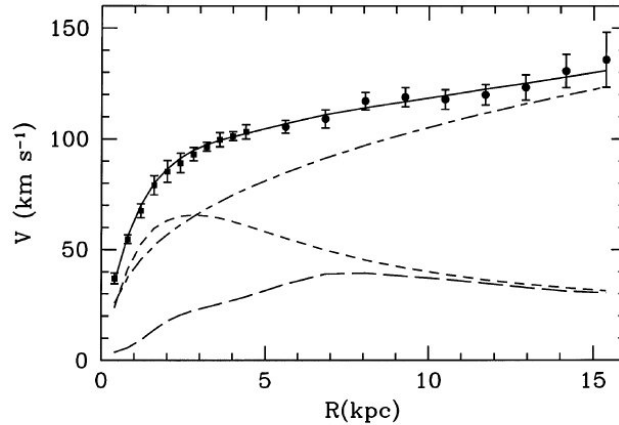


Figure 1.1: M33 rotation curve (points) compared with the best-fitting model (continuous line). Also shown are the halo contribution (dot-dashed line), the stellar disc (short-dashed line) and the gas contribution (long-dashed line) [5].

the mass extends at least up to such radii, where no visible matter is present any more. The problem would be solved by the presence of a dark matter halo surrounding the galaxy and extending much further than the luminous matter.

- **Gravitational lensing:**

The gravitational lensing is an effect that occurs when a massive object is located between the observer and the light source. In this case the light from the source is deflected by the gravitational field of the massive object, with the consequence that the image of the source is deformed or displaced. From the observation of such an effect, the mass of the object that causes the deformation can be derived. Typically, this effect can be produced by galaxy clusters: the mass derived with this method is consistent with the mass derived from the velocities of the galaxies.

- **Bullet cluster:**

All the evidences listed above have the characteristic that the gravitational center of the visible matter and the one of the dark matter

coincide. The discrepancies arise only from the difference between the gravitational force expected applying the Newtonian laws and the measured one. In the last years a very special case was observed, in which the gravitational center does not coincide with the visible matter. This is the so called “bullet cluster” [6].

Two galaxy clusters are observed, after a collision. The collision has no effect on the galaxies, the motion of which remains the same as before the collision. The dark matter is also expected not to show any consequence for the collision, given the very weak interaction cross section, so that the position after the collision is expected to coincide with that of the galaxies. The hot gaseous material of the two clusters, on the other hand, interacts strongly, and its motion is slowed down. In this way, after the collision the gas is expected to be located between the two clusters. Fig.1.2 shows the bullet cluster as it is observed. The red regions represent the gas, detected by its X-rays emissions. The blue regions represent the distribution of the gravitational force, as it is deduced from gravitational lensing. This confirms the hypothesis of the presence of an amount of dark matter, the mass of which is much higher than the mass of the gas, and that is located where the visible matter is. This, in fact, has a mass much lower than the gas, and would not explain the distribution of the gravitational force.

On a cosmological scale, the presence of dark matter is confirmed by the Cosmic Microwave Background (CMB). The CMB was first observed in 1964 and interpreted as the echo of the big bang. This background radiation has the characteristic spectrum of a black-body emission at a temperature of 2.72 K and is incredibly constant over all directions, with variations in the order of μK only. The most precise measurement of the CMB was performed by WMAP (Wilkinson Microwave Anisotropy Probe) [7] [8] of which the result is shown in Fig.1.3.

From the decomposition of the temperature anisotropies of the CMB into spherical harmonics, information on the structure of the universe can be de-



Figure 1.2: Image of the so-called bullet cluster. Two galaxy clusters are observed after a collision. The collision has no effect on the luminous matter, while the hot gas, originally bound to the clusters, is slowed down. The X-ray emitting hot gas is depicted in red in the picture. The blue regions represent the regions where - according to gravitational lensing - the gravitational force is concentrated. These regions do not coincide with the distribution of the gas but with that of the luminous matter. Since the mass of the gas is much higher than that of the luminous matter, such a distribution of the gravitational force can only be explained with the presence of dark matter, the distribution of which coincides with that of the luminous matter.

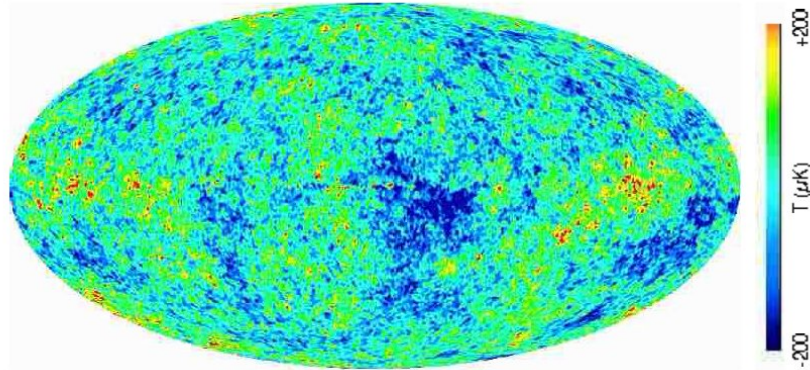


Figure 1.3: Map of the anisotropy of the cosmic microwave background, measured by WMAP [7].

duced. The observed spectrum is best reproduced by the so called Λ CDM model, which describes a universe dominated by dark energy (cosmological constant Λ) and by cold dark matter (CDM). According to this model, the dark energy accounts for $\sim 73\%$ of the total density of the universe. The total density of matter is $\Omega_m h^2 = 0.128 \pm 0.0008$, where h is the reduced Hubble expansion parameter $h = H_0/100 = (0.73 \pm 0.03) \text{ Mpc}^{-1} \text{ km s}^{-1}$. The abundance of baryons is only $\Omega_b h^2 = 0.0223 \pm 0.0007$ [8]. The difference between Ω_m and Ω_b indicates that most of the dark matter has to be non baryonic.

1.2 Candidates

The presence of dark matter in the universe has been confirmed by several observations and at several scales. It is not yet clear, however, what this dark matter consists of.

As mentioned, from the analysis of the CMB, we know that most of the dark matter has to be non baryonic. If dark matter consists of particles, their stability or long lifetime is also necessary, to allow their actual presence in the universe. The kind of interaction between the dark matter particles

themselves and the baryonic matter has to be very weak, to explain the difficulty of their detection.

Searching for a dark matter particle among the known particles, the neutrino appears to be the only possible candidate. This is the only particle, in the standard model, that is stable, neutral and weakly interacting. Neutrinos, however, are very light ($m_\nu \lesssim 2.3 \text{ eV}$ [9]) and, as a consequence, relativistic, and if they would be the only particle to contribute to dark matter, the structures observed in the universe could not have formed. From the CMB the limit on the relic density of neutrinos is set at $\Omega_\nu h^2 < 0.0067$.

Another possible candidate as dark matter particle are the axions. These particles have been suggested to solve the CP problem in QCD. They are predicted to be very light ($m_a \lesssim 10^{-2} \text{ eV}/c^2$) and very weakly interacting. The CAST (CERN Axion Solar Telescope) experiment is one of the experiments that try to detect axions [10] [11]. Differently as for the case of neutrinos, the axions could constitute the main part of dark matter in spite of their small mass, because they were never in thermal equilibrium in the early universe [12].

Assuming that the dark matter particles were in thermal equilibrium at the time of the radiation-matter decoupling, they must have been heavy enough not to be relativistic at this time. The time of the decoupling, in fact, corresponds to the moment of the formation of the structures in the universe. If the matter would have been dominated by relativistic particles, such structures would have been smeared out. This unknown dark matter particle is called WIMP (Weakly Interacting Massive Particle).

One of the candidates as WIMP is the neutralino. The neutralino is a particle predicted by the theory of Supersymmetry, in the frame of the Minimal Supersymmetric Standard Model (MSSM). In this model, to each standard model particle a partner particle is associated (called superpartner or sparticle), the spin of the sparticle differing from the spin of the particle by $1/2$.

The R-parity distinguishes standard model particles ($R = 0$) from su-

persymmetric particles ($R = 1$). The conservation of the R-parity prevents supersymmetric particles from decaying into standard-model particles. For this reason, the lightest supersymmetric particle (LSP) is stable.

Four neutralinos are predicted, as superpositions of the supersymmetric partners of the standard-model photon, Z^0 , and the two neutral higgs bosons. The lightest neutralino is usually denoted as χ . If the LSP corresponds to the lightest neutralino, this particle would be a good candidate for a dark matter particle.

In the frame of the constrained MSSM (CMSSM), constraints on the mass and interaction cross section of the neutralino are given. A possible parameter plot for the neutralino is shown in Fig.1.4. In this plot the logarithm of the spin independent interaction cross section of the neutralino with the proton is plotted versus the neutralino mass. Other models give different ranges for the parameters, for example with the mass extending to lower values.

A possible way to detect neutralinos is via direct interaction with a target (see section 1.3.2). Another possibility is by detecting annihilation products: since neutralinos are Majorana particles, they can self-annihilate. This process is more probable where the concentration of WIMPs is large. The search of products of annihilation of WIMPs is at the base of the indirect detection experiments, described in section 1.3.1.

Still remaining in the frame of the MSSM, the neutralino is not the only possible candidate as WIMP. For example, the LSP could also be the gravitino (partner of the graviton). Since this particle would only interact gravitationally, the direct detection would be very difficult.

1.3 Detection of Dark Matter

According to the observations described, dark matter particles are expected to be present in our galaxy. It should be possible to detect them with both direct detection experiments, or by indirect detection methods.

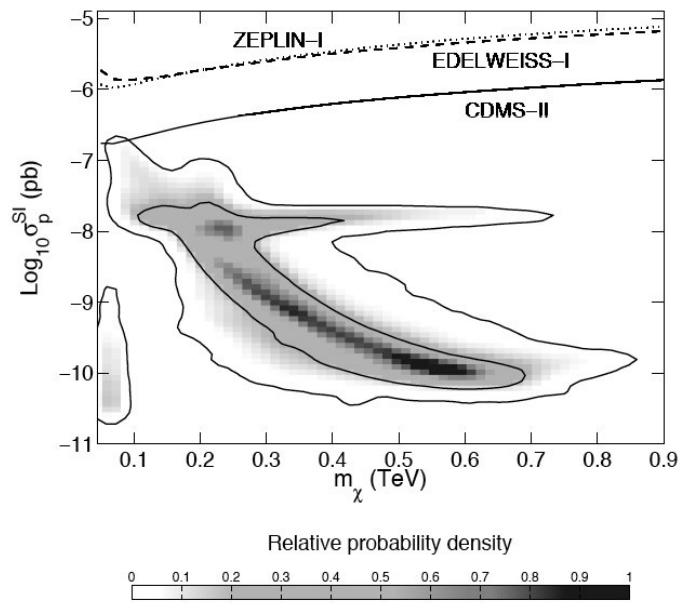


Figure 1.4: Constraints according to the CMSSM for the mass and the cross section for spin-independent interaction of the neutralino with the proton [13]. Exclusion curves obtained from the experiments ZEPLIN-I [14], EDELWEISS-I [15] and CDMS-II [16] are also shown.

1.3.1 Indirect Detection

One possibility to prove the existence of WIMPs and to investigate their characteristics, is to look for their annihilation products. The neutralino (one of the most probable candidates as dark matter particle, see section 1.2) is a Majorana particle, so that it can self-annihilate.

The annihilation process is favored in regions where the density of WIMPs is higher, like for example the center of the galaxy or the center of the sun, where WIMPs can be trapped due to gravitation. Products of the annihilation can be high-energy γ rays, neutrinos, positrons or antiprotons.

Several experiments are devoted to the detection of the products of annihilation of WIMPs. For the detection of high-energy γ s, both space telescopes and ground-based telescopes are used. In this second case, the γ rays cannot be detected directly, since they do not reach the ground, but secondary particles can be detected. Examples of such ground based experiments are MAGIC, a 17 m imaging air Cerenkov telescope situated on the island La Palma [17], CANGAROO-III, an array of four 10 m Cerenkov telescopes, situated in Woomera, Australia [18] and HESS, consisting of four 12 m diameter Cerenkov telescopes, situated in the Gamsberg area of Namibia [19].

Space telescopes, on the other hand, can directly detect the high-energy γ s. To this kind of experiments belongs EGRET (Energetic Gamma-Ray Experiment Telescope) [20] that has recently measured a signal that possibly can be attributed to WIMP annihilation [21].

The detection of positrons and antiprotons is only possible with space telescopes. The PAMELA (a Payload for Antimatter Matter Exploration and Light-nuclei Astrophysics) experiment is one of these, and has measured an abundance of positrons [22]. Positrons can be produced by the interaction of cosmic-ray nuclei and atoms in the interstellar medium (secondary source). The abundance measured by PAMELA, however, is not in agreement with the expectation of such secondary positrons, and would require a primary source. Such primary sources can be objects like pulsars, microquasars, but also WIMP annihilation. In [22] the results are described and discussed in

detail.

1.3.2 Direct Detection

Another possibility to detect Dark Matter particles is via the direct interaction of WIMPs in a target material producing nuclear recoils. The mass of WIMPs is expected to be in the range of 10-1000 GeV. Given the average velocity of WIMPs, $\bar{v} = 270$ km/s, calculated from the assumption that the WIMPs that can be detected are gravitationally trapped in our galaxy, the recoil energy produced by the scattering of a WIMP by a nucleus is in the range of some tens of keV.

The target can be optimized on the basis of the expected characteristics of WIMPs. Two kinds of interactions of WIMPs with nuclei are expected. The spin-dependent interaction is proportional to $J(J+1)$, where J is the nuclear spin. To enhance the cross section for this kind of interaction a target material containing a nucleus with high spin is favorable, e.g. iodine.

A spin independent interaction is also possible. In this case the interaction is coherent, with the consequence that the interaction cross section is proportional to A^2 , where A is the mass number of the interacting nucleus. In this case materials containing heavy nuclei are preferred (e.g. tungsten, xenon)

1.3.2.1 Background Reduction

To detect a rare WIMP event rate of typically 1 event per kg-day, a massive background reduction is needed. On the surface of the earth, the cosmic radiation represents an important source of background. It consists of hadrons and leptons produced by the interaction of high energetic particles with the atmosphere.

To reduce the background due to cosmic radiation, low-background experiments like the ones dedicated to the dark matter search are performed in underground facilities. There are several underground laboratories around the world. The depth of the laboratories is usually given in meters water

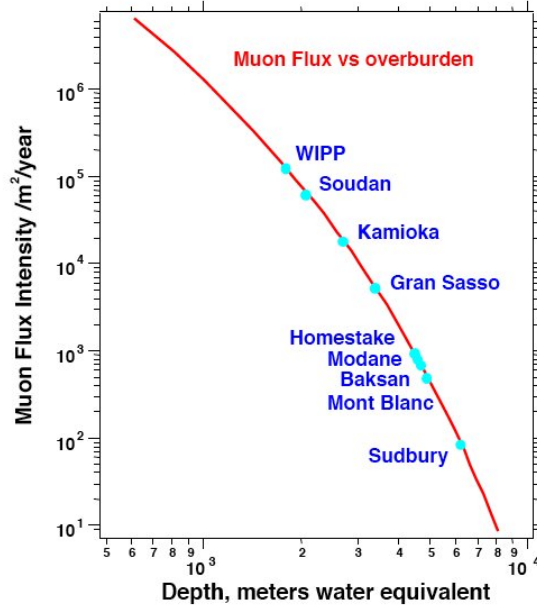


Figure 1.5: Plot of the muon flux as a function of the depth in m.w.e. The depth of some important underground laboratories is also shown [23].

equivalent (m.w.e.): 1 m of standard rock corresponds to about 3 m of water. Of the cosmic particles that reach the earth, muons are the most difficult to shield, due to their high penetration capability. A few meters of rock are sufficient to shield the hadronic component of the radiation completely, but thousands of m.w.e. are needed to reduce the flux of muons significantly. In Fig.1.5 the muon flux ($m^{-2}y^{-1}$) is plotted as a function of the depth (in m.w.e). In the same plot, the depth (and consequently the residual muon flux) of some of the most important underground laboratories in the world is shown.

An additional component of the background is due to the radioactive elements contained in the rocks. In order to reduce this background the experiments are surrounded by shielding materials of different kinds, depending on the characteristics of the experiment itself. For example lead and copper are used as shielding for γ radioactivity. If possible, antique lead, for example from Roman lead bricks, is used, because it contains a lower amount of

^{210}Pb . Light materials like polyethylene, on the other hand, can be used to shield against neutrons. Besides the passive shielding, a muon veto is used in some cases. The arrival of a muon is detected by the veto, allowing to reject events eventually produced by a muon itself or by secondary neutrons. In section 2.3, a detailed description of the shielding of the CRESST experiment is given.

A critical issue remain all the materials which are present in the vicinity of the detectors, that must carefully be selected in terms of radiopurity. The parts of the setup for which the choice of the material cannot be controlled easily (for example the cryostat in the case of an experiment like CRESST or CDMS), are usually kept outside of the shielding.

1.3.2.2 Background Discrimination

Since residual radioactivity cannot be suppressed completely, which is mostly due to residual impurities in the materials surrounding the detectors, an active method of rejection has to be introduced. The residual activity is mainly γ and β radioactivity, which produces electron recoil events in a given target material. On the other hand WIMPs are expected to produce nuclear recoils. Many experiments aimed at the direct detection of WIMPs are now able to distinguish between electron-recoil events and nuclear-recoil events and can therefore discriminate γ and β background. There are several methods used for this discrimination, in most cases based on the simultaneous measurement of two different signals produced by the interaction of a particle in the target material.

The interaction of a particle with a material can produce different kinds of signals depending on the characteristics of the material, for example light in a scintillating material, ionization in a semiconductor, or heat. In some cases more than one of these quantities occur simultaneously, and the way how the energy deposited by the interacting particle is distributed between the different channels (light, ionization, heat) depends on the kind of interaction. For example, it is well known that in most scintillators the amount of light

produced by a nuclear recoil of a certain energy is smaller than the amount of light produced by an electron recoil of the same energy. The amount of energy which does not contribute to the production of light is converted into heat, so if one simultaneously measures the light and the heat produced by an interaction, the discrimination between electron recoils and nuclear recoils is possible, as well as the reconstruction of the energy of the interaction.

The case of detectors based on semiconductors is similar. Here the ionization signal is normally used for the detection, but, similarly to the case of the scintillation, also the amplitude of the ionization signal is smaller for nuclear recoil events. As for the case of scintillators, the measurement of an additional heat signal also allows to reconstruct the energy of the event and to discriminate the kind of interaction.

With detectors using noble gases as target material, the discrimination of the background can be achieved by measuring simultaneously the light and the ionization signal. Also in this case the amplitude of the signals changes for different kinds of events.

1.3.3 Direct Detection Experiments

If one of the measured signals is the heat signal, cryogenic techniques are required. Experiments of this kind are CRESST, EDELWEISS and CDMS.

- **CRESST** (Cryogenic Rare Event Search with Superconducting Thermometers) uses CaWO_4 scintillating crystals as target material. The scintillation light is read out together with the heat signal. In chapter 2 the CRESST experiment will be described in detail. Another phonon-scintillation experiment is ROSEBUD [24].
- The **EDELWEISS** (Expérience pour Détecter les WIMPs en Site Souterrain) detectors [25] consist of Ge cylinders of 70 mm diameter and 20 mm height. The ionization produced by an interaction is read out by means of electrodes placed on the two faces of the crystal. The heat signal is measured by a Neutron Transmutation Doped germanium

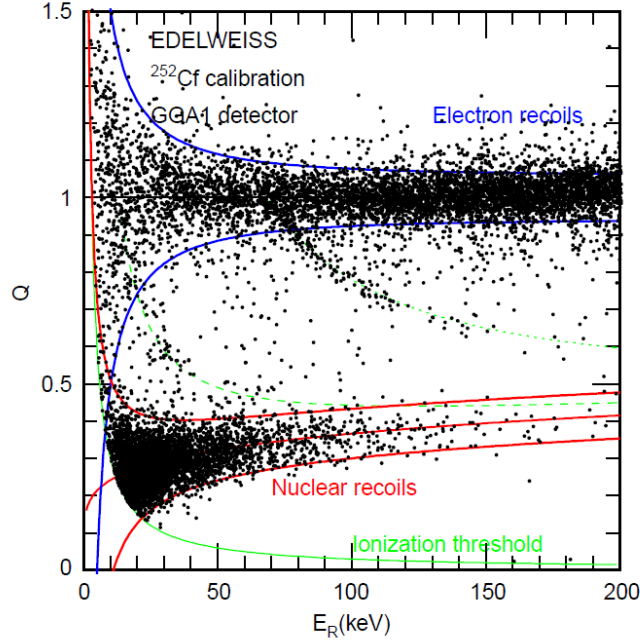


Figure 1.6: Discrimination plot obtained with EDELWEISS detectors [25]. Data of a measurement with a ^{252}Cf source are plotted. The variable Q on the y axis is defined as the ratio of the ionization signal and the deposited energy, and is normalized to 1 for electron recoil events. The thick lines represent the 90% nuclear (red lines) and electron (blue line) recoil events zones. The green line corresponds to the ionization threshold curve ($E_I = 3.5$ keV $_{ee}$ in this case). The dashed lines show where events associated with the inelastic scattering of neutrons on ^{73}Ge (13.26 and 68.75 keV excited levels) are expected in this plane. Further details are given in [25].

crystal (NTD) glued onto the absorber crystal. In Fig.1.6 a discrimination plot obtained with an EDELWEISS detector is shown. The plotted data were recorded by irradiating the detector with a ^{252}Cf source emitting neutrons and γ s.

In the first phase of the experiment (EDELWEISS-I) three target crystals were mounted in the cryostat, (~ 30 mK). The cryostat was located in the underground laboratory Laboratoire Souterrain de Modane (LSM) in the Fréjus tunnel. The shielding of this laboratory corresponds to 4800 m.w.e. Lead (10 cm) and copper (15 cm) provided shielding

against the gamma background. As neutron moderator, 30 cm of paraffin was present. In this configuration the experiment was run from 2000 to 2003, and an exposure of 62 kg-days was collected [15]. The best upper limit (90% C.L.) for the WIMP-nucleon cross section obtained from this data was at $\sim 1.5 \cdot 10^{-6}$ pb for WIMP masses around 80 GeV (see Fig.1.7).

After this first phase, the EDELWEISS experiment was upgraded with the installation of a new cryostat, where up to 100 detector crystals can be accommodated. A new type of detector has been developed in order to improve the rejection of surface events - “interdigit detectors” [26]. The neutron shielding was also improved, and a muon veto installed. In this configuration, EDELWEISS-II aims at a sensitivity in the range of a few 10^{-8} pb for the WIMP-nucleon cross section.

- Among the experiments that use cryogenic detectors, **CDMS** (Cryogenic Dark Matter Search) [27] at the moment provides the best limits for WIMP-nucleon interaction ($\sigma_0 < 4.6 \cdot 10^{-8}$ pb for a WIMP mass of 60 GeV). The experiment is located in the Soudan Underground Laboratory in Minnesota (2090 m.w.e.). As target material, silicon and germanium are used, and the background discrimination is achieved by the simultaneous measurement of ionization and heat. The detectors have the shape of a disk with 7.6 cm diameter and 1 cm height. Concentric electrodes for the collection of the charge are on one of the flat surfaces of the disc. On the other flat surface, transition edge sensors with aluminum phonon collectors are sputtered for the measurement of the heat signal. The operating temperature of the CDMS detectors is ~ 50 mK.

The discrimination is obtained by determining the ratio between the ionization signal and the phonon signal. The most recent data of the CDMS experiment were collected in the period from October 2006 to July 2007. In Fig.1.7 the limits obtained by the analysis of the data col-

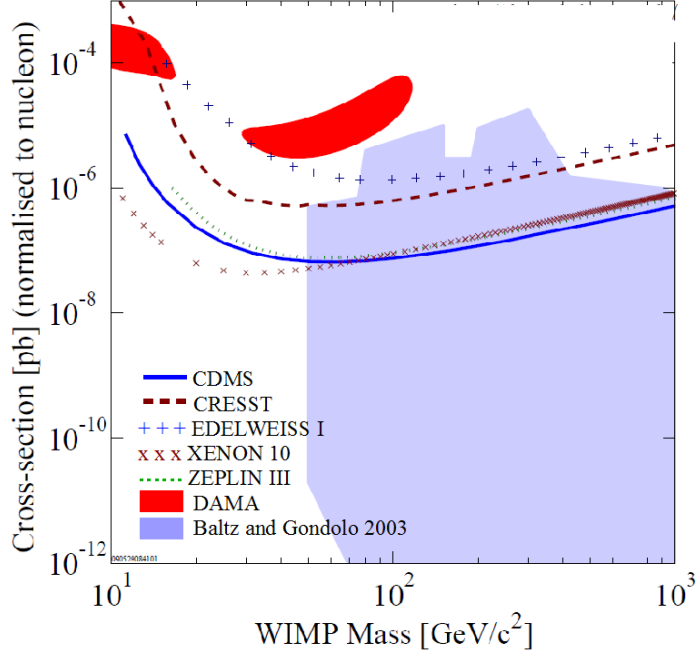


Figure 1.7: Exclusion plot for coherent spin-independent cross section. Limits from some of the direct detection experiments are plotted. CRESST-II [28], EDELWEISS [15] and CDMS [27] use cryodetectors. XENON [29], WARP [30], ZEPLIN-III [31] use liquid noble gases as target. DAMA (NaI detectors) claims a positive evidence [32] [33]. The range predicted by some supersymmetric models [34] is also shown.

lected in this time period by 15 germanium detectors are shown in [27].

Another category of experiments that perform background discrimination by means of the simultaneous measurement of two signals, is provided by experiments that use liquid noble gases as target material. Experiments of this kind are, for example, WARP [35] using liquid argon, as well as ZEPLIN [36] and XENON [29] that use liquid xenon. In these cases, the two measured signals are the scintillation light and the ionization. The quenching of the ionization for nuclear recoil events allows the background discrimination.

In comparison to experiments like CDMS, EDELWEISS and CRESST, with operating temperatures of the detectors in the mK range, the noble gas

experiments have the advantage of a much higher operating temperature (in the region of liquid nitrogen temperature). For this reason it is much easier to scale up the present experiments to a big target mass. On the other hand, the discrimination between electron recoil and nuclear recoil events is not as good as for the cryodetectors described above: the two populations of events overlap, and not all nuclear recoil events can be identified unambiguously.

As an example, the XENON experiment will be described here. The experiment is based on a two-phases time-projection chamber. Liquid xenon is the target material. An interaction produces scintillation light and free charges. The light is detected by photomultipliers (signal S_1) located at the bottom of the detector, while the charge is drifted, by an electric field, in the gas phase. Here the charge produces a second light signal (S_2), detected by an array of photomultipliers located at the top. From the detection of the first light signal (the one generated in the liquid xenon) it is possible to reconstruct the lateral position of the interaction. The delay of the second signal gives the information on the vertical position. This three dimensional reconstruction of the position of the interaction allows the definition of a fiducial volume, for the rejection of events produced by γ quanta from the environment.

The discrimination is achieved by taking the ratio S_2/S_1 of the two light signals. In Fig.1.8, the results of a measurement performed by irradiating the XENON detector with a γ source (top panel) and with a neutron source (bottom panel) are shown. Part of the events from the two kinds of recoils overlap, so that for the background discrimination, only the events belonging to the lower part of the nuclear recoil band can be considered as possible WIMP candidates.

A prototype detector (XENON10) with 15 kg of xenon was operated in the Gran Sasso underground laboratory during winter 2006-2007. 41 photomultipliers were located at the bottom of the liquid phase, for the collection of the primary scintillation light, 48 on top of the gas phase, for the collection of the secondary light signal. The charge was drifted by an electric field of

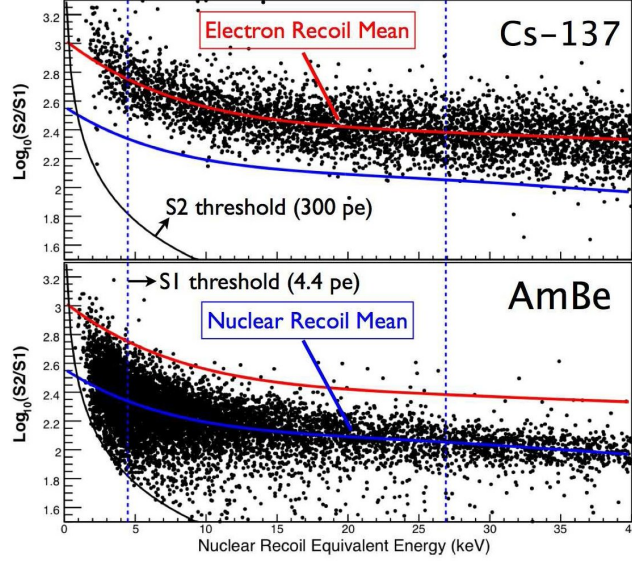


Figure 1.8: $\text{Log}_{10}(S2/S1)$ as a function of energy for electron recoils (top) and nuclear recoils (bottom) from calibration data. The solid (colored) lines are the mean $\text{Log}_{10}(S2/S1)$ values of the electron recoil (upper, red) and nuclear recoil (lower, blue) bands. The region between the two vertical dashed lines is the energy window (4.5 - 26.9 keV nuclear recoil equivalent energy) chosen for the WIMP search [29].

0.73 kV/cm. After the fiducial volume cut, a total mass of 5.4 kg was left, for a collection time of 58.6 days. The upper limit for the spin independent WIMP-nucleon cross section obtained with this measurement is $5.2 \cdot 10^{-8}$ pb for a WIMP mass of 30 GeV and is shown in Fig.1.7.

A different detection concept is used by the DAMA/LIBRA [32] [33] experiment. The target material is highly radiopure NaI. The scintillation light is collected by photomultipliers. A module is composed of a 10 kg NaI scintillating crystal coupled to two photomultipliers.

The basic difference between this experiment and those described before is that in this case no background discrimination is possible. However, the large target mass (~ 100 kg for DAMA/NaI [32] and ~ 250 kg for DAMA/LIBRA

[33]) allows the DAMA experiment to look for an annual modulation of the count rate due to the motion of the earth around the sun. The velocity of the earth relative to the WIMP halo is given by the sum of the velocity of the sun in the galactic plane and the velocity of the earth relative to the sun. As a consequence of the rotation of the earth around the sun, its velocity relative to the WIMP halo changes during the year (in particular, this relative velocity is maximum in June and minimum in December). The expected count rate for WIMPs hitting a target material on the earth, will consequently change on an annual basis.

Given the spin of iodine, the DAMA experiment differs from the experiments described previously also because it is sensitive to the spin-dependent WIMP-nucleon interaction.

In the first phase of the experiment (called DAMA/NaI), 10 NaI modules were operated, with a total target mass of ~ 100 kg. With this configuration, events were collected over a period of 7 years, for a total exposure of 107.8 t d. Later the setup was upgraded and 25 modules were installed. The new experiment, called DAMA/LIBRA is still collecting data. The results of the first 4 annual cycles are described in [33]. In Fig.1.9 the annual modulation observed by DAMA/NaI and DAMA-LIBRA are reported together. The interpretation of these results in terms of WIMP mass and cross section (spin dependent and spin independent) is not trivial and is discussed in detail in [33]. In table 6 of [33] possible WIMP masses and WIMP-nucleon cross sections are listed. Two different mass ranges are compatible with the signal observed: a heavy particle (15-120 GeV) or a light particle (28-100 MeV).

According to the theory, the present experiments are scanning only a small part of the parameter space of the neutralino (see Fig.1.7). To improve the limits and reach a sensitivity of $\sim 10^{-10}$ pb, it is necessary to increase the target mass and to reduce the background to a maximum of ~ 30 events/ton/year. Different experiments, based on the background discrimination techniques described, are planning to scale up to the ton mass range.

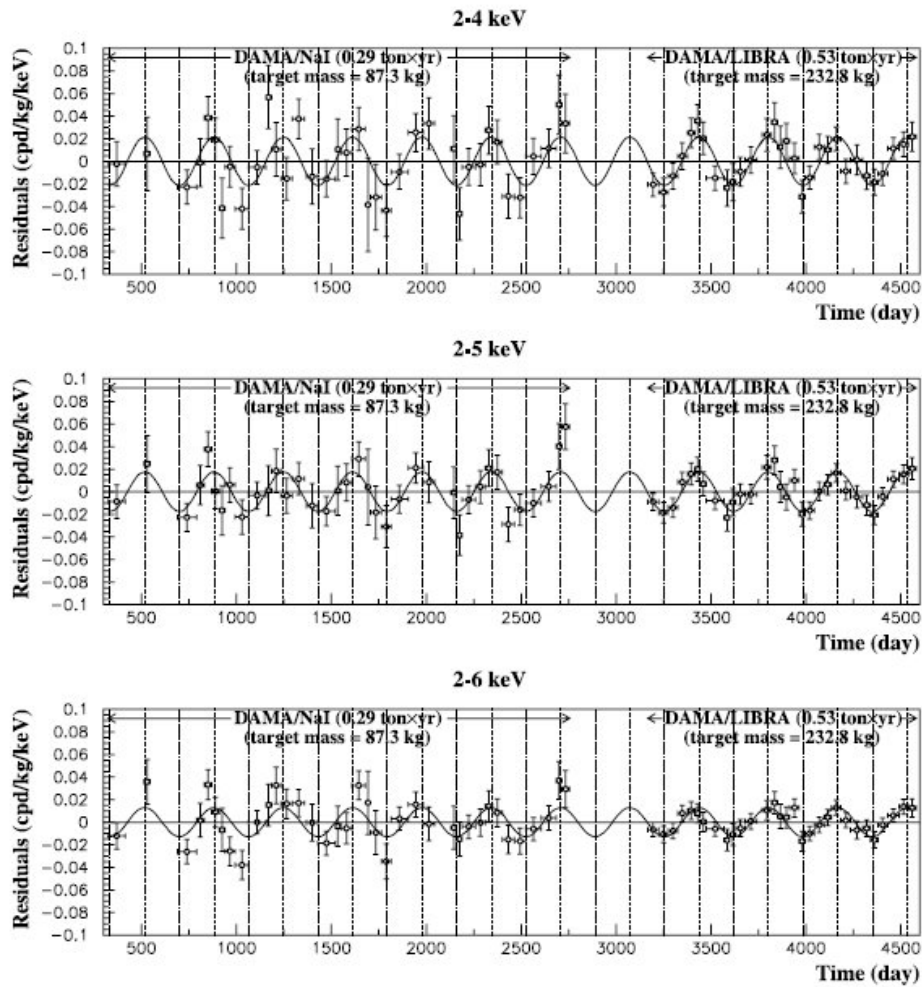


Figure 1.9: Annual modulation measured by the DAMA/NaI and the DAMA-LIBRA experiments [33].

EURECA [37] [38] [39] is a project in which the European cryogenic experiments (CRESST, EDELWEISS and ROSEBUD) are working together. The different techniques developed by these experiments will be used for a total target mass in the order of one ton, achieved with different target materials. The CDMS collaboration is also planning to improve the experiment by moving to a deeper laboratory (SNOLab, 6000 m.w.e.) and increase the mass up to ~ 1 ton (superCDMS, [40] [41]). In the frame of liquid noble gases experiments, the projects ArDM [42] and XENON-1000 [43] aim also to ton-scale target mass.

Chapter 2

CRESST

CRESST (Cryogenic Rare Event Search with Superconducting Thermometers) is an experiment for the direct detection of WIMPs. The CRESST experiment is situated in Hall A of the “Laboratori Nazionali del Gran Sasso” (LNGS) in Italy [44] [45] [28]. This underground laboratory has a shielding of 3500 m.w.e. that reduces the muon flux at sea level to a residual flux of $\sim 1 \mu/m^2h$ (see Fig.1.5, [23])

As mentioned in section 1.3.2, WIMPs are expected to interact with matter by nuclear recoils. Two kinds of interaction of WIMPs with matter are expected: a spin-dependent interaction where the cross section increases with the nuclear spin and a spin-independent interaction, the cross section of which is expected to be proportional to A^2 (where A is the atomic mass number of the interacting nucleus).

2.1 CRESST Detectors

In the CRESST-II experiment, CaWO_4 single crystals are used as target material [46]. The presence of a heavy nucleus (tungsten, $A = 182 - 186$) makes this material a well suited target for spin independent interaction of WIMPs. On the other hand, none of the nuclei present in the detector have a high nuclear spin, so that the spin dependent interaction cannot be investigated.

With the CRESST detectors a background discrimination is possible. As seen in the previous section, most of the residual background consists of γ and β radioactivity from the materials surrounding the detectors. This produces electron recoils in the crystal, while WIMPs are expected to produce nuclear recoils. In section 1.3.2.2 some of the background discrimination techniques used in direct-detection experiments are illustrated, mostly based on the simultaneous detection of different kinds of signals produced by an interaction.

In the case of CRESST the discrimination is based on the simultaneous measurement of a light signal and a phonon signal. CaWO_4 single crystals, in fact, have scintillation properties and by the interaction of a particle with the crystal, part of the energy released is converted into light. The amount of energy converted into light depends on the kind of interaction that takes place. The maximum light output is obtained for electron recoil events for which $\sim 5\%$ of the energy is converted into light (see [47] and section 5.4). The energy that is not converted into light produces quantized vibrations of the crystal lattice (phonons).

For the measurement of the phonon signal, cryogenic techniques are needed. The phonon signal is a heat signal, which can be measured calorimetrically. To have a measurable increase in the temperature, the heat capacity must be kept as low as possible ($\Delta T = \Delta E/C$, with C being the heat capacity of the system). For the case of a dielectric material, like the CaWO_4 crystal, the heat capacity decreases with the temperature following equation 2.1, where Θ_D is the Debye temperature.

$$C \propto \left(\frac{T}{\Theta_D} \right)^3 \quad (2.1)$$

The heat capacity can then be reduced by decreasing the temperature of the system. The operating temperature of the CRESST detectors is some tens of millikelvin, where a high sensitivity can be achieved.

The phonons produced by the interaction are collected by a transition edge sensor (TES) evaporated onto the crystal. The TES is a superconduct-

ing film (α phase tungsten, in the case of CRESST) of which the temperature is stabilized within the transition region between the normal and superconducting state ($T_C \sim 15$ mK). If this transition is steep, a small change in temperature results in a measurable change of the film's resistance. In the following, the CaWO_4 crystal with the TES is called phonon detector.

For the detection of the scintillation light, also a cryogenic light detector is used. This consists of a silicon on sapphire substrate that absorbs the photons emitted by the CaWO_4 crystal and converts them into phonons. The phonons are then collected by a tungsten TES, like the one used for the phonon detector.

The whole detector is surrounded by a reflective and scintillating foil. The aim of the reflective foil is to reflect the scintillation light to allow its efficient collection by the light detector. A foil is chosen that also has scintillation properties, to help in the discrimination of events produced by radioactive impurities on the surface of the CaWO_4 crystal. Such impurities are mainly due to polonium, a member of the radon decay chain, that decays by emission of an α particle. In 50% of the cases of such a decay on the surface of the detector, the α particle escapes the crystal, and the recoiling nucleus produces an event that can mimics a tungsten recoil. The α particle that escapes the crystal has a high probability to hit the foil that covers the inner part of the detector. Since this foil is also scintillating, being hit by the α particle, it will produce additional light that will also be collected by the light detector, shifting the event out of the nuclear recoil band [48] [49].

In Fig.2.1 a schematic drawing of the detector is shown. Further details of the detectors are given in [45], [28].

Since by far most of the energy of the interaction (95% or more) goes into the production of phonons, the measurement of the phonon signal, in good approximation, gives the information on the total energy of the interaction. Given the phonon energy, the amplitude of the light signal depends on the kind of interaction (electron or nuclear recoil). In a plot of the light amplitude versus the phonon amplitude, different kinds of signals form separated bands

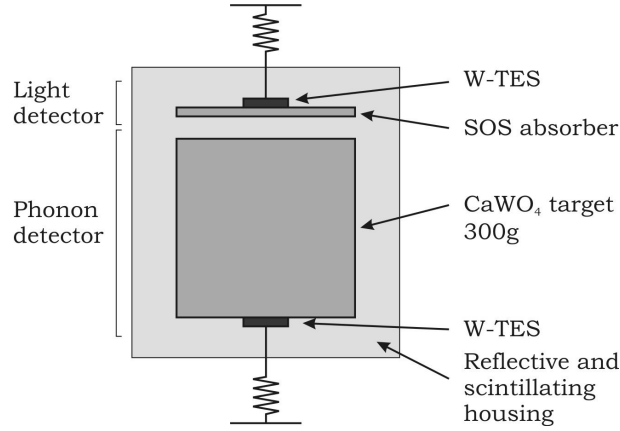


Figure 2.1: Schematic drawing of a CRESST detector module. The phonon detector is composed of a CaWO_4 crystal on which a tungsten TES is evaporated. The light detector, on top in the drawing, is composed of a silicon on sapphire (SOS) absorber with a tungsten TES. A reflective and scintillating foil surrounds the detector, for an efficient collection of the scintillation light and for the discrimination of heavy decaying nuclei on the surface of the crystal.

characterized by the light yield (Y). This is defined as the ratio between the amplitude of the light signal and the amplitude of the phonon signal (see section 4.2.1). The quantity Y is, in first approximation, independent of the energy, so that in a plot of yield versus phonon amplitude the two bands (electron recoil and nuclear recoil) are horizontal. In Fig.2.2, the yield-phonon plot for a measurement performed in CRESST with a neutron source, is shown [28]. The upper band (higher light yield) is the electron recoil band, the lower band is the nuclear recoil band. The light channel is calibrated in energy with the γ line at 122 keV from ^{57}Co [50]. The linearity of the light detector is verified with the help of heater pulses. In this way the light yield is set to 1 at 122 keV. At other energies the value of the light yield can be different because it depends slightly on the energy. In order to characterize the light output of the different kinds of interactions (electron recoils, α , nuclear recoils, but also recoils on different nuclei) the quenching factor (QF) is often used. It is defined as $1/Y$.

To neglect the difference in the amplitude of the phonon signal for elec-

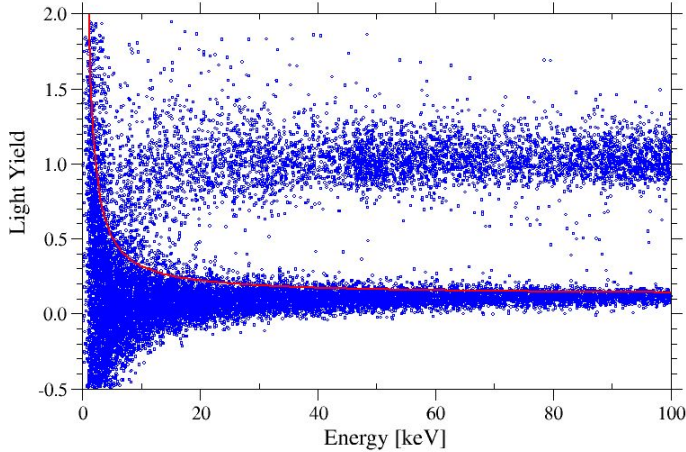


Figure 2.2: Plot of the light yield versus the phonon amplitude for a neutron calibration measurement [28]. The upper band is the electron recoil band, the lower band collects the nuclear recoil events produced by the neutrons. The red line represents the threshold below which 90% of the oxygen recoils are expected.

tron and nuclear recoils, respectively, due to the different amount of energy converted into light is correct only in first approximation. In section 5.4 it will be shown how to evaluate and to correct the error done in this way.

2.2 Cryogenic Setup

In order to cool the CRESST detectors to their operating temperature, a dilution refrigerator is required. The cryostat used for the CRESST experiment reaches a base temperature of ~ 10 mK. In a low-background experiment like CRESST it is crucial to choose radiopure materials for the surrounding of the detectors in order to reduce the background as much as possible. On the other hand, in the case of a device like a cryostat it is unavoidable to use materials that have radioactive contaminations. The only possibility to avoid that the radioactivity of the material increases the background, is to introduce a shielding between the “dirty parts” and the detectors. In Fig 2.3

a drawing of the setup of CRESST is shown [28].

In CRESST, the separation between the dilution unit and the detectors is achieved by introducing a cold finger. The cold finger is made of copper and is thermally coupled to the dilution unit. The detector holder is located at the lower end of the cold finger (about 1.5 m below the mixing chamber). In this way, it is possible to put clean shielding materials (lead and copper) all around the detector volume (see Fig 2.3).

The detector holder presently mounted in the cryostat can hold up to 33 detector modules each consisting of a cylindrical CaWO_4 single crystal of 4 cm diameter, 4 cm height, a weight of ~ 300 g, and a separate light detector. Thus the maximum total amount of target material is ~ 10 kg. The holder is made of low-background copper, electropolished to avoid surface contaminations. In Fig.2.4 the detector holder is shown.

The thermal coupling of the detector holder to the cold finger is relatively weak. In this way, rapid temperature variations of the cryostat are filtered out, and the temperature of the detector holder is more stable. The detector holder is surrounded by several thermal radiation shields thermally coupled to the different temperature stages of the cryostat.

For the readout of the signal from the TES a SQUID (Superconducting Quantum Interference Device) is needed [51]. The operation of 33 detector modules requires 66 SQUIDs. The operating temperature of the SQUIDs is ~ 4.2 K. In order to avoid too high a thermal load on the dilution unit, they are placed directly in the helium bath.

To avoid electromagnetic interferences from the environment, the cryostat and the readout electronics are placed inside a Faraday cage.

2.3 Shielding against Background Radiation

As explained in section 1.3.2.2 shielding is needed to prevent ambient radioactivity from reaching the detectors. In CRESST II several kinds of shielding are present to reduce the background events [28].

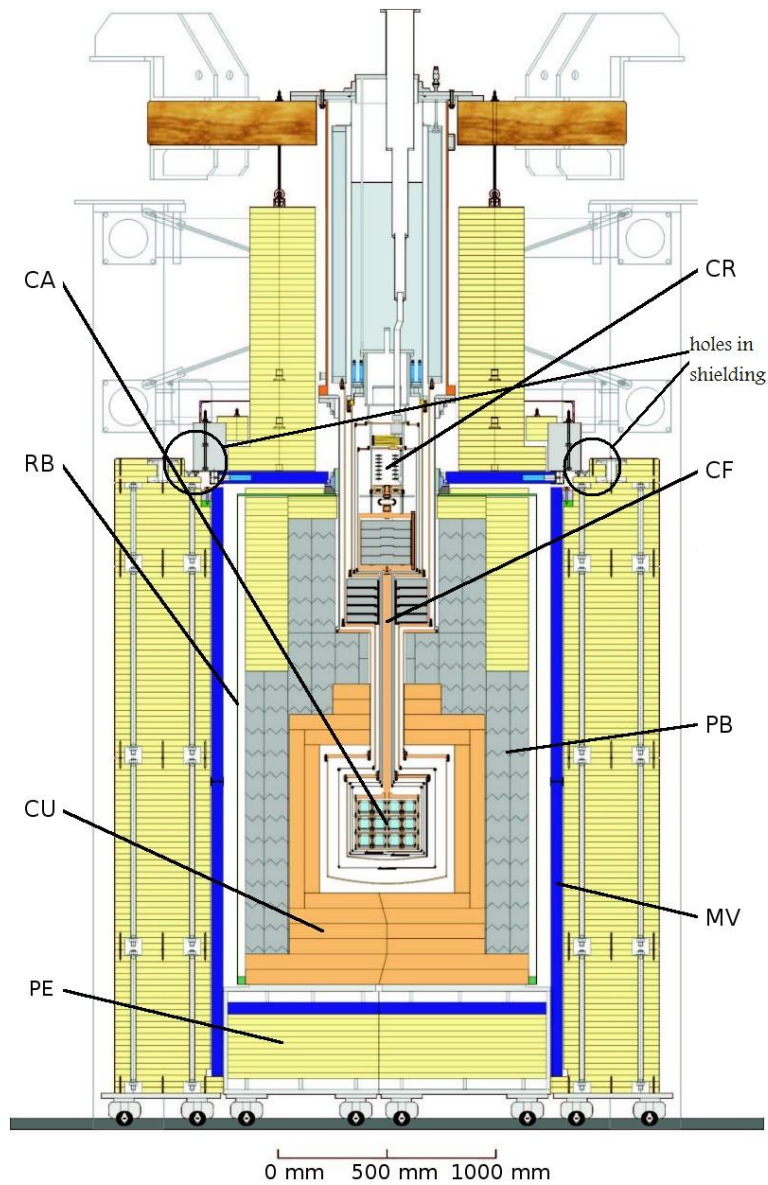


Figure 2.3: The CRESST setup with shielding [28]. The cryostat (CR) is at the top. The cold finger (CF) provides the thermal coupling of the detector holder (carousel, CA) to the cryostat. The orange rectangles which surround the detector holder represent the copper shielding (CU). The lead shielding (PB) is the gray layer around the copper. The radon box is denoted by RB. The muon veto (MV) is represented in dark blue. The polyethylene neutron shielding (PE), which is the most external shielding layer, is represented in yellow. As pointed out by the two circles in the picture, during Run 30 there were still small holes in the PE shielding.

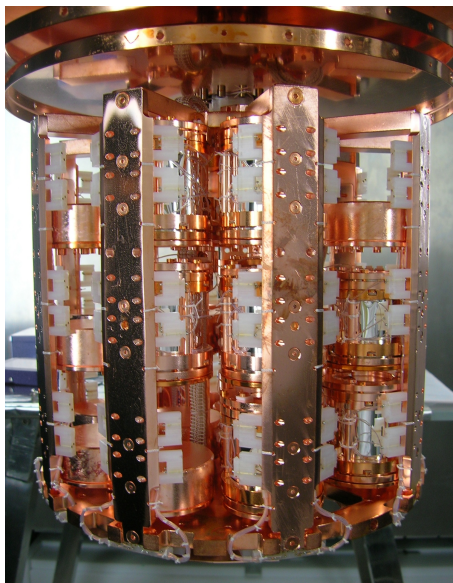


Figure 2.4: Detector holder (CA in Fig.2.3) presently mounted in the CRESST cryostat. The holder is made of ultrapure copper and can accommodate 33 detector modules, corresponding to a maximum target mass of ~ 10 kg CaWO_4 . The carousel-like holder allows the detector modules to be handled individually.

In Fig.2.3 a schematic drawing of the cryostat and the shielding is shown. Starting from the inner part, the first shielding consists of ~ 14 cm of low-background copper (orange rectangles in Fig.2.3, CU), followed by a ~ 20 cm thick low-background lead shielding (gray squares in Fig.2.3, PB). These two layers prevent γ radioactivity from the environment to reach the detectors.

This entire part (cold box plus copper and lead shielding) is enclosed in a gas tight box, the so-called radon box (RB). It is continuously flushed with pure nitrogen gas, evaporated from a can of liquid nitrogen. In this way the radon present in the atmosphere surrounding the detectors is flushed, as, being radioactive, it would produce additional background.

The most external layer provides a neutron shielding. It consists of ~ 45 cm of polyethylene (yellow in Fig.2.3, PE) that, being composed of light nuclei, has a high interaction cross section for neutrons. Neutrons with an energy of some MeV are moderated to thermal energies and then captured on the hydrogen. This is an efficient shielding for neutrons produced by fission of ^{238}U in the rocks surrounding the experimental setup. However, it is not as effective for higher energy neutrons produced, for example, by scattering of muons off nuclei in the rocks (see [52] and section 3.1).

Besides the passive shielding described above, a muon veto (MV) is present. This active shielding is located inside the PE shielding and consists of 20 plastic scintillator panels. The dimension of each panel is 1-1.2 m² and they cover $\sim 98.7\%$ of the solid angle. On the top it was unavoidable to have an opening of 0.27 m² for the cryostat's cold finger. A photomultiplier is coupled to each panel to readout the scintillation light produced by crossing muons. The signals of the photomultipliers are taken out of the Faraday cage via optical fibers, in order to avoid electronic interference with the detector signals.

2.4 Results of the CRESST-II Commissioning Run

The commissioning run of CRESST-II took place from March 27th to July 23rd 2007. During this run, 10 detector modules were installed in the cryostat. Two of them have worked very reliably as double detectors and were used for the dark matter analysis. The cumulative exposure was 47.9 kg-days. WIMPs are expected to interact mainly with tungsten. The corresponding tungsten exposure was 30.6 kg-days. A detailed treatment of the results of this run is provided in [28]. Here only a short summary is given.

In Fig.2.5, the events collected by the two detector modules are plotted (light yield versus phonon energy). The upper (black dashed) line represents the limit below which 90% of all nuclear recoils are expected. Below the lower (solid red) line, 90% of the tungsten recoils are expected. To calculate these limits the values of the quenching factors given in [53] of the different nuclei have been used.

The vertical dotted lines define the energy interval taken into account to search for WIMP events. The lower limit is set at 10 keV. This is the minimum energy for which a separation between electron and nuclear recoils is possible. Below this limit the two bands start to overlap and an event-by-event separation is not possible anymore.

For the upper energy limit, cross section arguments are taken into account. In Fig.2.6 the expected rates for WIMP scattering off oxygen, calcium and tungsten, and off CaWO_4 are shown. The Helm form factor [54] suppresses the cross section on tungsten for higher momentum transfer. In the case shown, a WIMP mass of 60 GeV and a WIMP-nucleon cross section of 10^{-8} pb were assumed, leading to a suppression of the cross section for tungsten at 55 keV [47].

As one can see in Fig.2.5, three events are present in the acceptance region, two in Zora (at 18.03 keV and 33.09 keV) and one in Verena(at 16.89 keV), which give a rate of 0.063 per kg-day on tungsten. An exclusion limit for

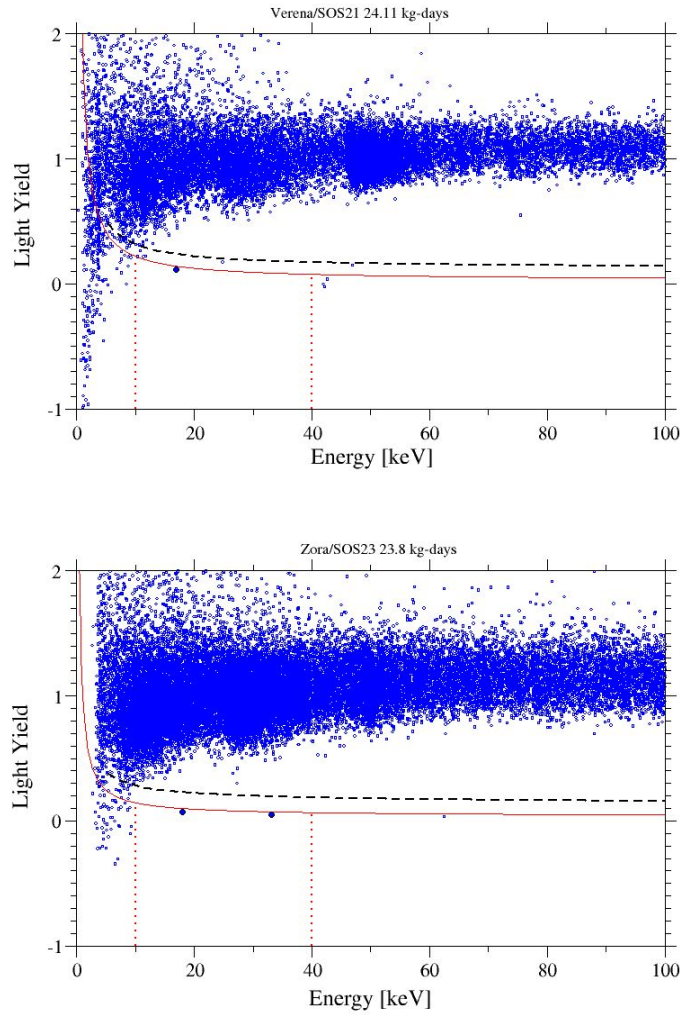


Figure 2.5: Events collected by the detectors Verena (top) and Zora (bottom) during the commissioning run. The black dashed line represents the limit below which 90% of all nuclear recoils are expected. The red solid line represents the limit below which 90% of the tungsten recoils are expected. An energy interval between 10 and 40 keV (vertical dotted lines) was taken into account. Three events (one in Verena and two in Zora, heavy dots) are present in the acceptance region.

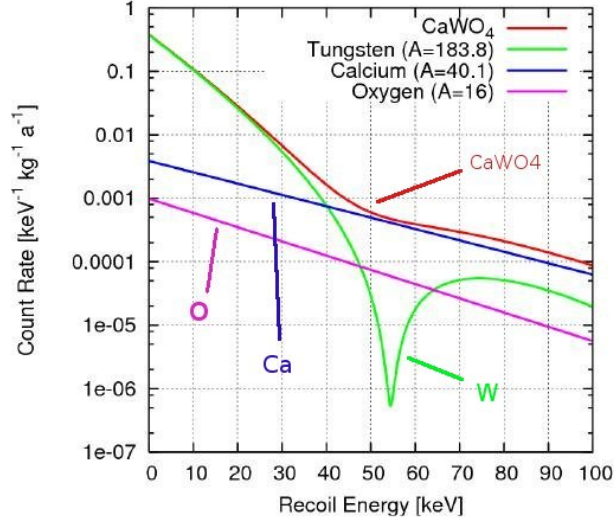


Figure 2.6: Expected WIMP recoil rates for oxygen, calcium, tungsten, and in total for CaWO_4 for a WIMP mass of 60 GeV and a WIMP-nucleon cross section of 10^{-8} pb. The strong suppression of the cross section for tungsten around 55 keV is due to the Helm form factor [47], [54].

the coherent spin-independent WIMP-nucleus cross section can then be calculated, using standard assumptions on the dark matter halo [28]. The result is plotted in Fig.2.7 (red solid line).

As to the origin of the three events, different scenarios are taken into account. One possibility is that they are caused by neutrons that passed through the polyethylene shielding. The probability that a neutron after passing 45 cm polyethylene still has enough energy to produce an event like the one observed is extremely low, but during the run30 holes were present in the shielding (see Fig.2.3), through which neutrons could penetrate in the setup. These holes have been patched only after the run was stopped. Neutrons, in any case, should produce oxygen recoils, while the observed events are compatible with the QF of tungsten.

Another possible origin of these events could be given by the non complete coverage of the inner surface of the detector module with the reflecting-scintillating foil. As described in section 2.1, the scintillating foil is needed for the discrimination of surface α decay events. The coverage of the foil,

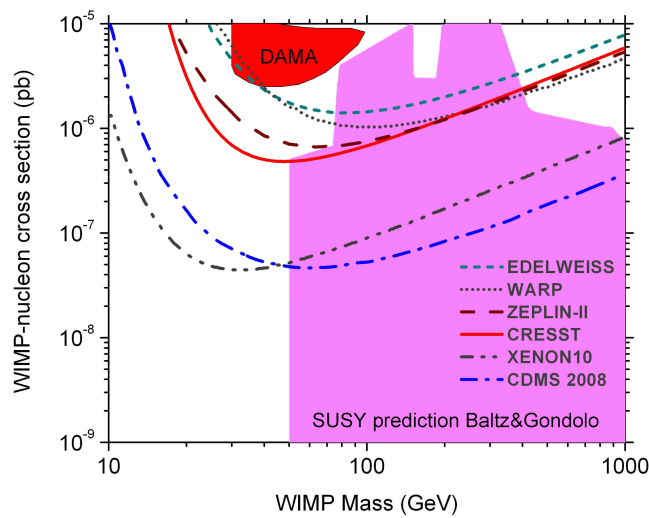


Figure 2.7: Results of the CRESST-II commissioning run in the exclusion plot for coherent spin-independent cross section. (March-July 2007) [28]. For comparison limits from other experiments are also shown: CDMS [27], XENON [29], WARP [30], EDELWEISS [15], as well as the range predicted by some supersymmetric models [34]. The DAMA collaboration claims a positive evidence [32] [33].

however, is not complete, and if the α hits a part of the holder that is not scintillating, for example the non-scintillating clamps holding the detector, an event is produced, completely similar to a tungsten recoil. This could be the case of the three events discussed here.

A detailed discussion of the results of this run is given in [28].

After the commissioning run, some changes were made in the setup. More detector modules have been mounted (17) in order to increase the target mass. In order to further reduce the possibility of α particles escaping, the springs holding the detectors have been covered with scintillating material as e.g. Araldite. Some of the (phonon) detectors mounted are composite detectors, in which the phonon detector is glued on the absorber crystal ([55] [56] [57] [58]). As new target material ZnWO_4 is also being tested. The new run took place from April to December 2008. Data evaluation is still in progress.

Chapter 3

Nuclear Quenching Factors

As described in the previous chapter, the CRESST detectors are able to discriminate most of the radioactive background thanks to the different light output between electron-recoil events and events due to nuclear recoil or α s. The parameter that we use to characterize the light output is the quenching factor (QF). The definition of this parameter is given in section 2.1. The QF is, in first approximation, independent of the energy of the interaction. The QF for electron recoils is defined as 1. Since WIMPs are expected to produce nuclear recoil events, all electron recoil events are background and can be discriminated by means of the QF.

Background events that produce nuclear recoils in the detector cannot be discriminated in this way, therefore they represent a dangerous background for the detection of WIMPs. Such kind of events are produced mainly by neutrons from the environment. The origin of neutrons in the surrounding of the experiment is illustrated in the next section.

3.1 Neutron Background

Several mechanisms are responsible for the production of neutrons in the surroundings of the CRESST experiment and the energy of these neutrons depends on the respective production mechanism. One of the possible origins

of neutrons is from fission of ^{238}U in the surroundings of the experiment. ^{238}U is present in the surrounding rock, but can also be present in the material used in the experimental setup. In particular lead, used as shielding against radioactivity from the environment, can contain some ^{238}U contamination. The neutrons produced in fission decays have an energy below 10 MeV, so they can easily be moderated by a polyethylene shield. The CRESST experiment is completely surrounded by a 45 cm thick polyethylene shield. Neutrons produced outside this shielding are either absorbed or reach the detectors with an energy well below the threshold of the region of interest (ROI).

Even more dangerous are fission events that occur inside the polyethylene shielding. In this case, the energy of the neutrons reaching the detectors is still high enough to produce nuclear recoil events in the energy range where WIMP events are expected. In the CRESST experiment the lead shielding is situated inside the polyethylene shielding, so that neutrons produced in fission processes from ^{238}U nuclei in the lead can reach the detectors with their full energy.

Another process responsible for neutron production is scattering of muons off nuclei in the material surrounding the detectors. High energetic muons can excite nuclei which can then emit neutrons in the de-excitation process. Neutrons produced by this mechanism can have an energy up to 100 MeV, so that the 45 cm of polyethylene shielding are not sufficient to moderate them before they reach the detectors. Also in this case it is crucial where the event takes place: as described in section 2.2 the CRESST setup is equipped with a muon veto. If the neutron is produced inside the veto, recoil events caused by such neutrons can be eliminated using the coincidence with the event in one or more of the veto panels. On the other hand, if the muon interaction occurs outside of the veto, the nuclear recoil cannot be eliminated because there is no signal from the veto.

Both cases, i.e. fission of ^{238}U inside the polyethylene shield, or production of a neutron by a high-energetic muon outside the muon veto, can lead to “WIMP like” events.

In order to improve the sensitivity of the experiment, one has to find ways to discriminate also such kinds of events. In the CRESST experiment the target material (CaWO_4) contains three different nuclei (oxygen, calcium and tungsten). If one looks at the ROI (10-40 keV) (the interval where WIMP events are expected, see section 2.4) the occurrence of oxygen, calcium or tungsten recoils can be expected to be very different. First of all, the target contains four times more oxygen than calcium or tungsten, so that oxygen recoils are enhanced by a factor of four. Second, for kinematic reasons, in most cases tungsten recoils will have a very low energy because of the big mass difference between the tungsten nuclei and neutrons.

One can try to estimate the different contributions to the recoil spectrum produced by neutrons from the background with the help of a calculation based on cross section data for neutrons on oxygen, calcium and tungsten. Details on the calculation are given in section 4.1.2. To perform the calculation one needs to know the energy spectrum of the incoming neutrons. In [52] the neutron background for the CRESST experiment is discussed. In the presence of a polyethylene shielding the main contribution is found to originate from neutrons produced in the fission of ^{238}U in the lead shielding. The spectrum of such neutrons is depicted in Fig.3.1. In Fig.3.2 the calculated recoil spectra for oxygen, calcium and tungsten are plotted, obtained performing the calculation described in section 4.1.2 with the spectrum of Fig.3.1 for the incoming neutrons.

As one can see from Fig.3.2, in the energy region from 10 to 40 keV, the recoil spectrum is dominated by oxygen recoils. On the other hand, WIMP events are expected to be mainly tungsten recoils. This is due to the interaction cross section of WIMPs with nuclei, which is expected to be proportional to A^2 (where A is the atomic mass number of the interacting nucleus) for spin independent scattering processes (see section 1.3.2). Thus oxygen recoil events can be attributed mainly to background neutrons, while tungsten recoils are mainly attributed to WIMPs. In order to discriminate the neutron background we need to identify the recoiling nucleus. For this

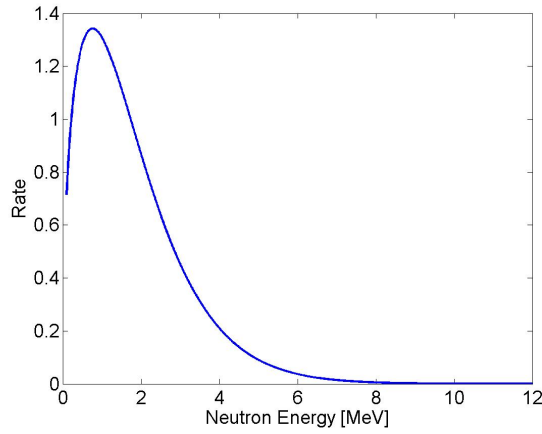


Figure 3.1: Energy spectrum of neutrons produced by fission of ^{238}U [52].

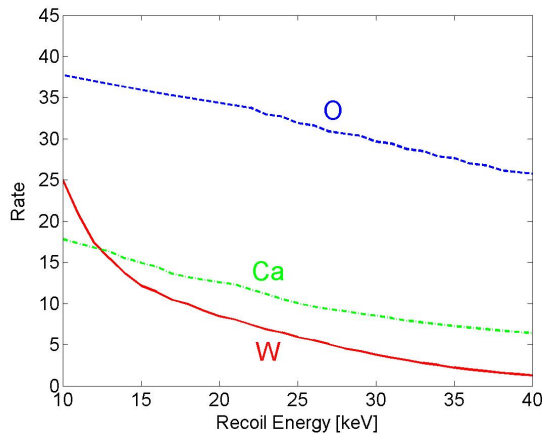


Figure 3.2: Example of calculated recoil energy spectra for oxygen (dashed blue line), calcium (dashed-dotted green line) and tungsten (solid red line) in CaWO_4 (the oxygen spectrum is multiplied by 4 to take the chemical composition into account). The calculation is performed for the neutron energy spectrum of neutrons produced by fission of ^{238}U (see Fig.3.1). The energy interval (10-40 keV) shown is the one considered in CRESST to search for WIMPs events (see section 2.4).

purpose a similar method can be used to that for distinguishing between electron and nuclear recoils. Different nuclei have, in fact, different light outputs, or different QF. If this difference can be resolved, it can be used to identify the recoiling nucleus.

Various methods can be used to measure the quenching factors of the nuclei. In the following sections advantages and disadvantages of these methods are compared.

3.2 Principle of Measurements of the Quenching Factors

To produce nuclear recoils, neutrons can be used. Equation 3.1 describes, for the non-relativistic case, the recoil energy in the laboratory system (E_{rec}) given to a nucleus of mass M_x in a scattering event with an incoming neutron (mass M_n , energy E_{in} in the laboratory system) (Fig.3.3). The neutron is scattered at an angle θ_{cm} in the center of mass system.

$$E_{rec} = 2E_{in} \frac{M_n \cdot M_x}{(M_n + M_x)^2} (1 - \cos\theta_{cm}) \quad (3.1)$$

The relation between the scattering angle in the center of mass system (θ_{cm}) and in the laboratory system (θ_{lab}) is given by equation 3.2

$$\cos\theta_{cm} = -\frac{M_n}{M_x} \sin^2\theta_{lab} \pm \sqrt{1 - \frac{M_n}{M_x} \sin^2\theta_{lab}} \quad (3.2)$$

For $\theta_{cm} = 0^\circ$, $E_{rec} = 0$, for $\theta_{cm} = 180^\circ$ (backward scattering) $E_{rec} = E_{max}$, with

$$E_{max} = 4E_{in} \frac{M_n \cdot M_x}{(M_n + M_x)^2} \quad (3.3)$$

In general, the recoil energy can have any value between 0 and E_{max} . This means that also in the simple case of monoenergetic neutrons, one gets a continuous recoil spectrum, the shape of which depends on the characteristics

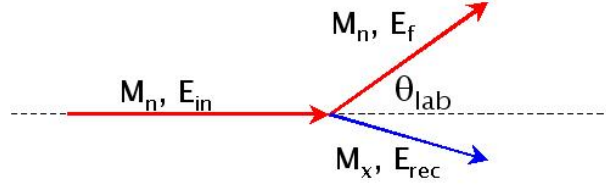


Figure 3.3: Scattering of a neutron (mass M_n , energy E_{in}) from a nucleus (mass M_x), in the laboratory system. E_{rec} and E_f are the energy after the scattering for the nucleus and the neutron respectively.

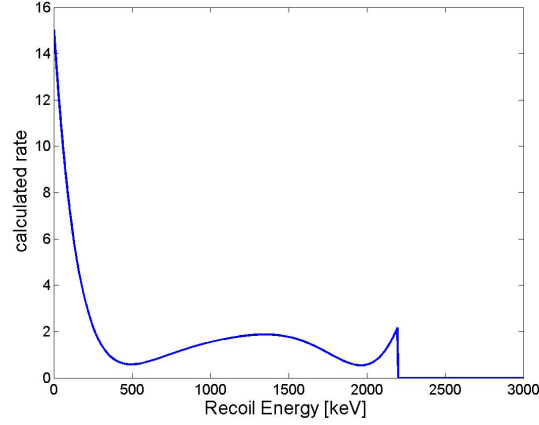


Figure 3.4: Calculated energy spectrum of recoils of oxygen atoms produced by monoenergetic neutrons of energy 10 MeV. The scattering angle is not fixed. E_{max} in this case is 2.2 MeV (Eq. 3.3). Above this energy the amplitude of the spectrum goes to zero.

of the differential cross section $d\sigma/d\theta$ for scattering of neutrons from the recoiling nucleus. Fig.3.4 shows, as an example, the calculated recoil spectrum of oxygen for elastic scattering of monoenergetic neutrons of energy 10 MeV. This recoil spectrum has been calculated using equation 3.1 and neutron cross section data from [59]. For non-monoenergetic neutrons the recoil spectrum is more complicated. More details concerning the expected recoil spectra are given in section 4.1.2.

In CaWO_4 there are three different kinds of nuclei: when the crystal is irradiated by neutrons with a certain energy spectrum, the energy spectrum

of the recoils produced will be different for each of the three kinds of nuclei, depending on the mass of the nuclei and the cross sections for the interaction of neutrons with these nuclei.

The presence of three superimposed continuous spectra makes it difficult to separate the three different populations of nuclear recoil events. However, it is exactly such a separation that we need in order to determine the quenching factors of the different nuclei.

Despite the difficulty of separating the spectra, neutrons remain a good tool for the measurement of nuclear quenching factors because they can penetrate inside the detector. Thus they have the big advantage that the recoils produced are uniformly distributed in the bulk of the detector, i.e. the CaWO_4 crystal. They are a very similar kind of events to those that we expect from background neutrons in the case of oxygen recoils. The kind of events produced by WIMPs are mainly due to elastic scattering from tungsten nuclei: for the same energy transferred, the response of the detector is the same when a tungsten recoil is produced by a WIMP or by a neutron.

3.2.1 Neutron Scattering with Fixed Kinematics

As seen in the previous section, the recoil spectrum obtained by irradiating CaWO_4 with neutrons is very complicated to interpret, even in the case of a monoenergetic neutron source. In order to improve the situation, in addition to using monoenergetic neutrons, one needs to fix the scattering angle. In this case, as apparent from equation 3.1, for elastic scattering there is only one possible recoil energy for each nucleus. The expected spectrum is then of the kind schematically shown in Fig.3.5 : three separate populations of events appear, one for each kind of nucleus. In this way the quenching factor of each nucleus can be measured.

This kind of measurement has already been performed at our institute at room temperature [60] [61]. A monoenergetic 11 MeV neutron beam has been produced at the Maier-Leibnitz-Laboratorium (MLL) in Garching. Details on the neutron beam (production, energy spectrum, etc.) are given in

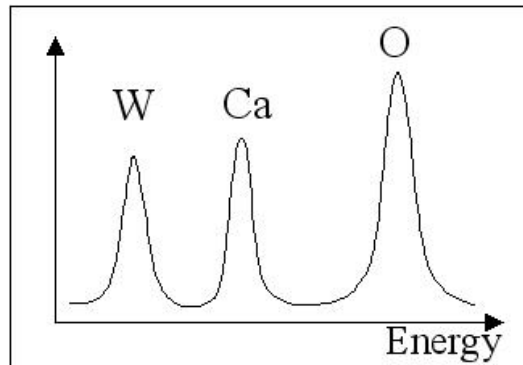


Figure 3.5: Schematic of the expected ideal recoil spectrum obtained by irradiating CaWO_4 with monoenergetic neutrons at a fixed scattering angle.

section 4.1.3. Forty neutron detectors of the kind described in section 4.1.3 were placed at a certain angle θ the choice of which depends on the recoil energy to be measured and on the cross section. By performing a coincident measurement between events in the CaWO_4 crystal and events in one of the neutron detectors, one eliminates all events in which the neutron is scattered at an angle different from θ . The spectrum of the events selected this way is then of the kind shown in Fig.3.5. Since the scintillating properties of the CaWO_4 crystal can vary with its temperature [62], it is necessary to repeat the measurement at the operating temperature of the CRESST detectors, i.e. ~ 10 mK.

3.2.2 Ion Irradiation

Another measurement for the investigation of the response of the detector crystal to nuclear recoils, based on a completely different concept, has been performed at the Max-Planck-Institut für Physik in Munich [63]. In this case, the impinging ions are produced and accelerated outside of the crystal. In Fig.3.6 a schematic of the setup is shown. The ions are produced in the LDI (Laser Desorption/Ionisation) chamber by a pulsed laser. The production rate is such that not more than one ion for every pulse of the laser reaches the detector. The ions are then accelerated by a high voltage, up to a maximum

3.2. PRINCIPLE OF MEASUREMENTS OF THE QUENCHING FACTORS⁴⁵

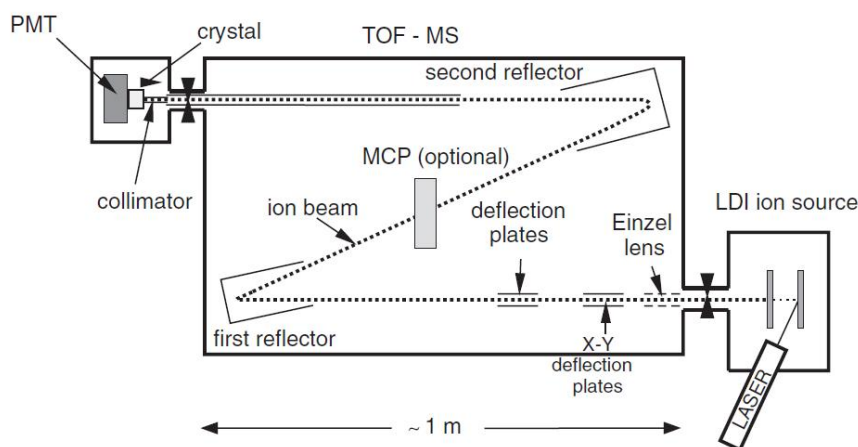


Figure 3.6: Schematic of the setup for the measurement of the quenching factors by ion irradiation. On the right bottom part, the LDI (Laser Desorption/Ionisation) chamber is represented, where the ions are produced. In the middle is the time-of-flight mass spectrometer (TOF-MS). Here the ions are selected on the base of their time of flight, so that only the desired ions reach the crystal. On the top left square in the picture, the location of the crystal and the photomultiplier is represented.

energy of 18 keV. In the TOF-MS (time-of-flight mass spectrometer) chamber the ions with the desired energy are selected and finally reach the crystal, which is coupled to a photomultiplier tube, that detects the scintillation light produced by the incoming ion.

This method has the advantage that one controls completely the events that are produced: one can select the energy of the events and investigate each event separately. One can also investigate the Quenching Factor of a CaWO_4 crystal for more elements than in the case of neutron induced nuclear recoils. Results obtained with this method are shown in Fig.3.7. Several elements have been investigated. A clear dependence on the mass appears: the QF is increasing with increasing mass of the impinging ion. For the heaviest ions the tendency of a saturation of the QF value is observed.

Since the ions are irradiated from outside, the produced events are surface events. If there is a difference in the pulses produced by surface events with respect to bulk events, the value of the QF measured with the method

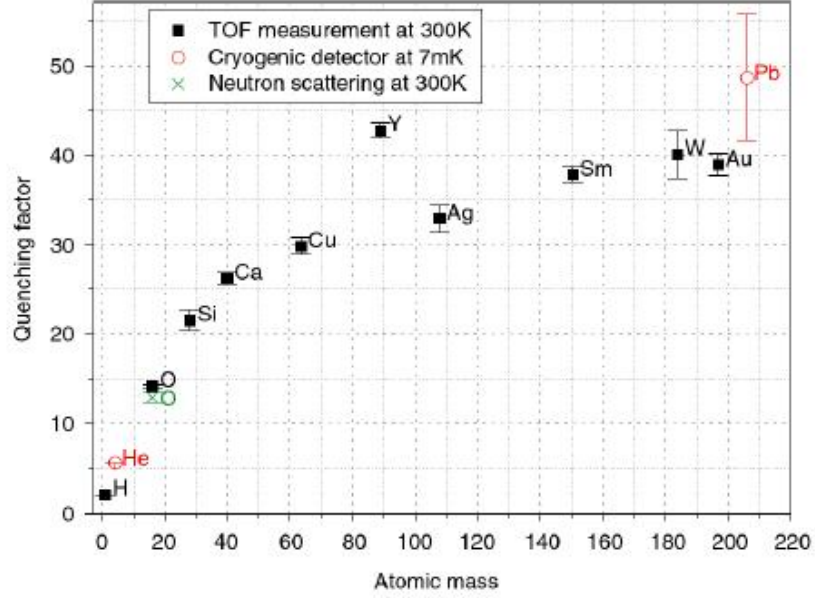


Figure 3.7: Results for the QFs of CaWO_4 for the different selected ions, measured by ion irradiation [63]. For comparison, also results obtained with different methods are shown. The red open circles represent values of the QFs at 7 mK obtained from the CRESST measurement data. The green cross represents the value of the QF of oxygen, obtained with the scattering experiment at room temperature, described in section 3.2.1. An increase of the value of the QF with the mass of the recoiling nucleus is observed.

described here will be deeply influenced.

Ion irradiation measurements have been performed at different temperatures, the lowest being 4.2 K. At present, it is not possible to perform this sort of measurement at the temperature at which the detectors are operated (10-20 mK in the CRESST experiment). The reason for this is that one needs a window through which the detector can be irradiated. However, such a window would not allow to reach operational temperatures in the mK range, due to infrared radiation.

The results of the measurements described in this section and in section 3.2.1 will be discussed again in section 5.3.4 and compared with the results of the bulk measurements at mK temperatures, described in this thesis.

Chapter 4

Setup of the Scattering Experiment

The main aim of the work presented in this thesis, is the determination of the bulk quenching factors (QFs) at mK temperatures of the three different nuclei (oxygen, calcium and tungsten) present in CaWO_4 . As explained in the previous chapter, this is necessary in order to be able to distinguish events produced by background neutrons from WIMP events. Nuclear recoils have been induced by irradiation of the detector crystal with neutrons. In this chapter an overview of the neutron sources used for the measurements and a description of the experimental setup are given.

4.1 Neutron Sources

4.1.1 Standard Neutron Sources

Available standard neutron sources are ^{252}Cf and $^{241}\text{Am-Be}$.

^{252}Cf is an unstable isotope with a half-life of $T_{1/2} = 2.645$ y. It decays via α emission (96.9%) and spontaneous fission (3.1%). In the case of fission decays, neutrons are emitted with an average energy of 2.3 MeV. In Fig.4.1 (left) the energy spectrum of the neutrons produced by a ^{252}Cf source is shown [64].

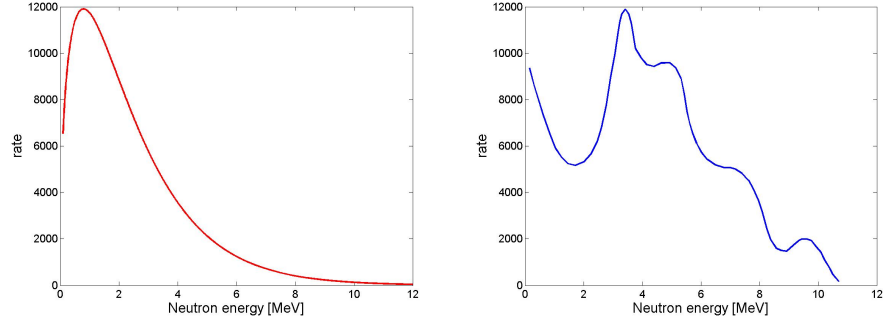


Figure 4.1: Energy spectra of neutrons from a ^{252}Cf source [64] (left) and from a $^{241}\text{Am-Be}$ source (right) [60].

Another possibility to obtain neutrons in the MeV energy range is by an $^{241}\text{Am-Be}$ source. In this case a chain of reactions takes place, which ends up with the emission of neutrons. The first step is the α decay of ^{241}Am ($^{241}_{95}\text{Am} \rightarrow ^{237}_{93}\text{Np}^{(*)} + \alpha$). The $\text{Np}^{(*)}$ is in its $2nd$ excited state in 85% of the cases. From this excited state it decays primarily to the ground state by the emission of a 60 keV γ . The emitted α particle is captured by Be: $^9_4\text{Be} + \alpha \rightarrow ^{13}_6\text{C}^*$ and the highly excited $^{13}_6\text{C}^*$ decays by emission of a neutron ($^{13}_6\text{C}^* \rightarrow ^{12}_6\text{C}^* + n$) [65]. The resulting neutron spectrum is shown in Fig.4.1 (right). The average energy is ~ 5 MeV.

The advantage of these sources is that they are easy to handle and can be used at any time. On the other hand, the neutrons produced are not monoenergetic and the energy is relatively low. Furthermore, there is no possibility to set a trigger on the production of neutrons, so that a time-of-flight measurement is not possible.

4.1.2 Expected Recoil Spectra

As seen in section 3.2, recoils produced by neutrons exhibit a continuous spectrum even in the simple case of monoenergetic neutrons, if the scattering angle is not fixed (Fig.3.4). The shape of the spectrum, for a given neutron energy E_1 , depends on the mass of the recoiling nucleus and on the characteristics of the interaction cross section of neutrons with such a nucleus. Since

the recoil energy is related to the scattering angle θ_{cm} in the center-of-mass system (equations 3.1 and 3.2), the recoil spectrum is influenced by the characteristics of the differential cross section $d\sigma/d\theta_{cm}$. For example, if $d\sigma/d\theta_{cm}$ has a local maximum for a certain value of $\theta_{cm} = \theta_1$, the recoil spectrum for monoenergetic neutrons of energy E_1 will have a local maximum at the recoil energy (E_{rec1}) corresponding to the scattering angle θ_1 :

$$E_{rec1} = 2E_1 \frac{M_n \cdot M_x}{(M_n + M_x)^2} (1 - \cos\theta_1) \quad (4.1)$$

In a case like ours, where the target is a material containing three different kinds of nuclei, it is highly desirable to know the expected shape of the recoil spectrum of each kind of nucleus. For this purpose calculations have been performed in the following way. As input, the energy spectrum of the source is taken. For each value of the incoming neutron energy E_i (from zero to the maximum energy of the spectrum of the source, in steps of 10 keV) a recoil spectrum is calculated. In this way, for example, the spectrum of Fig.3.4 has been obtained. This spectrum is then multiplied by the intensity of the spectrum of the source at the energy E_i and by the amplitude of the scattering cross section for neutrons of energy E_i on the nucleus considered. The spectra obtained in this way (each one corresponding to a particular value of E_i) are then summed to obtain the final spectrum. The values for the cross section needed to perform the calculation are taken from [59]. The calculation has been performed with a program developed by M. Stark [66] for oxygen, calcium and tungsten. The spectrum for oxygen is multiplied by four, according to the stoichiometric conditions. The results obtained in this way are shown in Fig.4.2, where the calculated spectra for oxygen, calcium and tungsten are depicted, using as input spectrum for the calculation, the spectrum of a ^{252}Cf source (dotted lines) and of an $^{241}\text{Am-Be}$ source (solid lines).

The calculation just described is relatively simple, because it only takes into account the interaction of the neutrons with the nuclei without considering the influence of the environment. Of course, the appropriate method

would be to perform a Monte Carlo simulation, on the other hand the calculation has the advantage that it can be performed relatively quickly and adapted to different spectra of the neutron source and different target nuclei. As we will see, this calculation well reproduces the measured spectrum, being so a very helpful tool for the understanding of the results.

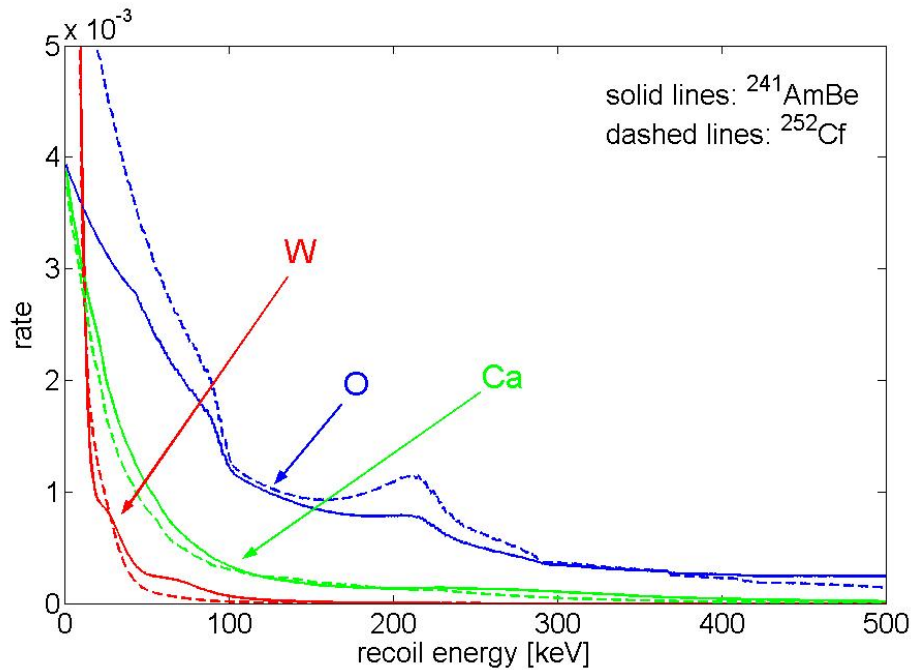


Figure 4.2: Calculated energy spectra of oxygen, calcium and tungsten recoils produced by irradiation of a CaWO_4 crystal with a $^{241}\text{AmBe}$ source (solid lines) and a ^{252}Cf source (dotted lines).

The shapes of the spectra shown in Fig.4.2 are due to characteristics of the interaction cross section. The most evident feature is the peak at ~ 220 keV in the recoil spectra of oxygen obtained with both sources, more pronounced in the case of the Cf source. This can be explained by taking the interaction cross section of neutrons with oxygen into account. In Fig.4.3, the interaction cross section for neutrons on oxygen is plotted versus the neutron energy. Resonances are clearly visible at several energies. Especially pronounced are the resonances for neutrons of 0.44 MeV and 1 MeV. In the energy spectra of both sources, neutrons of these energies are present and,

given the enhancement of the cross section, the corresponding recoil spectra give a higher contribution. The oxygen recoil spectra for neutron energies of 0.44 MeV and 1 MeV are shown in Fig 4.4.

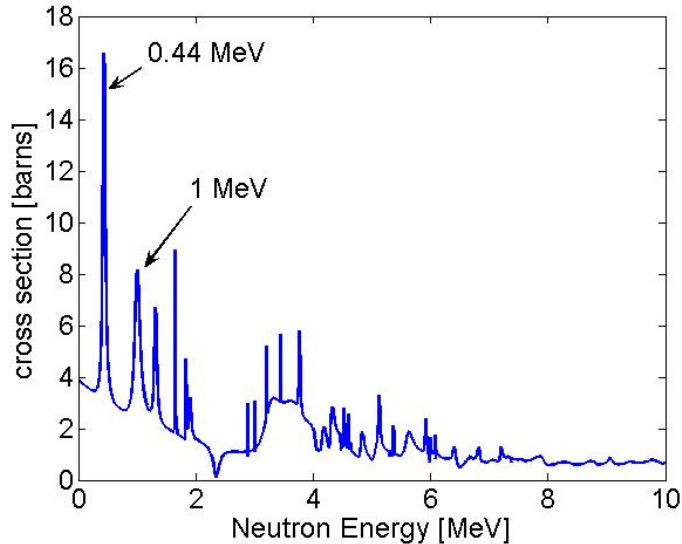


Figure 4.3: Cross section of neutrons on oxygen as a function of the energy of the neutrons. The two intense resonances, visible at 0.44 MeV and at 1 MeV, produce structures in the recoil spectrum of oxygen, at ~ 90 keV and at ~ 220 keV, respectively.

The recoil spectrum for neutrons of 1 MeV has a peak corresponding to a maximum recoil energy of ~ 220 keV (see right spectrum of Fig.4.4). When this spectrum is multiplied by the value of the cross section corresponding to this particular incoming energy, this characteristic is enhanced and results in a clearly visible peak in the total spectrum (see Fig.4.2). For the resonance at 0.44 MeV the maximum at ~ 90 keV is less pronounced (see left spectrum Fig.4.4). This together with the fact that in the low recoil-energy region (below ~ 90 keV) the rate is rapidly increasing, has the consequence that in the oxygen recoil spectrum obtained with a continuous spectrum for the incoming neutrons, the feature at ~ 90 keV is not as clearly visible as the one at ~ 220 keV. The local maximum at ~ 220 keV (Fig.4.2) is more pronounced for the Cf case than for Am-Be, because 1 MeV neutrons give a bigger relative

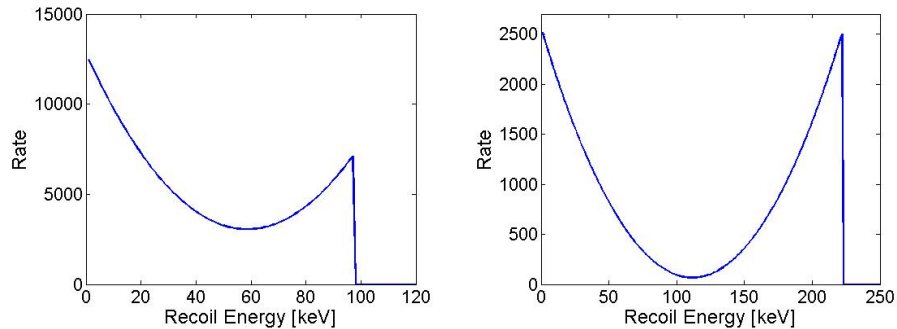


Figure 4.4: Calculated recoil spectra for monoenergetic neutrons of energy 0.44 MeV (left) and 1 MeV (right). The sharp drop of the spectra corresponds to the maximum energy transfer for a neutron of the given energy on oxygen (equation 3.3).

contribution to the spectrum of the Cf source than to that of the Am-Be source (the spectrum of the Cf source has its maximum just below 1 MeV, see Fig.4.1).

The interesting aspect is that the position of the local maximum only depends on the characteristics of the interaction of neutrons with oxygen. The shape of the spectrum of the incoming neutrons determines only how pronounced this peak is. Since oxygen recoils dominate in comparison to those of calcium and tungsten, this peak is visible also in the total recoil spectrum. As will be shown in section 5.4, this feature can be recognized in the measured nuclear recoil spectrum. Thus, it can be used as a reference point for the calibration of the nuclear recoil band (see section 5.4).

4.1.3 11 MeV Neutron Beam

In addition to the standard neutron sources mentioned in the previous sections, we have also irradiated the detector with a monoenergetic neutron beam [60] [67].

The beam has been produced at the Tandem van de Graaf accelerator at the Maier-Leibnitz-Laboratorium (MLL) in Garching. For the generation of the neutrons the reaction $p(^{11}\text{B},n)^{11}\text{C}$ has been used. The target at the end

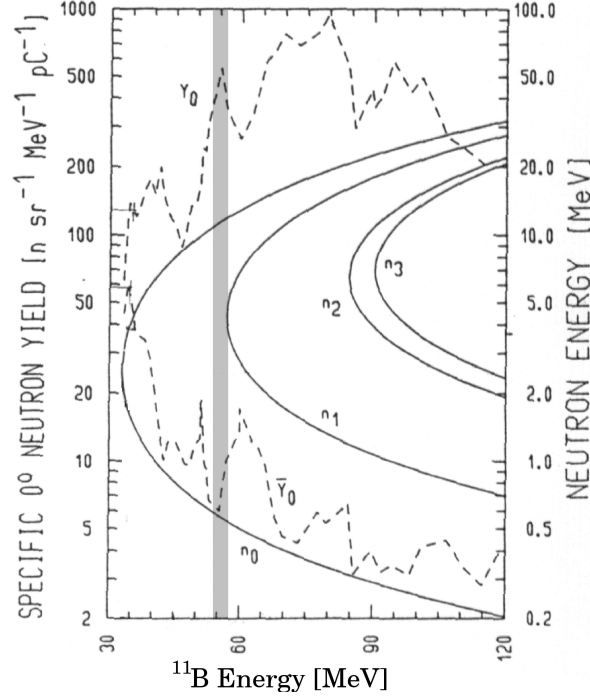


Figure 4.5: Energy dependence of the neutron energies (solid lines) of the ${}^1\text{H}({}^{11}\text{B},\text{n}){}^{11}\text{C}$ reaction (populating the four lowest energy levels in ${}^{11}\text{C}$ indicated by the labels n_0 , n_1 , n_2 , n_3) on the ${}^{11}\text{B}$ energy. The dashed line gives the yield at 0° for the high energy branch (Y°) and the low energy branch (\bar{Y}°) of the n_0 neutron group [68]. The area marked in gray represents the beam energy chosen for the production of neutrons. This region is particularly convenient, because the high energy branch at zero degrees (Y°) has a maximum, while the low energy branch (\bar{Y}°) has a minimum.

of the beam line consists of H_2 gas. The gas is contained in a cylindrical cell (length 3 cm and diameter 1 cm) at a pressure of ~ 3 bar. A $5\ \mu\text{m}$ thick molybdenum window separates the cell from the beam line itself.

In the center-of-mass system, monoenergetic neutrons are produced. The energy and angular distribution of the neutrons produced depend on the energy of the ${}^{11}\text{B}$ projectile.

In Fig.4.5 the characteristics of the reaction $\text{p}({}^{11}\text{B},\text{n}){}^{11}\text{C}$ as a function of the energy of ${}^{11}\text{B}$ are depicted [68]. The neutron energy in the laboratory system at 0° is plotted as a function of the projectile energy (full lines). The

different curves (n_0 , n_1 , n_2 and n_3) refer to reactions where the four lowest energy levels in ^{11}C are populated. For each energy of the projectile, neutrons of two different energies are produced. This is due to the kinematics of the reaction. The projectile is, in this case, much heavier than the target (inverse reaction). For this reason the center-of-mass has a relatively high velocity in the laboratory system. This has the consequence that also neutrons emitted backwards in the center-of-mass (CM) system, are emitted forwards in the laboratory system, but with a lower energy. The two branches of the reaction correspond, then, to neutrons emitted at 0° in the CM system (high-energy branch) and to neutrons emitted at 180° in the CM system (low-energy branch). The dashed line gives the yield of the two groups of neutrons for the n_0 case.

The projectile energy chosen is the one marked in gray in Fig.4.5. In this case the neutrons of the high-energy branch in the laboratory system have an energy of 11 MeV (intersection of the gray area with the upper part of the n_0 curve), while the low-energy neutrons (intersection of the gray area with the lower part of the n_0 curve) have an energy of ~ 0.5 MeV. This choice is convenient because the high-energy branch of the reaction has a local maximum and at the same time the low-energy branch has a local minimum (dashed line). Moreover, the energy of the projectile is not yet large enough to produce neutrons of the group n_1 [60]. The inverse kinematic has also the consequence that the emitted neutrons do not have a 4π distribution in the laboratory system, but they are collimated in the forward direction. For the chosen projectile energy, the maximum angle at which neutrons are produced is $\sim 45^\circ$. In section 5.1, measurements of the beam profile at different angles are shown and discussed.

In Fig.4.6, the energy spectrum of the neutrons of the beam at 0° is shown. This spectrum has been recorded by measuring the time-of-flight of the neutrons from the target cell, where they are produced, to a detector situated at 0° . The detector for the measurement of the spectrum uses a liquid organic scintillator (NE 213) as target material contained in a hexagonal cell

of 91 mm inner diameter and 50 mm height. The scintillation light is observed by a photomultiplier. The NE 213 liquid scintillator is composed of light elements, in particular $\sim 50\%$ of hydrogen, that makes it a good target for neutrons: the energy transfer for scattering of neutrons from protons is higher than for any heavier nucleus, since proton and neutron have almost the same mass ($M_p \cong M_n$). The maximum energy transfer corresponds, in this case, to the total energy of the neutron. Furthermore, NE 213 is optimized for pulse shape discrimination between neutron signals and γ signals [69]. This discrimination is important because the γ s produced simultaneously with the neutrons constitute a background for the neutron measurement and need to be discriminated. The energy threshold of these detectors is ~ 2 MeV for neutrons.

This kind of detector can tell that a neutron interaction has happened, but it cannot give information on the energy of the neutron. The interaction can be described by equation 3.1, with $M_x = M_p \cong M_n$. This means that, depending on the scattering angle, the energy released by the neutron in the detector, in the form of recoil energy of a proton, can have any value between zero and $E_{max} = E_{in}$. For this reason, to measure the energy of the neutrons a time-of-flight measurement is needed.

In such a measurement, the energy resolution is related to the resolution on the time-of-flight by the following relation

$$\frac{\Delta E}{E} = 2 \frac{\Delta t}{t} \quad (4.2)$$

so increasing the time-of-flight, the error on the energy decreases.

For the error on the time-of-flight, several contributions have to be taken into account. Firstly, one needs to know the time when the neutron was produced. In our case this was achieved by pulsing the ^{11}B beam. The intensity of the beam is chosen such that for every bunch of ^{11}B ions reaching the cell, not more than one neutron interacts in the neutron detector. As start signal for the time-of-flight measurement the signal of the pulsing system of the accelerator beam was used. The time spread of the bunches, then,

contributes to the time resolution of the measurement. This time spread is ~ 2 ns. The position in the target cell where the reaction takes place contributes to the time spread with ~ 1.5 ns and a similar contribution is given by the uncertainty of the position in the neutron detector where the detection takes place. Finally the resolution on the time measurement, which is given by the resolution of the TDC, has to be taken into account. In our case the TDC has a resolution of ~ 3 ns.

The last contribution is the largest, and, in fact, the overall time resolution of the measurement described here was ~ 3 ns. For the measurement of the beam spectrum, the distance between the target cell and the neutron detector was 163 cm: the time of flight of the 11 MeV neutrons was then 36 ns. This leads, from equation 4.2, to an energy resolution of 20%.

The measured spectrum, shown in Fig.4.6, has a peak at 10.7 ± 0.1 MeV that corresponds to the neutrons emitted at 0° in the CM system. The low energy neutrons that appear in the spectrum have several origins. Part of them are the neutrons emitted at 180° in the CM system, that, given the velocity of the center-of-mass, have also a forward velocity in the laboratory system, but a much lower energy. Low energy neutrons are also produced by interactions of the ^{11}B ions in the molybdenum window that separates the hydrogen cell from the beam line, and in the gold beam stop at the end of the cell.

The calculation of the recoil spectra described in section 4.1.2 was performed using the measured neutron spectrum shown in Fig.4.6. Of course, it is necessary to make an assumption on the shape of the spectrum below 2 MeV, which is the energy threshold of the detector used for the measurement of the spectrum of Fig.4.6. The shape that has been found to best reproduce the measured spectrum is the sum of an exponential curve (for the low-energy part) and a Gaussian centered at 10.7 MeV for the peak. In Fig.4.7 the curve used as input spectrum for the calculation is shown. The results of the calculation of the recoil spectra for oxygen, calcium and tungsten are shown in Fig.4.8.

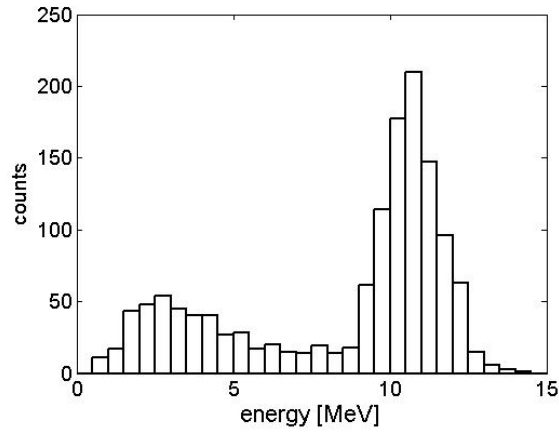


Figure 4.6: Energy spectrum of the neutron beam from the accelerator, at 0° . The spectrum has been recorded by measuring the time-of-flight of the neutrons from the target cell to a neutron detector situated at a distance 1.63 m in the direction of the beam line (see section 5.1).

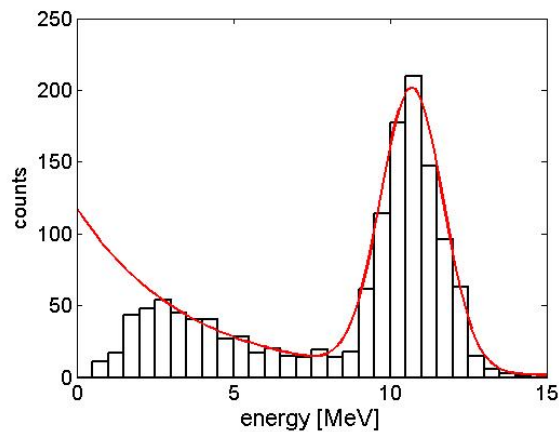


Figure 4.7: In this plot, the curve used as input for the calculation of the recoil spectra (red solid line) is compared with the measured spectrum (histogram). The curve is produced as the sum of a Gaussian centered at 10.7 MeV and an exponential curve.

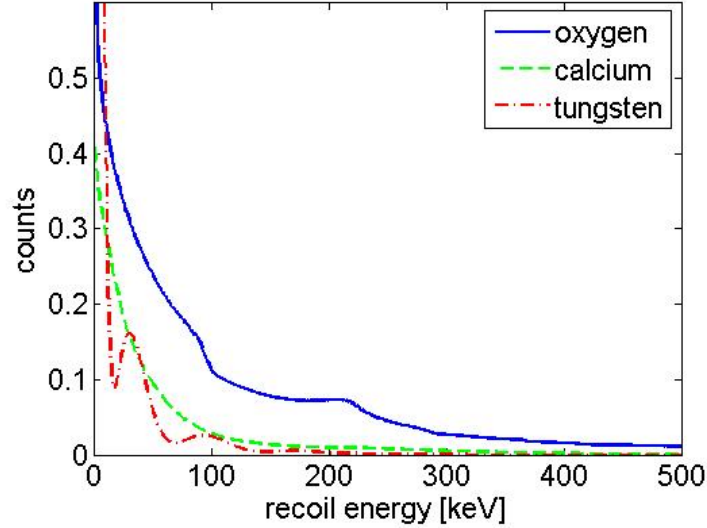


Figure 4.8: Calculated spectra of the energy recoils for oxygen, calcium and tungsten from irradiation with the ~ 11 MeV neutron beam from the accelerator.

It is interesting to compare the calculated recoil spectra for the different neutron sources (Am-Be and Cf, Fig.4.2; 11 MeV neutron beam, Fig 4.8), and to estimate the contributions of the different nuclei (oxygen, calcium and tungsten) to the total spectrum at various energies. An important point is up to which energy there is a significant contribution from tungsten. Given the high mass of this nucleus, the maximum recoil energy of tungsten for a neutron of energy 11 MeV is ~ 240 keV (from equation 3.3). In Table 4.1 the calculated contributions of the three different nuclei to the total recoil spectrum is given for different energy intervals. Since the goal is to separate the different contributions to the spectra, it is important to compare the expected rate of events from each nucleus in each energy interval. If the contribution of one of the three nuclei (for example tungsten) is very small compared to the others, it will be difficult to extract its quenching factor. At the same time, if the contribution of tungsten can be neglected, it will be easier to separate the contributions of calcium and oxygen. For this reason, contributions relative to oxygen are also given in every energy interval (second value in table 4.1).

The contribution of calcium is between 15% and 30% of the total, so always significant. The case of tungsten is more complicated: for neutrons from the ^{252}Cf source, the number of tungsten recoils is always negligible, given the low energy of the neutrons. In the case of $^{241}\text{Am-Be}$ source, tungsten gives a significant contribution up to ~ 150 keV. With 11 MeV neutrons the contribution of tungsten recoils is higher, and significant up to 200-250 keV (240 keV is the maximum transfer energy from an 11 MeV neutron to a tungsten nucleus).

Energy [keV]	^{252}Cf			$^{241}\text{Am-Be}$			11 MeV Beam		
	O	Ca	W	O	Ca	W	O	Ca	W
50-100	1000	211	21	1000	319	87.1	1000	302	140
	100 %	21%	2%	100 %	31 %	8.7 %	100 %	30 %	14 %
100-150	444	102	2.73	518	121	16.6	508	108	61.7
	100 %	22 %	0.6 %	100 %	23 %	3.2 %	100 %	21 %	12 %
150-200	410	67.6	0.41	415	75.5	3.10	407	62.4	25.7
	100 %	16 %	0 %	100 %	18 %	0.8 %	100 %	15 %	6.3 %
200-250	325	48.3	0	348	70.1	0.25	342	50.4	9.45
	100 %	12 %	0 %	100 %	20 %	0 %	100 %	15 %	2.8 %

Table 4.1: Calculated contributions to the recoil spectrum of the different nuclei for different energy intervals. The calculation is performed as described in section 4.1.2. The first value given is the absolute contribution, the second is the contribution relative to oxygen.

4.2 Experimental Setup

The detector module especially developed for our scattering experiment is a cryodetector based on the same working principle as that of the CRESST detectors described in section 2.1. The target material is a CaWO_4 single crystal, equipped with a TES as phonon sensor. The light detector, facing the crystal, consists of a silicon substrate, also equipped with a TES. In the following, a detailed description of the detector module itself and of the whole experimental setup is given.

4.2.1 Signal Response of the Crystal

The interaction of a particle with the CaWO_4 crystal produces two simultaneous signals: scintillation light (photons) and heat (phonons). Most of the energy, more than 95%, is converted into phonons, so that the amplitude of the phonon signal represents, in good approximation, the total energy of the interaction. The remaining part of the energy is converted into scintillation light. However, the amount of light produced by an interaction of a certain energy depends on the kind of interaction: electron recoils of a given energy produce much more light than nuclear recoils of the same energy. If both signals are recorded simultaneously, information not only on the amount of energy (phonon signal) but also information on the kind of interaction (light signal) can be obtained.

In Fig.4.9, an example of a measurement performed with γ and neutron sources is shown. This measurement was performed with the detector and experimental setup described in the sections (4.2.2 to 4.2.7). The γ s produce electron-recoil events, while the neutrons produce nuclear recoils. In the top plot of Fig.4.9 the two bands are clearly visible, corresponding to the two different kinds of events: given a certain energy of the interaction (x axis) two different light amplitudes (y axis) are possible depending on the kind of interaction.

For a more quantitative description of the discrimination capability, a new parameter is used, the light yield (Y). The light yield is defined as the ratio of the amplitude of the light signal and the amplitude of the phonon signal. Its value is normalized to 1 for electron recoil events at ~ 122 keV: in this way the light amplitude is measured in keV_{ee} (electron equivalent), which means that the light signal from an event of energy, for example, 100 keV will have an amplitude of 100 keV only if it is an electron recoil event. A nuclear recoil of the same energy will have a much lower value in keV_{ee} .

In first approximation, the light yield is independent of the energy, so that in a plot of the yield versus the phonon amplitude the bands corresponding to the different kinds of interactions are horizontal (see Fig.4.9, bottom).

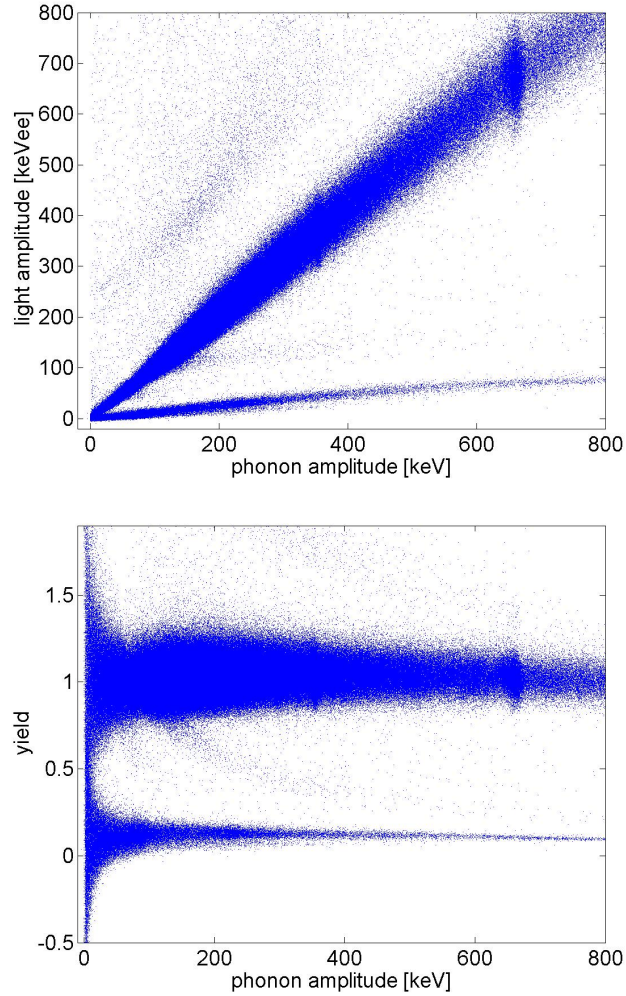


Figure 4.9: Data points from a measurement with γ and neutron sources. On top, the amplitude of the light signal versus the amplitude of the phonon signal is plotted. The upper band is the electron recoil band, the lower is the nuclear recoil band. The events above the γ band are random coincidences between a direct hit on the light detector and an event in the crystal. The plot on the bottom represents the light yield (normalized to 1 for electron recoil events) versus the amplitude of the phonon signal. In first approximation the light yield does not depend on the deposited energy. In this case the two bands are horizontal. Between the two bands, two populations of events are present. Such events are inelastic scattering of neutrons on a tungsten nucleus. Details on such events are given in section 5.2.2.4.

Another parameter, called the Quenching Factor (QF) is defined as the inverse of the light yield: $QF = 1/Y$. In the following, the parameter QF is used to characterize the light output of nuclear recoils. A higher QF therefore means a lower light output.

4.2.2 Readout of the Signals

The phonon signal is a calorimetric signal, which necessitates to read out an increase of the temperature. The amount of heat produced by an interaction of a particle is very small: in order to have a measurable increase of the temperature, the heat capacity has to be as small as possible. This can be achieved by going to very low temperatures (mK). Even so, the temperature increase is of the order of a few or a few tens of μK . In order to measure such a small change in temperature, a transition edge sensor (TES) is used. This kind of sensor consists of a film of a superconducting material evaporated onto the crystal. The temperature of the film is stabilized within its superconducting transition region (see Fig.4.10). In this region the resistance sharply drops to zero, so that a tiny change in the temperature results in an important change of the film's resistance.

The measurement of this small change in the resistance can be performed with a SQUID (Superconducting Quantum Interference Device). The film (resistance R_T) is part of a readout circuit as shown in Fig.4.11. The circuit has two parallel branches. In one of them is the TES (R_T), in the other a shunt resistance ($R_S \approx 10 \text{ m}\Omega$) is placed. A bias current I_0 (which is kept constant during operation) flows in the circuit. The way how this current is split between the two branches depends on the value of the resistances. A change of the resistance R_T of the TES due to a change in temperature produces a change in the current in both branches. In one of the two branches (in this case the one with the TES) the input coil of the SQUID is inserted. The change in the current produces a change of the magnetic field of the coil. This is coupled to the SQUID.

The choice of the material used for the TES depends on the performance

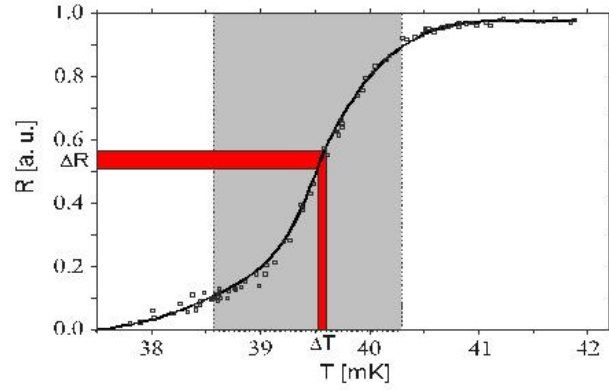


Figure 4.10: Schematic of the working principle of a TES. The gray area indicates the region of the transition, the red areas indicate the relation between a temperature change ΔT and the resulting change in resistance ΔR . The transition of the film to the superconducting state provides a step dependence of the resistance of the film on its temperature: a relatively small change in the temperature provides a measurable change of the resistance.

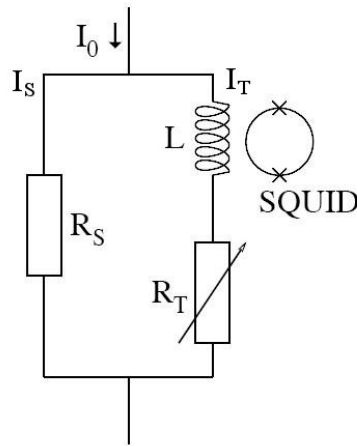


Figure 4.11: Read-out circuit of a TES. The (constant) bias current I_0 is split between the two branches of the circuit. The values of I_S and I_T depend on the values of the shunt resistance R_S and of the resistance of the film R_T . A change in the current through the input coil of the SQUID produces a signal in the SQUID.

required. In the CRESST experiment, tungsten films are used. This is due to the very low transition temperature of tungsten (in the alpha phase ~ 15 mK) which is responsible for the high sensitivity of the detector. A lower transition temperature means a lower heat capacity, and therefore a higher sensitivity. As will be explained later, for the measurements presented in this work other requirements are important and a different material (Ir-Au film) is chosen as TES.

The pulse shape of the phonon signals is related to the phonon collection and thermalization times. Slow phonon processes result in a slow pulse. The TES (its dimension and structure) can influence the collection time and consequently the shape and time constants of the pulses ([47] [70]). The configuration chosen for the detectors used in CRESST II produces pulses with a time constant of the order of ~ 10 ms. Since such detectors are run underground, in a low background environment, this comparatively very long time constant does not represent a limiting factor. The event rate for a 300g absorber in CRESST-II is less than one event per second so that even with such long pulses the fraction of pile-up events is low enough. Running such a CRESST-type detector on the surface, with much higher background, is not possible. Some modifications are necessary in order to perform characterization measurements on the surface. In section 4.2.3 the phonon detector used for the neutron scattering measurements is described in detail.

For the measurement of the scintillation light a cryogenic light detector is needed. A substrate (silicon on sapphire or pure silicon) is used as photon absorber. Photons absorbed by the substrate are also converted into phonons. These are then collected by a sensor of the same kind as the one used for the phonon signal. The readout is identical to that case.

4.2.3 Phonon Detector

CRESST detectors can stand a maximum rate of 0,5-1 Hz. In the low-background environment of an underground laboratory, this does not represent a problem, but on the surface, a 300 g detector would have a background

event rate of a few tens per second, which means that the signals would be dominated by pile-up. For this reason a detector to be used on the surface needs a special design.

The first and easiest thing that one can do is to reduce the dimensions of the crystal, thus reducing the overall event rate. However, in order to measure with a reasonably high rate it is very useful to reduce the decay time of the pulses.

In order to have faster pulses, the collection time of the phonons can be improved. This can be achieved by increasing the surface of the TES. A bigger TES, however, has a higher heat capacity, which reduces the pulse height. A solution to this problem is to introduce phonon collectors of a material with a transition temperature much higher than the operating temperature of the detector, e.g. Al. In this way, such collectors are superconducting and consequently their heat capacity is nearly zero. The absorption of phonons in Al, breaks up Cooper pairs, exciting quasiparticles (QP). The QP diffuse in all directions in the collector. When they reach the TES they can thermalise and release their energy in it. More details on this process are given in [47].

Moreover, the TES can be operated in the electrothermal feedback mode. The temperature of the detector is stabilized slightly below the transition temperature. The power dissipated by the current I_T in the film stabilizes it at a temperature that is slightly higher than the temperature of the thermal bath. The collection of the phonons produced by an interaction increases the temperature of the film, thus increasing its resistance. As a consequence I_T decreases, reducing the power dissipated and hence the temperature of the film. This means that in this configuration the film tends to self-stabilize at the operating point and allows higher count rates [47].

The phonon detectors used at our institute are provided with a TES based on a bilayer (Ir-Au) film. The advantage of this kind of film is that the transition temperature can be modified by changing the relative thickness of the layers. The transition temperature of the TESs used at our institute and based on Ir-Au bilayer films are between ~ 20 and ~ 60 mK.

For the choice of the operating point, the same procedure is followed for the phonon and the light detectors. The temperature of the holder is stabilized at a value below the transition temperature of the TES. The bias current is then set high enough to slightly warm up the TES and bring it into the transition region. The bias current is set to the value for which the signals of a given energy are maximized.

In Fig 4.12 a pulse from the phonon detector just described is shown. The decay time of the pulse is 3.5 ms. This means that this detector can stand a rate of ~ 25 Hz (in comparison to a maximum rate of 0.5-1 Hz of the CRESST detectors). However a 300 g detector is still too big to be operated on the surface, even with the phonon collector TES design. The phonon detectors used for characterization measurements at our institute have typically a diameter of 20 mm and a height of 10-20 mm.

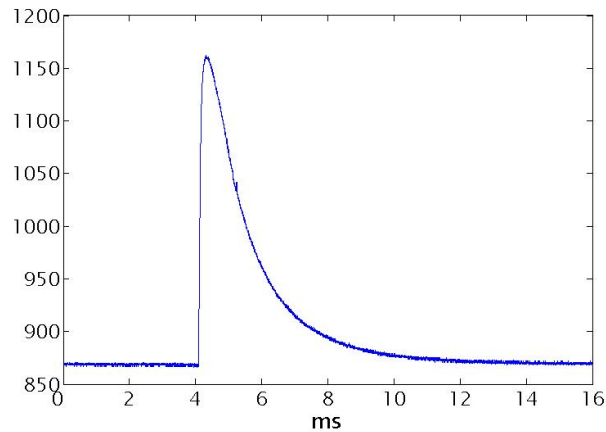


Figure 4.12: Example of a pulse from the phonon channel. The decay time of the pulse is 3.5 ms.

For the neutron scattering experiment another requirement has to be taken into account concerning the dimensions of the absorber: it is crucial to have the kinematics under control as much as possible (with the limits explained in section 3.2). If a neutron undergoes double scattering in the crystal, the two events cannot be separated, given the long time constants of the signals. This means that such an event will appear as one event having an energy equal to

the sum of the two recoils. If the two events are from two different kinds of nuclei, the light yield of the resulting “double event” will have an intermediate value, between the values of the events from each of the nuclei. If the number of double scattering events is high, this will worsen the separation of the bands corresponding to the nuclei O, Ca and W. In [66] and [71] the results of a measurement made with an Am-Be neutron source and with a CaWO_4 crystal of 20 mm diameter and 20 mm height are described. The separation of the bands is much worse than in the case of the smaller detector (20 mm diameter, 5 mm height) used for the measurements described in this work (section 5.3, Fig.5.23).

The mean free path of neutrons in CaWO_4 is ~ 6 cm. In [47] the results of simulations are shown, aimed at the determination of the contribution of double scattering for absorbers with different dimensions and with different orientations relative to the direction of the incoming neutrons. In table 4.2 these results are summarized. One can see that already in the case of a $20 \text{ mm} \times 20 \text{ mm}$ crystal the amount of double scattering is too high for the scattering experiment [47].

The detector used for the neutron scattering measurements presented in this work is a CaWO_4 crystal of 20 mm diameter and 5 mm height. For this crystal the fraction of double scattering is reduced to $\sim 7\%$ (see table 4.2) and the total scattering rate is still reasonable [47]. On the CaWO_4 crystal an elaborate TES has been realized. The structure of this sensor consists of a parallel connection of 28 individual Ir-Au films, each connected to 10 aluminum phonon collector fins, of area $50 \times 250 \mu\text{m}^2$ each. The total phonon collection area is then 3.5 mm^2 . Further details are given in [47].

In Fig.4.13 the phonon detector used in the neutron scattering measurement is shown. Fig.4.14 shows the transition curve of the TES. The transition temperature is ~ 60 mK. The main part of the transition is linear and its width is ~ 2 mK. The steepness of the transition assures a high sensitivity of the detector. Its linearity is important for a linear energy response of the detector (see section 5.2.1).

$\varnothing 40mm \times 40mm$ crystal			
	Scatter Prob.	Mult. Scatters	Fraction
From Side	$40.1 \pm 0.3\%$	$9.2 \pm 0.2\%$	$22.9 \pm 0.5\%$
From Top	$48.7 \pm 0.3\%$	$11.2 \pm 0.2\%$	$23.0 \pm 0.5\%$
$\varnothing 20mm \times 20mm$ crystal			
From Side	$22.8 \pm 0.3\%$	$2.88 \pm 0.11\%$	$12.6 \pm 0.5\%$
From Top	$28.4 \pm 0.3\%$	$3.59 \pm 0.12\%$	$12.6 \pm 0.5\%$
$\varnothing 20mm \times 5mm$ crystal			
From Side	$22.8 \pm 0.3\%$	$1.65 \pm 0.08\%$	$7.2 \pm 0.4\%$
From Top	$8.0 \pm 0.2\%$	$0.58 \pm 0.05\%$	$7.3 \pm 0.7\%$

Table 4.2: Results for the overall scattering probability and the multiple scattering probability obtained with a Monte Carlo simulation reported in [47]. Three different crystal sizes are considered, all of cylindrical shape. The dimension are given as *diameter* \times *height* in mm. The first column indicates if the neutrons are coming from the side or are hitting the flat face of the crystal. The second column indicates the probability that a neutron entering the crystal scatters at least once. The third column gives the probability that the neutron scatters more than once. The last column gives the probability of multi-scattering events relative to the total scattering probability.

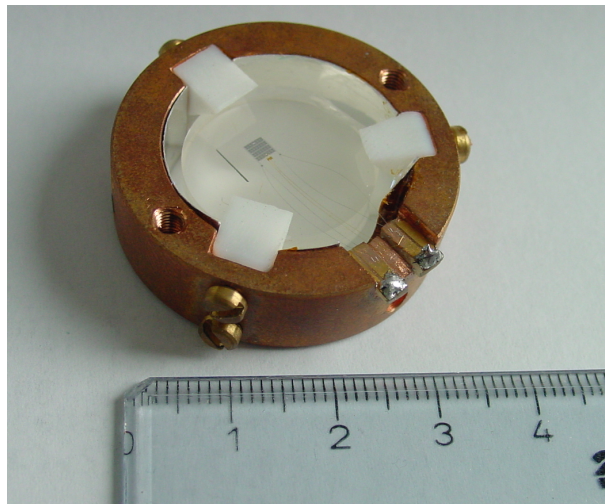


Figure 4.13: Picture of the phonon detector. The absorber is a CaWO_4 cylindrical crystal of 20 mm diameter and 5 mm height. The TES evaporated onto the crystal is highly elaborate (see text). The detector is enclosed in a copper holder. On the inner side of the holder a reflecting foil is placed for the collection of the scintillation light [47].

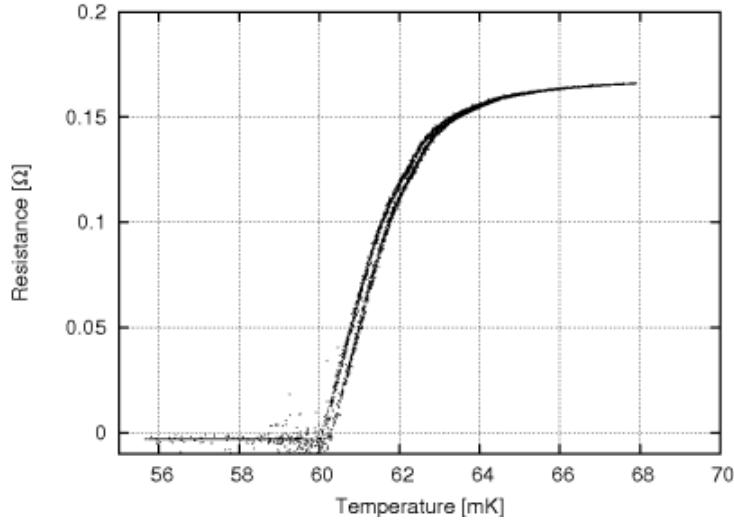


Figure 4.14: Transition curve of the Ir-Au TES of the phonon detector. The transition temperature T_c is ~ 60 mK and the temperature interval in which the transition takes place is ~ 2 mK. The steepness of the transition determines the sensitivity of the detector.

4.2.4 Light Detector

The light output of CaWO_4 for nuclear recoil events is relatively low. For measurements of the nuclear quenching factors (QF) an efficient light detection is crucial [72] [73] [74]. The light detector used consists of a silicon substrate, $20 \times 20 \text{ mm}^2$, with a thickness of $525 \mu\text{m}$ [47]. On top of the substrate a sensor is evaporated, of the same kind as the phonon sensor described above. In Fig.4.15 a picture of the light detector enclosed in a copper holder is shown. The copper holder can be screwed to the copper holder of the phonon detector (see Fig.4.13). In Fig.4.16 the transition curve of the TES of the light detector is plotted. Also in this case, as for the phonon detector, there is a large linear region in the transition from the normal to the superconducting state. Its width is ~ 2 mK.

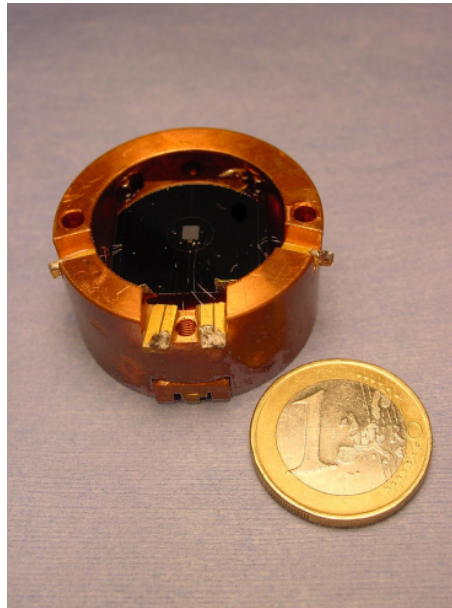


Figure 4.15: Picture of the light detector mounted in its copper housing [47]. The light detector consists of a silicon substrate ($20 \times 20 \text{ mm}^2$, with a thickness of $525 \text{ }\mu\text{m}$) onto which a TES is evaporated.

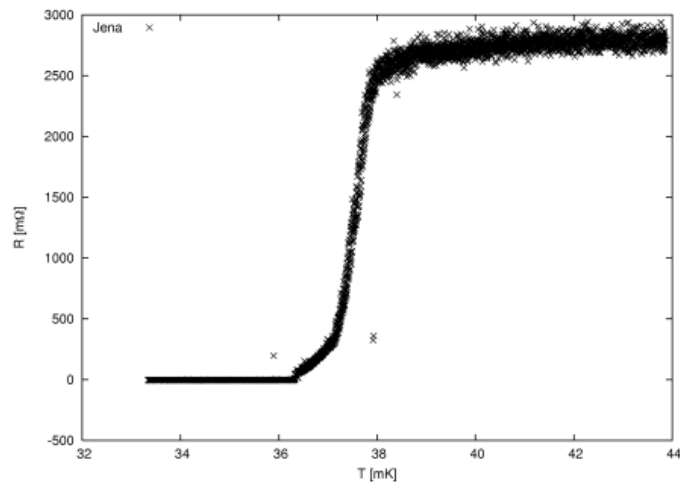


Figure 4.16: Transition curve of the Ir-Au TES of the light detector used for the neutron scattering measurements [47]. The transition temperature T_c is $\sim 38 \text{ mK}$ and the width of the transition is $\sim 2 \text{ mK}$.

4.2.5 Mounting the Detector Module

The phonon detector is mounted in a copper housing (see Fig.4.13). In order to maximize the light collection of the light detector, a reflective foil is placed all around the crystal. The detector is held in the housing by teflon holders on one side, and by CuBe springs on the other. Since CuBe remains flexible also at low temperatures, the springs reduce the mechanical stress on the detector. In a preliminary measurement, during which the detector was held on both sides by teflon holders, phonon-only events were observed, that disappeared after the introduction of the springs.

The copper holder is also used as a heat bath for the temperature stabilization of the detector. The holder is thermally connected to the mixing chamber of the cryostat by copper wires (1 mm thick). This thermal connection is weak enough that the detector can be heated to relatively high temperatures (up to $\sim 70 - 80$ mK) in comparison to the base temperature of the cryostat ($\sim 10 - 12$ mK), without causing too high a thermal load on the mixing chamber. The thermal contact between the holder and the detector itself is also weak and is realized by means of two thin gold wires (diameter $25 \mu\text{m}$) bonded to the holder and to the crystal.

A thermometer and a heater are fixed to the holder for temperature stabilization. The thermometer is a ruthenium oxide (RuO_2) resistor: the resistance changes relatively sharply in the temperature range $10 - 100$ mK (from $\sim 5 \text{ k}\Omega$ to $30 - 50 \text{ k}\Omega$) and is measured by a resistance bridge (Picowatt, AVS-47B). The resistance bridge is connected to a temperature controller (Picowatt, TS-530A), which regulates, by a PID controller, the power dissipated in the heater, stabilizing the temperature at the desired value.

The light detector is also held in a copper housing, which can be attached to the holder of the phonon detector. The thermal couplings (holder to mixing chamber and detector to holder) are realized in the same way as for the phonon detector. Also in this case a thermometer and a heater are fixed to the copper and connected to a second resistance bridge and temperature controller of the same type. In this way the temperatures of the two detectors

can be stabilized independently.

Since the transition temperatures of the phonon and the light detector TESs are rather different (light detector ~ 37 mK, phonon detector ~ 60 mK, see Figs. 4.14 and 4.16), it is necessary to thermally isolate the two copper holders. As one can see in Fig.4.17, a teflon ring is inserted between the two holders. In this way the stabilization of the temperature of one of the detectors does not affect the temperature of the other.

The module is fixed via copper rods to the mixing chamber plate of the cryostat and is located 31 cm below. The position where the detector has to be mounted is determined by the way the cryostat itself is held, since the detector must be at the height of the target cell, where the neutrons are produced. The installation of the cryostat is described in section 4.2.6. Care must be taken to thermally insulate the detector from the mixing chamber (the thermal contact, that has to be weak, is then realized by copper wires as described above). The insulation is obtained using Sintimid (a material with an extremely low thermal conductivity) for a part of the holding structure. In Fig.4.18 can be seen how the detector has been fixed to the mixing chamber plate. Being 31 cm below the mixing chamber, the detector is ~ 10 cm above the bottom of the inner vacuum chamber (IVC).

Below the detector, a ^{55}Fe source is mounted (not present in the pictures of Fig.4.17 and Fig.4.18, which were taken at an earlier time). The source is enclosed in a copper box with a 3 mm thick copper plate on top. Below the copper plate an aluminum foil (0.015 mm thick) is placed. The box is fixed at the detector holder by 7 cm copper rods. Through a hole of ~ 1 mm diameter in the copper plate the source irradiates the light detector from the bottom. In Fig.4.19 a schematic of the described setup for the ^{55}Fe source is shown. The ^{55}Fe source emits X-rays of energies 5.90 keV and 6.49 keV. A fraction of them reaches the light detector, another fraction excites the aluminum of the foil which then de-excites by emission of X-rays of 1.49 keV. This arrangement of the ^{55}Fe source and the Al foil allows an absolute calibration of the light detector (see section 5.2.2.1).

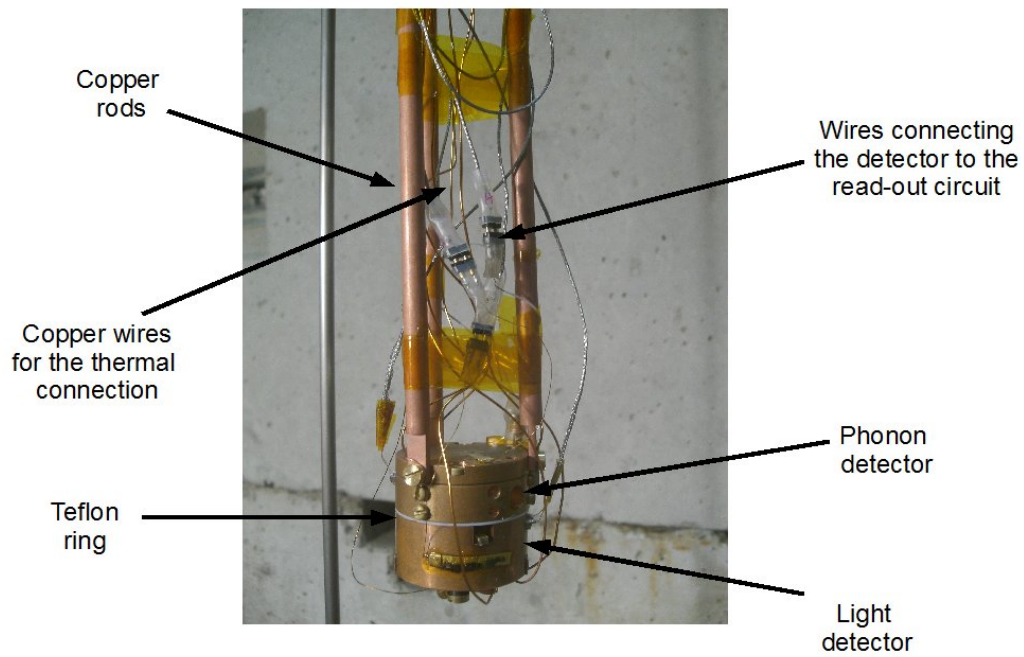


Figure 4.17: Detector module mounted in the cryostat. The upper part of the detector holder houses the phonon detector, the lower part the light detector. Both detectors are thermally isolated from each other by a teflon ring. The wires can be seen that provide the connection of the detector to the read-out circuit.

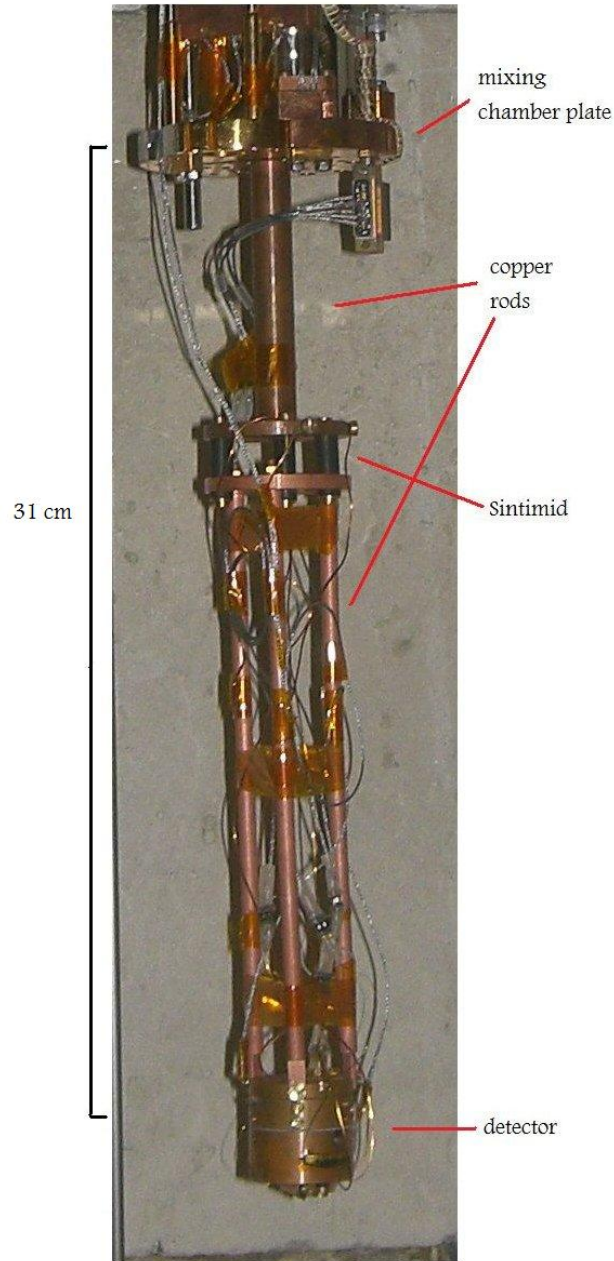


Figure 4.18: Picture of the structure connecting the detector to the mixing chamber plate. Most of the structure consists of copper rods. Sintimid is used for the thermal insulation of the detector from the mixing chamber.

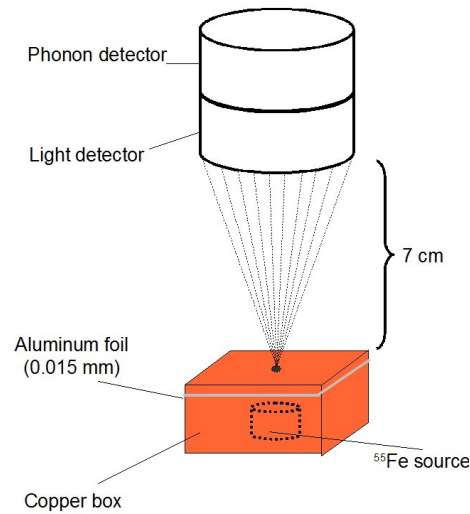


Figure 4.19: Schematic of the setup of the ^{55}Fe source for the calibration of the light detector. The source is placed in a copper box covered by a 3 mm thick copper plate with a hole of diameter 1 mm. The source emits X-rays of energy 5.90 keV and 6.49 keV. The Al of the foil, when excited by the interaction of an X-ray from the source, emits X-rays of energy 1.49 keV.

4.2.6 Installation of the Cryostat

The operation of the detectors requires temperatures in the range of some tens of mK. Such low temperatures can be reached with a ^3He - ^4He dilution refrigerator.

The cryostat installed is a Kelvinox 400 (Oxford Instruments). It has a base temperature of ~ 10 mK and a cooling power of $400 \mu\text{W}$ at 100 mK.

In the cryostat, two Supracon SQUIDs are installed (see below), so that a detector module (phonon and light detector) can be operated. An appropriate wiring had to be realized for the operation of the detector and read out of the signals. Some of the wires connect the coldest part of the cryostat to the environment at room temperature. In order not to transfer too much heat to the mixing chamber, which would prevent the cryostat from reaching the low temperatures needed, the wires have to be thermally coupled to different temperature stages so that most of the heat can be dissipated at higher temperature stages where the cooling power is high enough. The choice of the

material of the wires is also crucial in order to prevent too high a thermal load. In the following a description of the wiring is given. In Fig.4.20, a schematic of a dilution refrigerator is shown, in which the different temperature stages are indicated.

A vacuum-tight Lemo connector with 24 pins placed on top of the cryostat provides the feedthrough of the cables from the external electronics to the cryostat. Wires of different materials have been used, depending on the required features. In most cases shielded Nb-Ti wires have been installed, which are superconducting at the liquid-helium temperature. Superconducting wires, having a very low heat conductivity, prevent a heat flow from the warmer parts to the colder. In the utilized cables, the Nb-Ti wire is enclosed in a teflon mantle as electrical insulator, around which a metal shield is placed. This avoids the pickup of electrical noise by the wire.

For each channel (phonon and light) 8 wires go through the Lemo connector (at room temperature) into the cryostat. Two of them are the detector bias lines that go directly to the mixing chamber plate. For these lines shielded Nb-Ti wires are used. The other 6 lines are connected to the SQUID. Two provide the voltage to the SQUID, two go to the feedback coil and two are the connections to a heater needed to warm up the SQUID above the transition temperature, in the case of trapped magnetic flux quanta.

The SQUIDS are placed in the inner vacuum chamber (IVC) (see Fig.4.20). To operate the SQUIDS, their temperature has to be lower than 5 K. Since these devices are sensitive to changes of the magnetic flux, they must be shielded against external magnetic fields. For this reason they are enclosed in a Nb housing. Nb, being superconducting below 9.5 K, provides a very efficient shielding against external magnetic fields. The housing is fixed to the plate of the cryostat which is at ~ 1 K. On the other hand, being superconducting, the housing is a good thermal insulator, preventing the SQUID itself from cooling down. The cooling of the SQUID must then be achieved in another way. In our case the wires that provide the electrical connections are also responsible for cooling the SQUIDS.

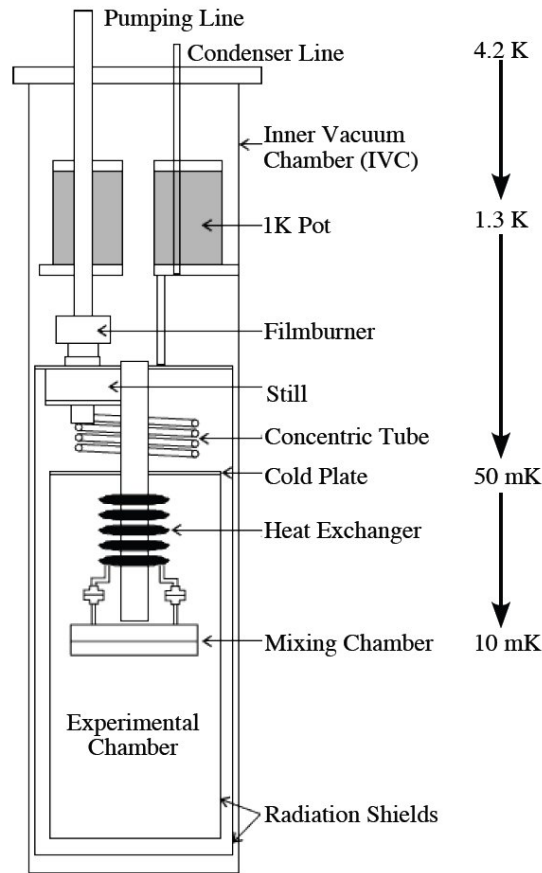


Figure 4.20: Schematic of a dilution refrigerator with indication of the different temperature stages (drawing from [75]).

For the SQUID voltage, copper lines are recommended, because of the low resistance (Nb-Ti has a relatively high resistance when it is not superconducting and a part of the line does not reach a temperature below the transition). The copper lines used are also shielded in the same way as described for the Nb-Ti. For all the other connections (feedback coil and heater) shielded Nb-Ti wires are used.

All the lines are clamped between two copper plates thermally coupled to the 4 K plate of the cryostat (the plate at the top of the inner vacuum chamber). The teflon shielding, however, prevents them from being effectively

cooled by the clamp. Thus, as already mentioned, the lines to the SQUIDs must also provide the cooling. Therefore it is crucial that the thermal contact of the wires to parts of the cryostat that are at 4 K or at a lower temperature is good and that they are able to dissipate the heat of the SQUIDs. For this reason, for the last few centimeters unshielded copper wires are used. These are thermally coupled to the 1 K plate by an additional copper clamp, to which they are fixed in addition by GE-Varnish, that ensures a good thermal contact. Since they are not shielded, each pair of the lines (voltage, feedback coil, heater) is twisted in order to reduce noise pickup.

The bias-current lines, as all the other lines, are clamped first at 4 K, then at the still (~ 0.7 K). They end up in the shunt box, which is a copper box where the splitting of the circuit into the two current branches (see Fig.4.11) needed for the readout is achieved. The shunt resistance is also placed inside the box, which provides electronic shielding of the circuit. The box is screwed to the top of the mixing chamber plate, to achieve good thermal contact. To connect the film to the read-out circuit (see Fig.4.11), two shielded Nb-Ti wires go from the box to the detector. Two additional shielded Nb-Ti lines connect the input coil of the SQUID to the rest of the read-out circuit (within the shunt box). Also these two lines are thermally coupled to the still plate.

The detector has to be at the height of the beamline, which is at ~ 1.5 m from the floor. For this reason the cryostat is held by a metal structure above the beamline. The helium bath, needed to provide a cold environment for the dilution refrigerator, as well as all other materials between the target cell and the crystal, can represent an obstacle for the experiments: the neutrons from the beam can scatter on the helium, so that their energy and direction can change. This can be a problem especially if one wants to perform measurements at fixed scattering angles. It is thus preferred to minimize the amount of helium surrounding the detector. For this reason a specially designed dewar has been used. This has a smaller diameter in the bottom part (where the detector is placed) so that only a few centimeters of helium are between the target cell and the detector. In section 5.1 the results of

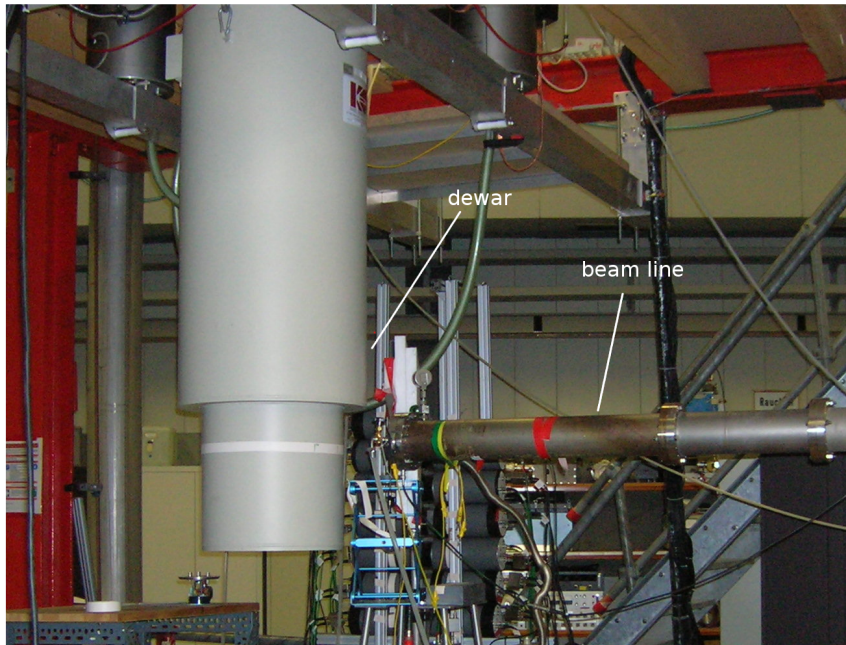


Figure 4.21: Picture of the setup at the MLL. The beamline and the dewar of the cryostat can be seen.

measurements are shown where the influence of different materials on the beam profile was investigated. From these measurements we have seen that the helium still present does not seriously compromise the measurements. In Fig.4.21 a picture of the setup is shown, where the specially designed dewar is visible.

Cryogenic detectors are very sensible to vibrations. For this reason the cryostat has to be mechanically isolated as much as possible from the environment. This is achieved by the introduction of air dumpers that decouple the cryostat from the holding structure. Much care has been taken to also minimize the mechanical coupling of the pumps (necessary for the operation of the cryostat) to the structure holding the cryostat. More detail concerning the installation of the cryostat will be given in [76].

4.2.7 Data Acquisition

The signals from the cryodetector are amplified and filtered at the top of the cryostat, in order to minimize the impact of noise picked up outside of the cryostat. For a detailed description of the electronics of the signal formation and processing see [76].

For the analysis of the data from the cryodetector the complete pulse shape is needed (see section 5.2). Two different data acquisition systems were used for the measurements described in this work.

The data acquisition originally associated with the setup is a CAMAC system optimized for the coincidence measurement described in section 3.2.1 [60]. A transient recorder (Joerger TR 612/3) was used for the acquisition of a complete pulse. The transient recorder has four input channels and a trigger input: the two signals from the cryodetector (phonon and light signals) are recorded by two of the channels of the transient recorder. The sampling rate of the transient recorder can be varied from 100 kHz to 3 MHz. For the measurement presented here, a sampling rate of 1 MHz was chosen.

To generate the trigger signal, an oscilloscope was used. Trigger thresholds were set for both the phonon and the light channel. The oscilloscope provides a trigger output (which corresponds to a logical OR-gate), that can be connected to the trigger input of the transient recorder. For neutron and γ events one needs to trigger on the phonon channel. The light pulses for nuclear recoil events can be so small that the trigger threshold could end up in the noise. The bigger phonon pulses, on the other hand are best suited to set a trigger threshold. To record events from the ^{55}Fe source, it is necessary to trigger on the light channel, since no phonon signal is associated to such events (see section 5.2.2.1).

By setting the trigger output of the oscilloscope to the OR-configuration, it is possible to acquire both ^{55}Fe events and neutron- γ events at the same time.

Since for the measurements performed with the cryodetector alone the coincidence part of the electronics was not needed, for one of the sets of

measurements a different acquisition system was used. This system is based on a PXI crate from National Instruments. Acquisition software has been used, that has been optimized for the cryodetector signals and for this data acquisition system. Also in this case the signals were acquired with a sampling rate of 1 MHz. The trigger system was integrated into the data acquisition system and, as in the previous case, it was possible to choose to trigger on one of the two channels or on both simultaneously. This acquisition system is described in detail in [47].

The CAMAC system (described in detail in [60]) includes the acquisition electronics needed for the neutron detectors and for the coincidence measurements described in section 3.2.1. In the frame of this work, part of this electronics was used for the measurements of the beam spectrum and the beam profile (see sections 4.1.3 and 5.1).

Chapter 5

Measurements: Results and Discussion

Two different kinds of measurements will be presented in this chapter. The first set of measurements investigated the profile of the 11 MeV neutron beam obtained by the reaction $p(^{11}\text{B},n)^{11}\text{C}$ at the tandem accelerator of the MLL, in particular how the profile is influenced by the presence of various materials. In the second part of this chapter, the measurements performed with the cryodetector setup installed at the MLL (described in section 4.2) are presented. The results for the quenching factors and the phonon quenching will be described in the last two sections.

5.1 Measurement of the Beam Profile

For the investigation of the response of the cryodetector, measurements with neutrons from different sources have been performed. Besides standard neutron sources (^{252}Cf and $^{241}\text{Am-Be}$) an 11 MeV neutron beam produced by the tandem accelerator at the Maier-Leibnitz-Laboratorium in Garching has been used. In section 4.1.3 the nuclear reaction used to produce this beam is described.

Knowing the energy spectrum of the source is crucial for understanding

the results of a neutron scattering measurement. The presence of the cryostat can also influence the energy spectrum of the neutrons and the profile of the spectrum. It is then interesting to investigate how different materials and the cryostat itself can modify the profile of the beam. This is the goal of the measurements described in this section.

To measure the beam profile in different conditions, seven neutron detectors have been used. The energy is determined by measuring of the time of flight (ToF) of the neutrons. The measurement technique and the detectors used are described in section 4.1.3.

The seven neutron detectors are placed at different angles (see Fig.5.1), so that each detector measures simultaneously the energy spectrum of the beam at the chosen angle. The shape of the spectrum at a given angle depends only on the kind of reaction: in this case the only parameter that can change the shape of the spectrum (position of the main peak, shape of the tail, amplitude ratio between peak and tail) is the energy of the ^{11}B beam, which is kept constant with high precision. On the other hand, the amplitude of the spectrum depends on the measuring time, on the beam current (number of ^{11}B ions that reach the target cell per unit time) and on the conditions of the hydrogen in the target cell (pressure, cleanliness). The beam current and the condition of the target determine the number of ^{11}B ions that react per unit time and consequently the rate of produced neutrons. These parameters are difficult to keep under control, so that spectra measured at different times cannot easily be compared quantitatively. However, the possibility to measure several spectra simultaneously, as we did for different angles, allows us to make a quantitative comparison of the characteristics of the beam at different angles. The absolute number of events, however, for the measurements performed in different conditions cannot be compared.

For a quantitative comparison, the different efficiencies of the detectors have to be taken into account. The efficiencies were determined with a series of dedicated ToF measurements where two of the neutron detectors were placed near to each other at $\sim 0^\circ$. In this configuration, the two detectors

are hit by the same flux of neutrons. The measurement was repeated 6 times, for six couples of detectors: one of the detectors was always the same (the reference detector) and the second was in turn one of the other 6. The neutron energy spectra measured by each couple were divided in 1 MeV bins. The rate measured in each bin by the investigated detector was compared with the rate measured by the reference detector for the same energy bin. For each detector, a normalization factor was calculated as a function of the energy. In this way, also the possibility of an energy dependence of the efficiency is taken into account. By analyzing the measurements performed at the different angles, the measured rate for every energy bin was multiplied by the normalization factor obtained with the efficiency measurement.

5.1.1 Profile of the Beam itself

First a measurement was performed to determine the profile of the neutron beam as it is produced. Measurements were carried out with two different configurations of the neutron detectors, as depicted in Fig.5.1. In table 5.1 the angles at which the detectors were placed in the two configurations are listed. The radial distance of the detectors from the H₂ target cell was 163 cm. The fact that the detector placed at 0° was not moved allows to find the normalization factor for the neutron flux for the two measurements, so that the results can be compared.

Configuration 1	0°	16°	34°	48°	64°	90°	120°
Configuration 2	0°	8°	26°	40°	54°	70°	120°

Table 5.1: Positions of the neutron detectors (angle relative to the beam axis) for the measurement of the beam profile (see Fig.5.1).

In Fig.5.1 a schematic of the measurement setup is shown. The rectangles represent the neutron detectors. The full ones are in the positions corresponding to configuration 1, the dashed rectangles represent the positions of the detectors in configuration 2. In Fig.5.2 the spectra measured at the different

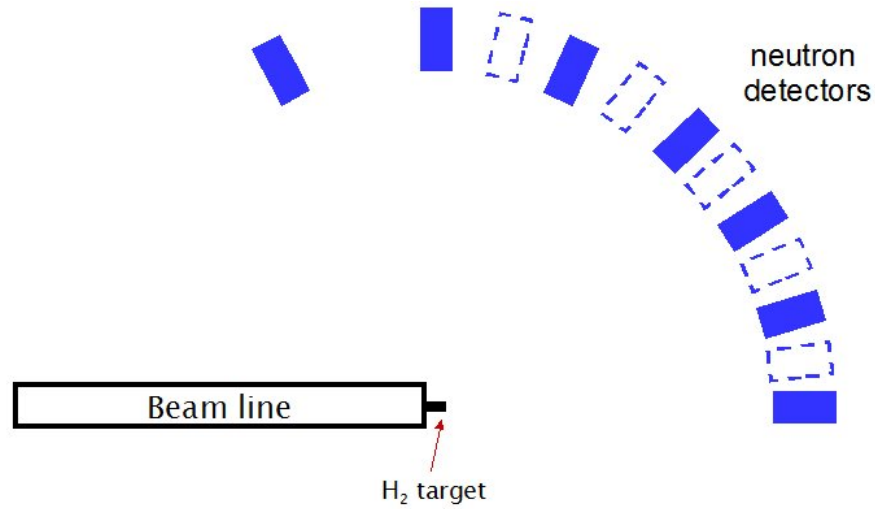


Figure 5.1: Scheme of the detector setup for the measurement of the beam profile. The rectangles represent the neutron detectors positioned at the different scattering angles. The full ones represent the positions in configuration 1 (0° , 16° , 34° , 48° , 64° , 90° , 120°), the dashed ones represent the positions in configuration 2 (0° , 8° , 26° , 40° , 54° , 70° , 120°). The detectors at 0° and 120° were not moved between the two configurations.

angles are plotted. At 0° the main peak is centered at 11 MeV, which is shown in the spectrum depicted in Fig.4.6. Increasing the scattering angle, the main peak appears at lower energies. The largest angle at which a peak is observable (at an energy of 3 MeV) is 40° . At angles larger than 40° (Fig.5.2, bottom panel) the main peak disappears, as expected from the kinematics of the reaction (see section 4.1.3).

5.1.2 Profile with Materials

After these measurements where the profile of the neutron beam as produced by the accelerator was investigated, a set of experiments was performed, to investigate how this profile is influenced by the presence of materials between the neutron source and the neutron detectors. In particular, it is interesting to see how the relative amplitudes of the main peaks at different angles change. The presence of material in the way of the neutrons, can let some of them

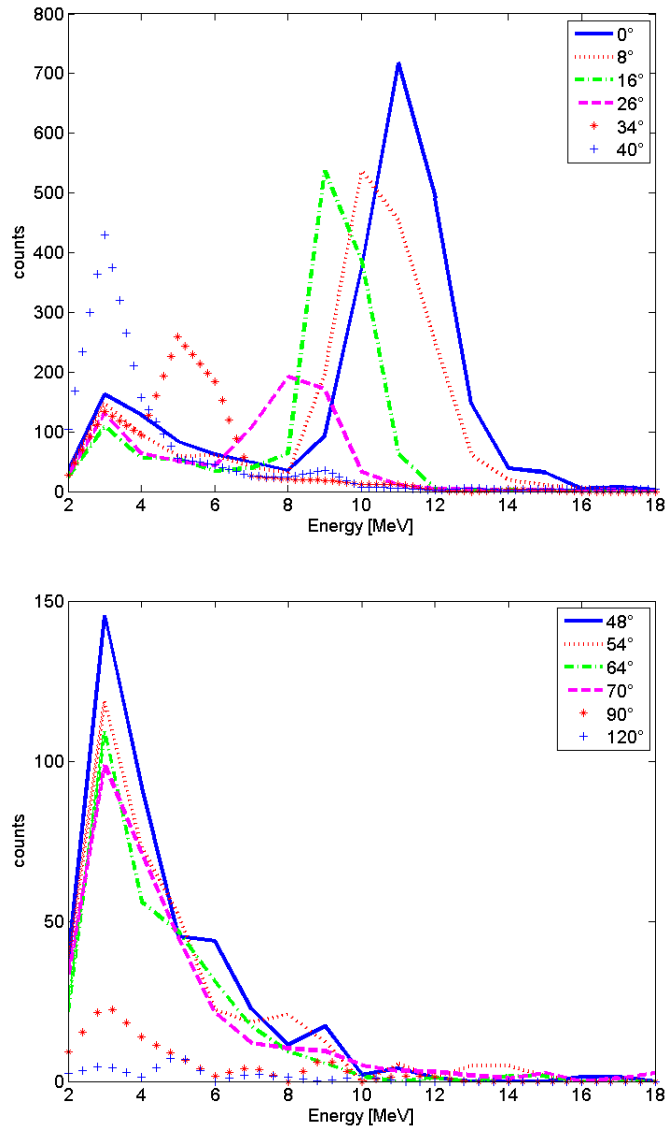


Figure 5.2: Measured neutron spectra at different scattering angles. In the top panel, the spectra measured at angles up to 40° are plotted. The main peak is at 11 MeV for the neutrons scattered at 0° . It then moves to lower energies for bigger scattering angles. The bottom panel shows the spectra measured at larger angles (48° to 120°). At these angles, only a background of low energetic neutrons is measured. This is consistent with the expected profile: for kinematic reasons, the neutrons produced in the reaction are collimated within angles smaller than $\sim 45^\circ$. Note the different scale between the two plots.

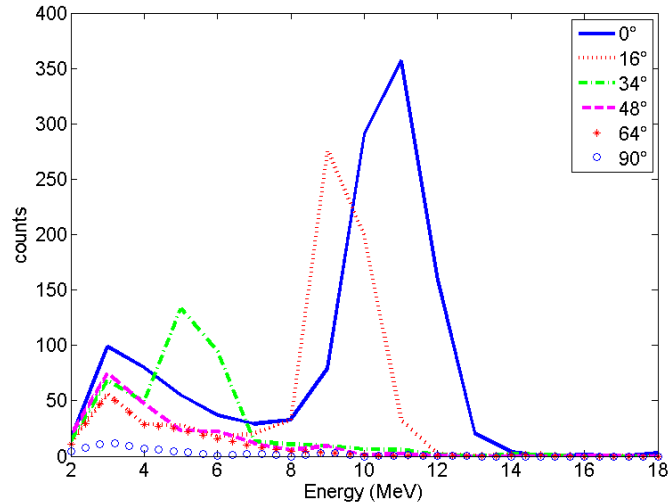


Figure 5.3: Beam profile measured without material in the way of the neutrons. The spectra shown here are those measured at the angles denoted in table 5.1 as “configuration 1”.

scatter so that they are removed, for example, from the peak at 0° , but contribute to the peaks at some other angles. Particularly interesting is the investigation of the increase of neutrons at angles larger than 40° . Such neutrons, in fact, produce background events for a scattering experiment like the one described in section 3.2.1.

Two sets of measurements are presented here. In the first case, lead was positioned in front of the target cell in different geometries and thicknesses. In the second case, measurements were performed with the cryostat in the same position as during the measurements with the cryodetector. In both cases, the neutron detectors were always positioned in the configuration called “configuration 1” in table 5.1, so only the spectra at these angles were measured. To facilitate the comparison of the profiles in the different measurements (no material, lead, cryostat) it is useful to look at Fig.5.3 as reference.

- **Lead**

This measurement was realized putting lead bricks in front of the cell. The lead bricks used have the shape of a parallelepiped with dimensions

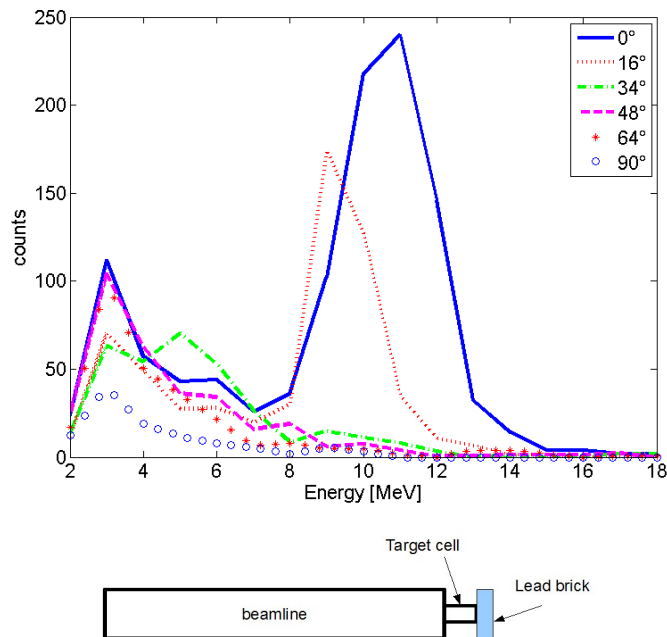


Figure 5.4: Neutron profile measured with a lead brick (5 cm) placed in front of the target cell. The way the brick was positioned is shown at the bottom of the figure. Comparing the spectra measured in this configuration with the ones of Fig.5.3 one can deduce that the presence of the lead does not strongly influence the profile since the relative amplitudes of the spectra at the different angles do not change significantly.

of 5 cm \times 10 cm \times 20 cm. The measurement of the profile was repeated for three different configurations of the lead bricks in front of the cell. In Figures 5.4, 5.5, and 5.6 the measured spectra in the three cases are plotted. In the bottom panel of each figure, a schematic drawing of the position of the lead brick is shown.

Fig.5.4 shows the profile of the beam with one lead brick positioned in front of the target cell in such a way that the neutrons emitted at 0° have to pass through 5 cm of lead. As already mentioned at the beginning of this section, the absolute number of events does not give any information. The relative intensities of the main peak at the different angles, however, is very similar to the case without material (Fig.5.3),

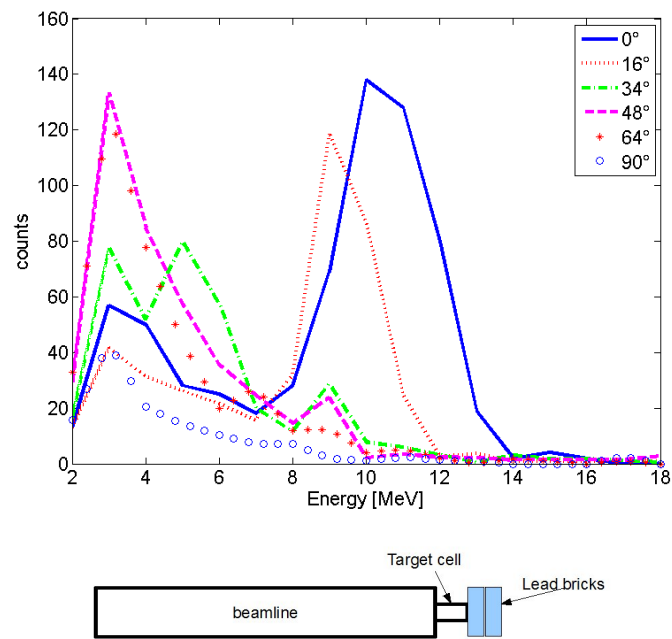


Figure 5.5: Neutron profile measured with 10 cm of lead in front of the target cell (two lead bricks, positioned as shown at the bottom). In this case the relative amplitudes of the spectra change strongly, compared to the spectra shown in Fig.5.3. In particular, the spectra at large angles are enhanced in comparison to the spectra at small angles, indicating that a significant part of the neutrons produced at small angles are scattered by the lead.

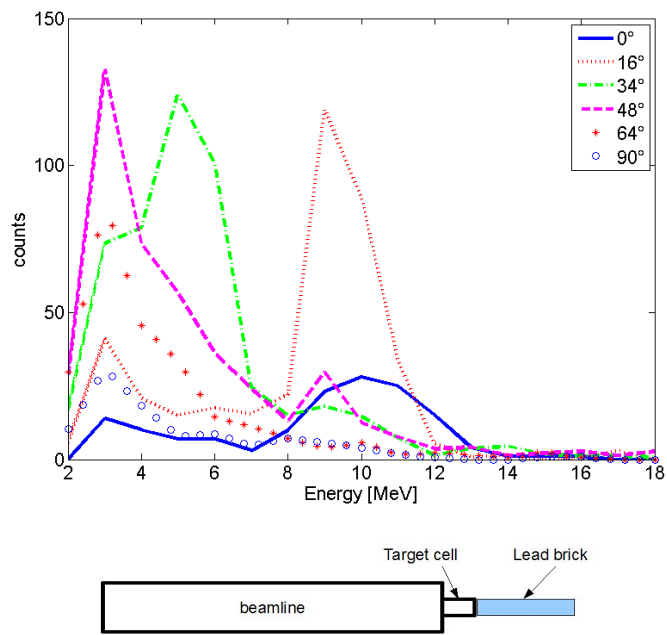


Figure 5.6: Neutron profile measured with one lead brick in front of the cell. Differently from the case shown in Fig.5.4, the brick is positioned in a way that neutrons produced at 0° have to cross 20 cm lead (schematic on the bottom). In this case, the 11 MeV peak at 0° almost disappears, while the spectra at larger angles are strongly enhanced.

and the spectra at angles larger than 45° do not show an enhancement. This demonstrates that the profile is only slightly influenced by the presence of the 5 cm thick lead brick.

The case with two lead bricks in front of the cell is different (Fig.5.5): The neutrons emitted at 0° have to pass through 10 cm of lead. The relative intensities of the spectra at different angles are now clearly different from the case without material (Fig.5.3). In particular, the ratios between the peaks of the spectra at small angles (0° and 16°) and the peak of the spectrum at 34° are clearly reduced and also the spectra at angles larger than 45° show a strong enhancement. This indicates that a significant part of the neutrons emitted at small angles interact in the lead and are scattered at large angles.

For the last measurement of this set, one lead brick was used, but it was positioned so that the neutrons emitted at 0° had to pass through 20 cm of lead (Fig.5.6). In this case most of the neutrons emitted at 0° are scattered away, as is evident from the strong suppression of the peak of the spectrum measured at this angle. The spectra at large angles, similarly to the case with 10 cm, are strongly enhanced by the neutrons scattered by the lead.

- **Cryostat**

Finally, the beam profile has been measured, placing the cryostat at the same position as for the measurements with the cryodetector. It is important to investigate how strongly the presence of the cryostat and of the liquid helium influences the neutron beam, in order to better understand the results obtained with the cryodetector.

For this measurement, the cryostat was filled with liquid helium, in order to reproduce the operating conditions. The measurement was performed two times: in the first case, the insert of the cryostat was placed in its operating position. In the second case, the insert was partially pulled out, in order to investigate the influence of the liquid

helium on the neutron beam in greater detail.

In Fig.5.7 the spectra measured in these two configurations are shown. Again, in order to understand what the effect of the presence of the cryostat amounts to, we need to compare the plots of Fig.5.7 with that of Fig.5.3.

In the first case, the spectra (see Fig.5.7 top) are very similar to those without material, The relative intensity of the peak at 11 MeV (0°) to the peaks at other angles, is similar as in Fig.5.3. This clearly indicates clearly that the cryostat does not strongly influence the neutron beam.

In the measurement performed with the insert of the cryostat pulled out, an influence on the profile can be noticed (see Fig.5.7 bottom). The peak at 0° is shifted to a slightly lower energy, and the intensities of the spectra at small angles are reduced in comparison to the spectra at larger angles. This indicates that the liquid helium significantly influences the neutron beam. However, with our cryostat, this effect is reduced due to the shape of the dewar, that is reduced in diameter at the part surrounding the cryodetector (see Fig.4.21).

5.2 Measurements with the Cryodetector

Several measurements have been performed with the cryodetector described in section 4.2. In this configuration the cryostat was kept cold for several weeks during February-March 2008. This condition permitted to measure continuously without changing the working points (temperature and current chosen for the stabilization) of the phonon and light detectors. In this period, a measurement with the 11 MeV neutron beam was performed (one week), followed by measurements with the ^{252}Cf and $^{241}\text{Am-Be}$ neutron sources (one week for each source). For this whole set of measurements a transient recorder was used to record the pulses (section 4.2.7) [60].

In April 2008, another measurement with the 11 MeV neutron beam was performed for one week. Between the measurements in March and April the

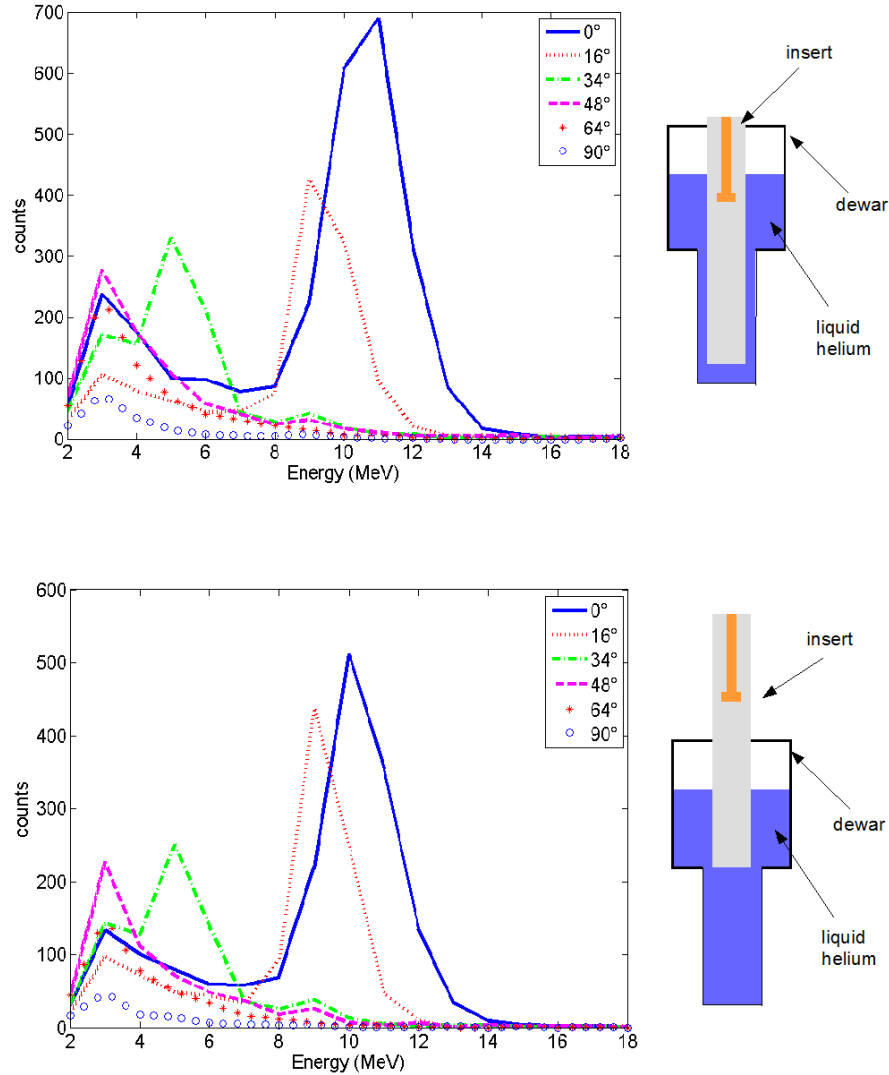


Figure 5.7: Neutron profiles measured with the cryostat in its operating position and filled with liquid helium. During the measurement of the spectra in the top panel, the insert of the cryostat was also in the operating position (see schematic on the right). These spectra are very similar to those measured without material (Fig.5.3), which indicates that the cryostat does not deeply influence the profile of the beam. For the measurement of the spectra plotted in the bottom panel, the insert of the cryostat has been pulled out (see schematic on the right), so that a greater amount of liquid helium is in the way of the neutrons to the detectors. In this case the energy of the peak at 0° is shifted to lower values and the intensity of the spectra at small angles is reduced with respect to those at larger angles.

cryostat was warmed up, so that the working point had to be set again. For this measurement a different data acquisition system was used, based on a PXI crate (section 4.2.7) [47].

Since the measurements of February, March and April were performed in the same conditions, and also the chosen working points have very similar characteristics, they can be discussed together. This will be done in the next sections 5.2.1 and 5.2.2.

The aim of the measurements was the characterization of the response of the CRESST detectors to different kinds of interactions (electron recoils or recoils of different nuclei). In particular, the measurement of the light yields produced by the recoils of the different nuclei present in the CaWO_4 detector would help to discriminate the neutron background in the CRESST experiment. This point was described in detail in section 3.1, where also the quenching factor (QF) was introduced.

Besides the QF, it is also interesting to determine the so-called phonon quenching (see section 5.4). This is defined as the ratio between the energy of the phonon signal of a nuclear recoil and the energy of the phonon signal of an electron recoil, for the same recoil energy.

$$PQ = \frac{E_{ph}^{(n)}}{E_{ph}^{(e)}} \quad (5.1)$$

It turned out that this effect is of the order of $\sim 8\%$ (see section 5.4). In first approximation, one can consider it negligible, as will be done in part of this work.

Phonon quenching is strictly related to light quenching. If one assumes that the energy of an interaction is distributed only between the phonon and the light signals, without the intervention of other mechanism, the two situations (relative to electron and nuclear recoils) can be summarized in the following way:

$$E_{ph}^{(e)} = E - E_{li}^{(e)} \quad (5.2)$$

$$E_{ph}^{(n)} = E - E_{li}^{(n)} \quad (5.3)$$

where E is the energy of the interaction, $E_{ph}^{(e)}$ and $E_{li}^{(e)}$ are the parts of E converted, respectively, into phonons and light if the interaction with energy E was an electron recoil event. $E_{ph}^{(n)}$ and $E_{li}^{(n)}$ are the corresponding parts, in the case that the energy E was released as a nuclear recoil. Since, for a fixed value of E , $E_{li}^{(n)}$ is smaller than $E_{li}^{(e)}$, $E_{ph}^{(n)}$ will be bigger than $E_{ph}^{(e)}$. Consequently, just applying the phonon calibration curve found for the electron recoil band, to the nuclear recoil band produces an overestimation of the energy for nuclear recoil events. In order to evaluate this error, at least one group of events of known energy has to be in the nuclear recoil band.

In the following sections (5.2.1 and 5.2.2) the procedure is described, that has been used to determine the energy of the pulses for both the phonon and the light detector and for the two different kinds of events (electron recoils and nuclear recoils).

5.2.1 Phonon Channel

5.2.1.1 Pulse Shape

The shape of the pulses produced by the TES depends on the shape of the superconducting transition of the film (steepness, linearity) in the region of the chosen working point (temperature and current chosen for the stabilization), and on the characteristic time constants of the production and absorption of the phonons.

As already mentioned (see [47] and section 4.2.3) the TESs are operated in the so-called electrothermal feedback mode. In this mode, the temperature increase of the film, generated by the absorption of phonons, is partially compensated by a decrease in the bias current. This mechanism, however, is not fast enough in comparison to the energy transfer to the film, so that the temperature increases and the position on the transition curve changes. As long as the temperature is such that the film remains in the linear region

of the transition, the shape of the pulse is independent of the energy of the interaction. For higher energy deposition, the film leaves this linear region of the transition, and the shape of the pulse differs from the shape of small pulses. If the energy transfer is high enough, the film ends up in the normal-conducting phase and the pulse saturates, since in the normal conducting region the relation between the temperature and the resistance is by far not as steep as in the transition region.

In Fig.5.8 two pulses from the phonon detector are shown. The pulse on the top panel is small enough so that the film does not exit the linear region of the transition. The shape of such pulses is, in first approximation, independent of the amplitude of the pulse itself, so that the pulse height is proportional to the energy of the interaction. The pulse on the bottom panel is an example of a saturated pulse. In this case the pulse height is only weakly depending on the energy of the interaction. On the other hand, the lower part of the pulse is generated in the linear region of the transition, so that its shape is the same as the corresponding scaled fraction of the small pulses. For the chosen working point, the non linearity starts at an amplitude of ~ 150 , in arbitrary units (a.u.), corresponding to ~ 130 keV.

For high-energy events, another phenomenon can occur, not related to the pulse generation, but to the read-out. The read-out of the pulses is performed by means of a SQUID operated in feedback mode, in order to keep it in the working point. For high-energy events, the change in the current can be too fast for the feedback to follow, and the SQUID can jump to a new working point, which differs from the original one by one or more flux quanta [51]. In Fig.5.9 a pulse is shown, for which three flux quanta were lost.

For the measurements described in this section, this phenomenon appears already at ~ 200 keV. Above ~ 500 keV in almost all cases one or more flux quanta are lost. This means that if we simply would reject such pulses, we would measure only in a very limited energy range. However, it is possible to reconstruct off-line the pulses as they would look like with no flux quanta lost. The loss happens in the rising edge of the pulse, so that the falling edge

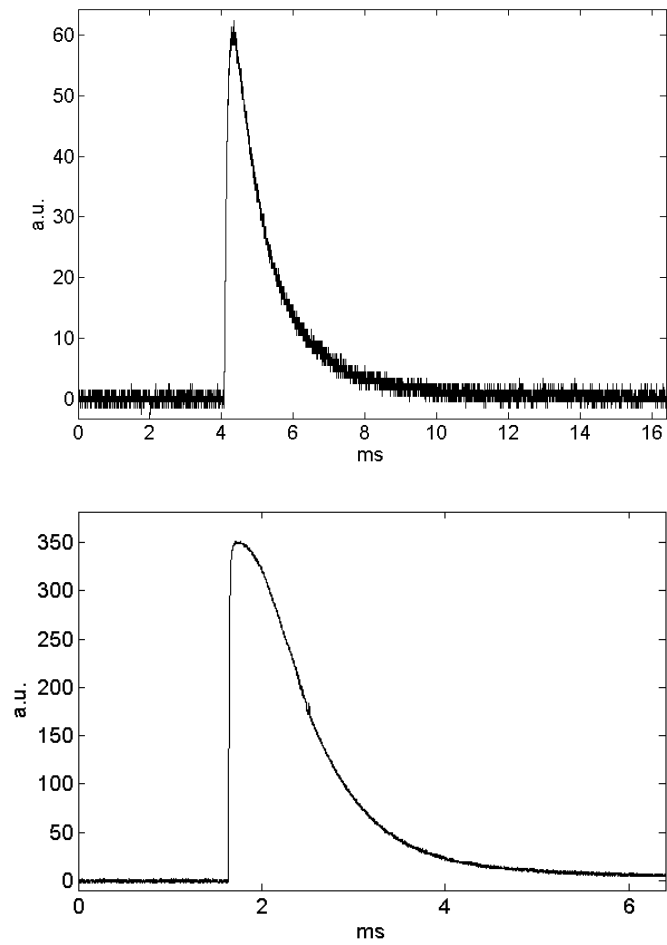


Figure 5.8: Example of pulses of different energy. Top: a low-energy pulse (~ 50 keV). Bottom: a high-energy (~ 520 keV), saturated pulse. Non-linear effects become important at ~ 150 a.u.

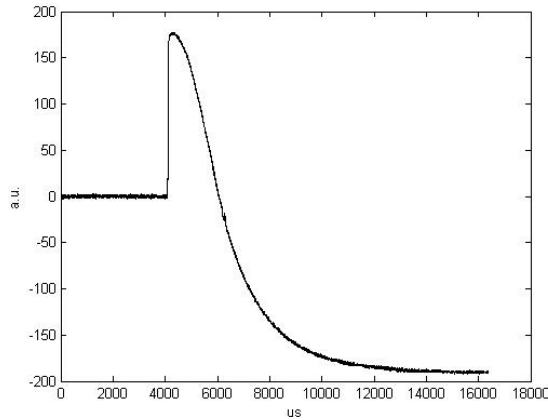


Figure 5.9: Example of a pulse with a loss of three flux quanta. If no flux quanta were lost, the baseline on the right side should be at the same height as on the left side. From the difference between the left and the right baseline it is possible to establish how many flux quanta were lost.

is not affected.

5.2.1.2 Electron Recoils

The phonon signal gives the information on the energy of the interaction. It is then necessary to calibrate the phonon channel in energy. This is achieved by starting from the electron recoil band.

The height of the raw pulses is proportional to the energy of the interaction only up to the amplitude where non-linearity effects appear. As will be shown later, for the measurements discussed here, non-linearity effects in the phonon channel appear already at 100-150 keV. One possible method to extract the information on the energy of the interaction also in the case of big pulses, is to perform a template fit.

The basic assumption of this procedure is that the part of the pulse produced in the linear region of the transition always maintains the same shape. Considering only events of the same kind (e.g. electron recoil events) in first approximation this can be assumed.

One can then proceed in the following way: from the low-energy events,

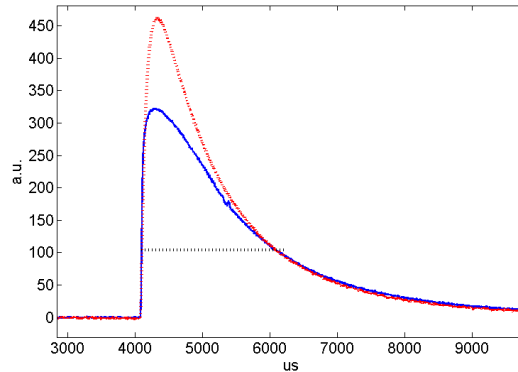


Figure 5.10: Template fit in the case of a saturated pulse. The pulse (blue solid line) is cut at height 100 (black dotted horizontal line), all points above 100 a.u. are ignored in the fitting procedure. The standard pulse (red points) is scaled in order to fit the lower part of the pulse.

for which the film remains in the linear region of the transition, a standard event is created, by summing many pulses (in this way the noise is filtered out and one gets a “clean” standard event). This standard pulse is used to fit all other pulses. The pulses to be fitted are cut at a height where non-linearity effects have not yet appeared, and the standard event is scaled to make it fit this lower part. The height at which the cut is performed is kept the same for all pulses. This means that, in the case of high-energy events, only a small fraction of the pulse is considered for the fit. In Fig.5.10 the fit of a saturated pulse is shown. In this case the cut was set at 100 a.u. All the points higher than 100 a.u. are ignored for the fit. As one can see, the scaled standard pulse reproduces the lower part of the pulse well. this way, the height of the scaled standard event contains the information on the energy of the interaction, since the scaled standard event represents the pulse as it would be in the case of an ideally infinite and perfectly linear transition.

The assumption that for electron recoil events the pulse shape is independent of the energy is true only in first approximation. In Fig.5.11 standard events produced from different energy regions are compared. The events are scaled so that the height is the same, and the shape can easily be compared.

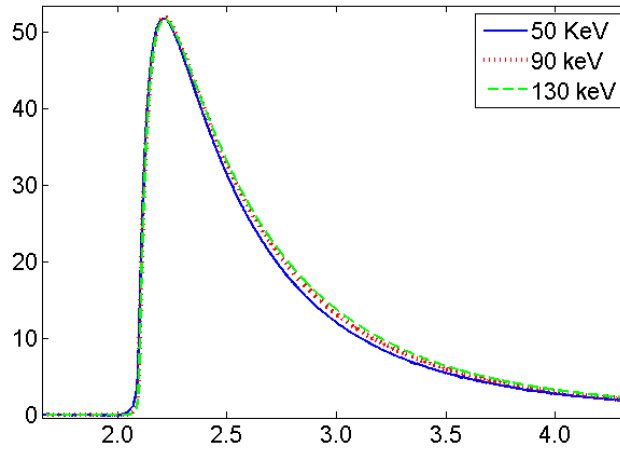


Figure 5.11: Pulses from phonon events of different energies. Each of the plotted pulses is the average of several pulses of the same energy. The pulses are scaled to the same height. The pulse shape changes regularly with the energy.

One can see that the decay-time constant increases slightly but regularly with the energy. In this situation, the template fit procedure is not exact. In particular, the choice of the energy region from which the standard event is produced, and the height at which the pulses are cut, can influence the height of the fitted pulse. On the other hand, given a certain standard pulse and a certain height for the cut, the height of the fitted pulse will be the same for all events corresponding to the same interaction energy: the fitted amplitude has a one to one relation to the energy of the interaction.

In order to find the relation between the fitted amplitude and the energy, one needs to have events in the electron recoil band, for which the energy is known. This is achieved by irradiating the detector with γ quanta of known energies. The sources that have been used are ^{57}Co (line at 122.1 keV), ^{133}Ba (lines at 276.4 keV, 302.9 keV, 356.0 keV, 383.8 keV) and ^{137}Cs (line at 661.7 keV). The ^{133}Ba and the ^{137}Cs sources were present during all measurements to monitor the stability of the working point. The ^{57}Co source was present only during dedicated calibration measurements (regularly 2 times a

day).

In Fig.5.12 (top) a typical calibration spectrum of the phonon channel is shown. The peaks produced by the γ lines are fitted with a Gaussian. The resulting positions are fitted to obtain the calibration curve. The curve that best fits the positions is a power law of the form $y = a * x^b$ [47]. In Fig.5.12 (bottom) the calibration fit is shown, with $a = 1.63 \pm 0.06$ and $b = 0.967 \pm 0.006$.

In most cases the working point was stable enough that measurements performed over several days could be fitted with the same standard event and processed together to find a calibration curve. The spectrum of Fig.5.12 contains events from all the calibration measurements carried out during the week in which the measurement with the ^{252}Cf source was performed. The good energy resolution of the γ peaks (FWHM = 9.14 keV for the line at 356 keV) confirms the stability of the measurement.

5.2.1.3 Nuclear Recoils

The procedure described in the previous section is consistent for the electron recoil band, since the calibration events are also electron recoil events. If the shape of the pulses for nuclear and electron recoil events would be the same, the calibration curve found for the electron recoil band could also be applied to the nuclear recoil band.

In Fig.5.13, a pulse from the nuclear recoil band is compared with a pulse of the same height from the electron recoil band. As one can clearly see, the shape of the two pulses is different. A template fit of events from the nuclear recoil band performed with the standard pulse from the electron recoil band would give a result not well defined, and dependent on the height of the cut chosen for the fit. Since no calibration events are available for the nuclear recoil band, there would be no possibility to assign the right energy with such a procedure. Moreover, to determine the phonon quenching, it is necessary to compare the amount of phonon energy of events of different kind. To do this, one needs to compare the amplitude of the recorded pulse, independently of

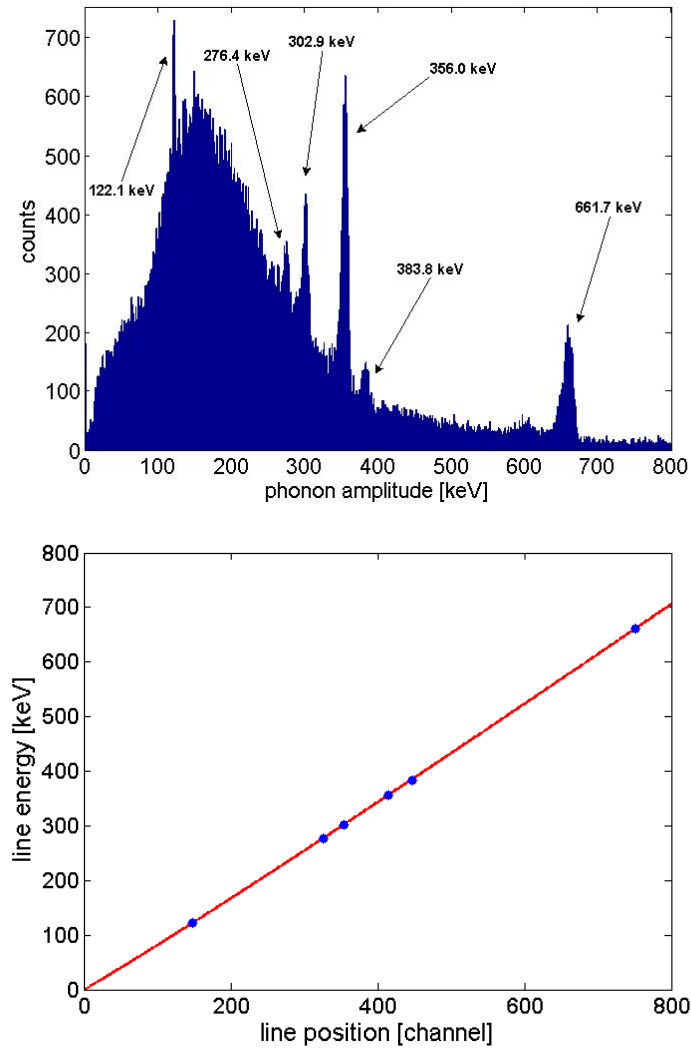


Figure 5.12: On the top a calibration spectrum is shown, measured with the following γ sources: ^{57}Co (line at 122.1 keV), ^{133}Ba (lines at 276.4 keV, 302.9 keV, 356.0 keV, 383.8 keV) and ^{137}Cs (line at 661.7 keV). The continuous background is mainly due to muons. Bottom: calibration points (blue) obtained from the γ lines and the best fit (red line).

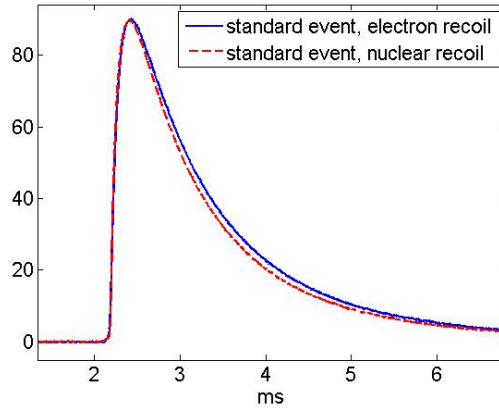


Figure 5.13: Comparison between a standard event from the electron recoil band (blue, solid line) and one from the nuclear recoil band (red, dashed line). The two standard events are made from pulses of roughly the same height.

its shape.

As long as the TES remains in the linear region of the transition, differences in the pulse shape are only due to differences in the mechanism of phonon production. In this case, independently of the shape of the pulse, its integral is proportional to the energy absorbed by the sensor. When saturation and non-linearity effects arise, the proportionality is not respected any more.

In Fig.5.14 the ratio between the integral and the fitted amplitude is plotted versus the fitted amplitude for events from a measurement with ^{133}Ba and ^{137}Cs γ sources. The values of the integral are scaled at 50 keV. The gray scale indicates the density of events, darker area corresponding to higher density. The ratio is equal to 1 if the integral is proportional to the energy. From the plot it is clear that this is the case up to ~ 100 keV. Above this energy, the ratio is smaller than one, meaning that the integral of the pulse would give too low an energy.

However, as long as the effects of saturation and non-linearity of the transition are not too strong, a one to one relationship between the integral and the energy could be maintained. By means of the calibration, the right energy has been assigned to each electron recoil event. This can be used to find the

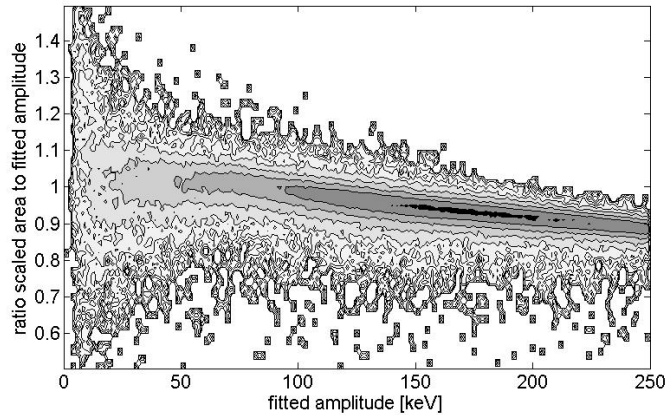


Figure 5.14: Plot of the ratio between the scaled integral (scaled at 50 keV) and the energy from the template fit, versus the energy of the template fit. Darker area indicates a higher density of events. The ratio is one as long as the area is proportional to the energy absorbed by the TES. This is the case up to ~ 100 keV. At higher energies the integral method gives smaller values than the template fit.

relation between the integral and the energy for the electron recoil band. If it is confirmed that, for the energy range of interest, this relation is unique, it can also be applied to the nuclear recoil band.

In Fig.5.15 the histogram of the integral of the pulses is shown, for a measurement with ^{133}Ba and ^{137}Cs γ sources. In the histogram only events from the electron recoil band are plotted. For comparison, the histogram is superimposed to that obtained with the calibrated fitted amplitudes. The fact that the two histograms are nearly identical, confirms that the method of calibrating the integral is reliable and does not produce a loss in resolution.

5.2.2 Light Channel

5.2.2.1 Calibration of the Light Detector

As explained in section 4.2.4, the scintillation light is collected by a silicon substrate that converts the photons into phonons. The phonons are then absorbed by a TES of the same kind as the one used for the phonon detector,

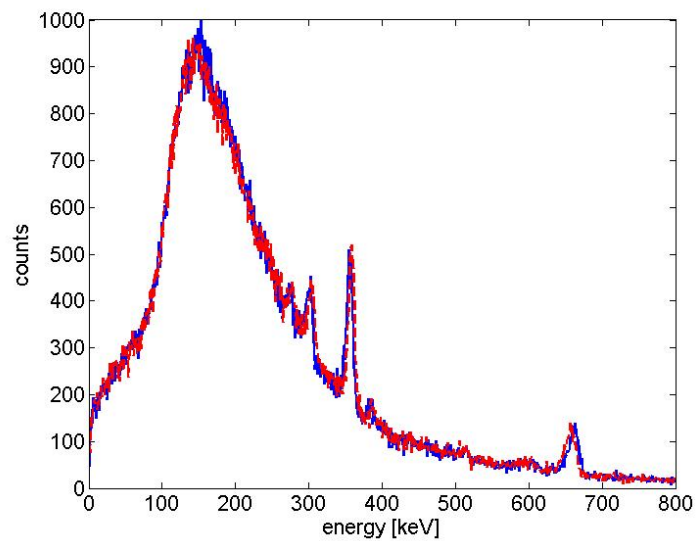


Figure 5.15: Histogram of the phonon signal (electron recoil events), calibrated by means of the integral (red dashed line). The γ lines of ^{137}Cs (661.7 keV) and of ^{133}Ba (276.4 keV, 302.9 keV, 356.0 keV and 383.8 keV) are visible. The histogram is superimposed to that obtained using the standard event fit (blue solid line). The superposition shows that the two histograms are similar (although not identical), in particular it is clear that the energy resolution obtained with the integral method is nearly as good as that reached by fitting the amplitude.

and the mechanism of production of the pulse is similar to that described in section 5.2.1.1.

It cannot be excluded that the light output of the crystal has a non-linear relation to the energy of the interaction. Independently from this, the light detector itself can have a non-linear behavior.

By calibrating with γ sources, the two contributions cannot be separated, so that it is impossible to know if a non-linearity of the light channel is due to a non-linearity of the light detector, or if it is a characteristic of the crystal. In order to separate the two contributions, it is necessary to find an alternative method for the calibration of the light detector, without involving the scintillation light. As described in section 4.2.5, a radioactive ^{55}Fe source is mounted below the detector holder, on the side of the light detector. The ^{55}Fe nuclides decay by electron capture into ^{55}Mn . The excited ^{55}Mn atoms de-excite by the emission of the characteristic K_α (5.899 keV) and K_β (6.490 keV) X-rays. Between the ^{55}Fe source and the detector, a thin (0.015 mm thick) aluminum foil is placed. Most of the quanta from the source pass through the foil without interacting. The ones that interact, excite aluminum atoms that decay by emission of a 1.49 keV X-ray quantum. The X-rays from the Mn and from the Al, hitting the silicon substrate of the detector, lose their complete energy in it. This energy is converted into phonons and finally produces a pulse in the TES. This process affects only the light detector, which can then be calibrated independently of the scintillation properties of the CaWO_4 crystal. Since the energy of the quanta is known, the light detector can be calibrated using these three points.

In some cases, the X-rays emitted by the silicon atoms (excited after the interaction of a photon from the source) escape the detector. In this case the energy detected is that of the original quantum from Mn minus the characteristic X-ray of the excited silicon atom. These X-rays have an energy of 1.74 keV, so that two secondary peaks arise (4.16 keV, from the K_α quanta and 4.75 keV from the K_β quanta of ^{55}Mn).

In Fig.5.16 the spectrum of the events from an ^{55}Fe source is depicted. The

events shown are collected during one week, simultaneously with the neutron events (not shown). The Fe events, in fact, can be distinguished from the γ and neutron events, since no phonon events are associated with them. The peaks of the K_α and K_β lines of ^{55}Mn are the most intense. The line from aluminum is very weak, since only a small fraction of the X-rays interacts in the thin aluminum foil. Still, due to the high statistics, the line can be resolved (see Fig.5.16, bottom) and the position determined. In addition, the two Si escape peaks are clearly visible.

To obtain the spectrum of Fig.5.16 the procedure of the template fit, described in section 5.2.1.2 was applied. In this case, in comparison to the phonon channel, the non-linearity effect appears at a much higher energy. However, the pulses produced by events of the K_α and K_β lines of Mn show a slightly saturated shape (see Fig.5.17). For the template fit, a standard pulse was made from events of the aluminum peak.

The position of the peaks is determined by Gaussian fits. The K_α and K_β peaks of Mn are fitted together with a double Gaussian. In Fig.5.18, top, the plot of the positions of the X-ray peaks of Fig.5.16 versus the energies of the lines is shown together with the linear fit. On the bottom of Fig.5.18 the difference between the energy of the X-ray lines and the fit is shown. The maximum deviation is about 0.5% and the points are distributed randomly around zero, which proves that the linear function well fits the calibration points.

The same calibration procedure has been applied for the measurements performed during February-March 2008. Also in this case, the linearity of the light detector is confirmed.

5.2.2.2 Electron Recoils

Now that the linearity of the light detector has been proved, one can proceed to the treatment of the light signals produced by interactions in the CaWO_4 crystal. Also in this case, the procedures used for the electron recoil band and the nuclear recoil band are described separately.

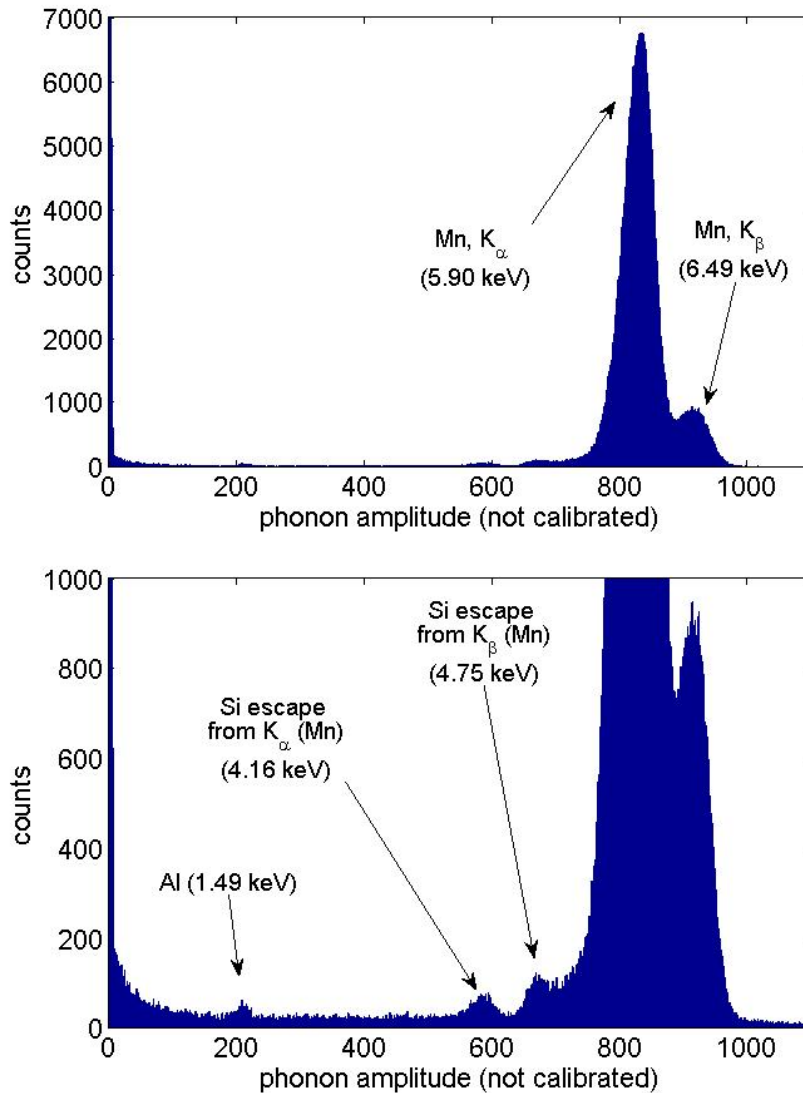


Figure 5.16: Energy spectrum of the events from an ^{55}Fe source. Top: the complete spectrum is shown. The two intense peaks at the right end of the spectrum are the K_{α} and K_{β} lines of ^{55}Mn . The amplitude is obtained with the template-fit procedure described in section 5.2.1.2. The standard pulse used for the template fit was made by summing pulses from events in the aluminum peak (blue dashed line in Fig.5.17). In the bottom picture, the vertical scale of the spectrum is enlarged. Here the silicon escape peaks and the aluminum peak are visible.

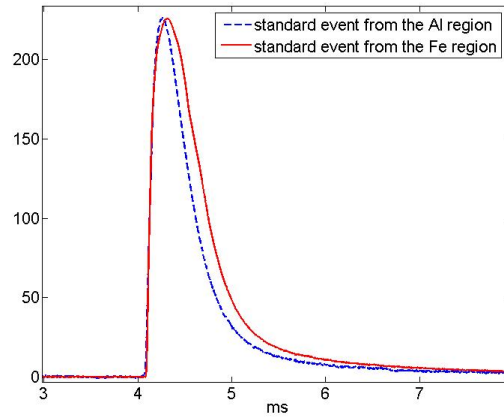


Figure 5.17: Comparison between two standard pulses from the ^{55}Fe events. The blue (dashed) line is obtained summing pulses from the aluminum peak, for the red (solid) line, pulses from the K_α peak of ^{55}Mn are used. The red (solid) pulse is scaled to the height of the blue (dashed) one. Clearly, the red (solid) pulse is partially saturated, so that it cannot be used for the template fit.

The working point of the light detector in both sets of measurements (February-March and April) has the characteristics that non-linearity and saturation effects appear at a much higher energy than in the case of the phonon channel. Light pulses corresponding to electron recoil events of 300-400 keV still have the expected shape.

For this reason, the integral of the pulses is a good parameter to determine the energy of the light signals. On the other hand, for the (usually small) light pulses the noise is much more important than in the case of the phonon pulses. This causes a loss in resolution for small pulses. In the measurements discussed here, the influence of the noise becomes significant for light pulses from electron recoils with an energy lower than ~ 200 keV. The only way to reduce the impact of the noise is the standard event fit. In this case a standard event has been produced from events of energy ~ 100 keV, and the fit has been applied to events up to 300 keV. To verify that the standard event fit is a reliable method in the energy range considered, one can look at the plot shown in Fig.5.19. Here the ratio between the integral of the pulses and

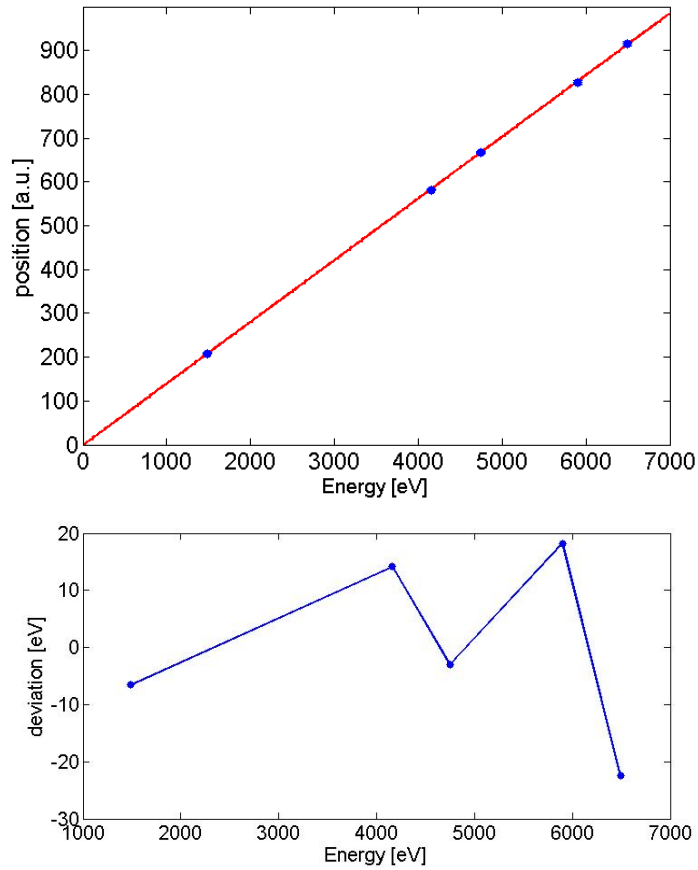


Figure 5.18: Top: Plot of the calibration points (position versus energy) obtained from the ^{55}Fe spectrum of Fig.5.16, together with a linear fit. Bottom: Difference between the energy of the lines and the calibration fit. The deviations are less than 0.5% and random. This confirms that the linear fit well reproduces the calibration points.

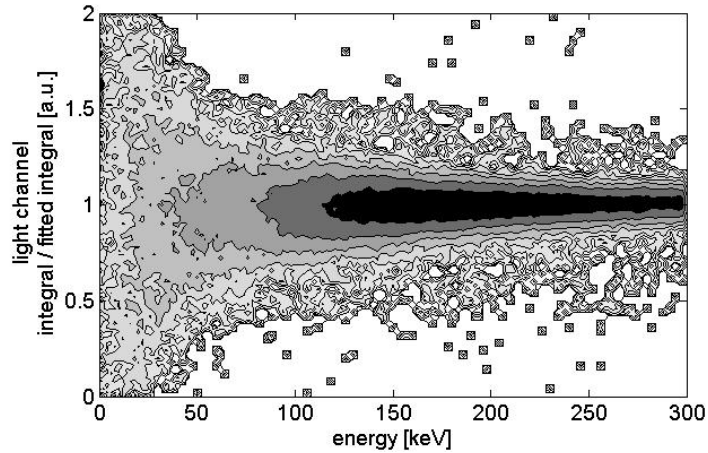


Figure 5.19: Plot of the ratio of the integral of the raw light pulses and the integral of the fitted pulses versus the energy of the interaction, for electron recoil events. The fact that the ratio is equal to one in the complete range, allows us to rely on the standard event fit in this energy range.

the integral of the fitted pulses is plotted versus the energy of the interaction. The ratio is equal to one in the complete range. This proves the reliability, in this energy range, of the standard event fit performed. Up to 200 keV it is necessary to take the integral of the fitted pulses, for higher energies, where the noise does not influence the pulses too deeply, the integral of the raw pulses has been taken.

To convert the scale of the light signal from arbitrary units to a physical unit, we use the light yield (Y). This quantity has already been introduced in section 4.2.1 and is defined as the ratio between the light-signal amplitude and the phonon-signal amplitude. Y is normalized to 1 for electron recoil events in the energy range 100-120 keV. In this way the unit of the light channel is keV_{ee} . Non-linearity effects of the light output of the crystal will result in values of Y different from 1 for energies different from 100-120 keV.

5.2.2.3 Nuclear Recoils

Due to the light quenching, light signals from nuclear recoil events in the CaWO_4 crystal are reduced by a factor of $\sim 1/10$ for oxygen recoil events

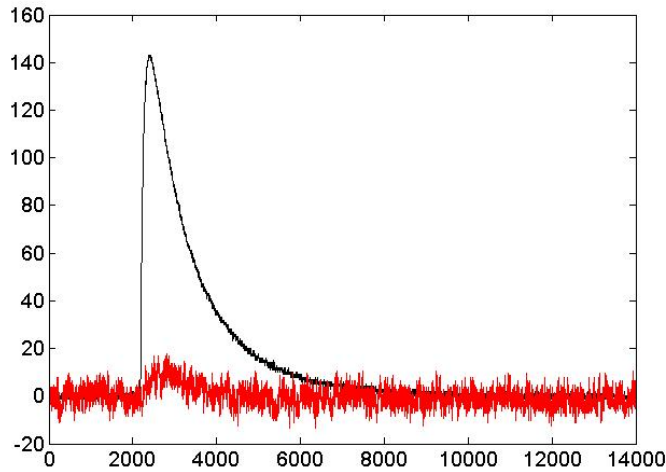


Figure 5.20: Light (red, noisy) and phonon (black) pulses for a nuclear recoil event of 100 keV.

down to $\sim 1/40$ for tungsten recoil events. As a consequence, also for nuclear recoil events of higher energy, the light signals are so small that the integral is strongly influenced by the noise. For this reason, the standard event fit cannot be avoided in this case. The amplitude range of the nuclear recoil pulses, however, is relatively small, so that the pulse shape is not expected to change significantly and the standard event fit can be expected to be reliable.

In Fig.5.20, an example of a nuclear recoil event of 100 keV is shown. The black trace is the pulse in the phonon channel, the red one (much smaller and noisy) is the light pulse. In such a case it is clear that the integral of the trace for the light pulse does not give a reliable information. The method of the template fit helps in this case to extract the pulse from the noise.

In a case like the one of Fig.5.20, however, also the template fit procedure is difficult to apply to the light channel, because the onset of the pulse cannot be determined precisely. Still, the phonon signal corresponding to the same event can be used to help in the fitting procedure. Since the two pulses are produced by the same event, they have the same onset. Instead of performing the fit separately for the phonon and the light channel, a coincident fit is done. From the fit of the phonon pulse (with a much better signal to noise ratio)

the position of the onset is determined, and the fit of the light pulse is forced to this position. For very small light pulses, that are dominated by the noise, this procedure can lead to a negative amplitude.

In Fig.5.21 the plot of the normalized light yield versus the phonon energy for a measurement with the neutron beam and ^{133}Ba and ^{137}Cs γ sources is shown. The upper band is the electron recoil band, the lower band is composed of nuclear recoil events. The events above the electron recoil band are due to random coincidences of events in the crystal and direct hits of the light detector (for example from the ^{55}Fe source). In such a case, the additional light produced by the direct hit of the light detector shifts the event above the electron recoil band. The events between the two bands are due to inelastic scattering on tungsten and will be described in detail in the next section 5.2.2.4.

5.2.2.4 Inelastic Tungsten Recoils

Between the two bands two group of events can be seen. These are due to inelastic scattering of neutrons on tungsten nuclei. In this case the nucleus is excited, and the de-excitation γ interacts in the crystal. The two signals (from the γ and from the recoiling nucleus) cannot be distinguished, and the result is a phonon pulse of an amplitude equal to the sum of the recoil energy plus the γ energy. The γ component of the pulse has a higher light output that shifts the events above the nuclear recoil band. The first excited levels of tungsten are at 46.5 keV and 99.8 keV (^{183}W), 100.1 keV (^{182}W), 111.2 keV (^{184}W) and 122.6 keV (^{186}W). These produce the classes of events that can be seen in this plot. The events at 46.5 keV are isolated, the other events, between ~ 100 keV and ~ 122 keV appear as a single group, since the energies are too close to be separated. The first excited levels of oxygen and calcium are at much higher energies (6.05 MeV and 3.35 MeV, respectively) and produce a continuum of events between the two bands, due to compton scattering of the γ s in the crystal.

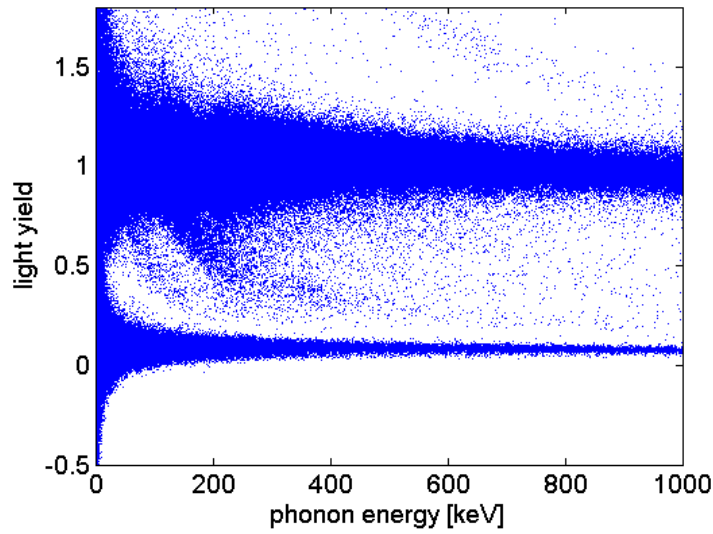


Figure 5.21: Plot of the light yield versus the phonon energy for events from a measurement with the 11 MeV neutron beam and ^{133}Ba and ^{137}Cs γ sources. The upper band is the electron recoil band, the lower is the nuclear recoil band. The events above the electron recoil band are random coincidences of events in the crystal and direct hits of the light detector (for example from the ^{55}Fe source). Direct hits of the light detector only produce a light signal without a phonon signal, so such a coincident event has a higher light signal than a normal electron recoil event. The events present between the two bands are due to inelastic scattering on tungsten. A detailed description of such events is given in section 5.2.2.4.

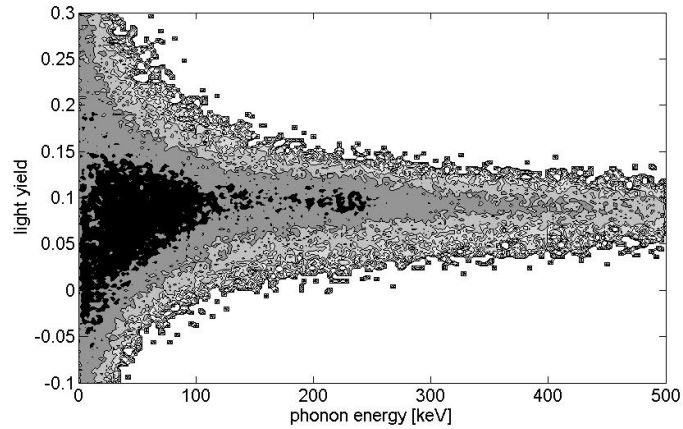


Figure 5.22: Light yield versus phonon energy for nuclear recoil events in a measurement with the 11 MeV neutron beam. The gray scale indicates the density of events, darker regions corresponding to higher densities. The asymmetry of the band (particularly evident below 100 keV) is due to the contributions of the different kinds of nuclear recoils.

5.3 Quenching Factors

5.3.1 Data Evaluation

The quenching factor (QF) defined as $1/Y$ is a parameter useful to characterize the light output of a specific kind of interaction.

Each kind of interaction in the crystal has a different light yield, which produces different bands in a yield-energy plot like in Fig.5.21. The lower band, that has been indicated as the nuclear recoil band, is actually composed of three bands, one for each kind of nuclei present in the crystal (oxygen, calcium and tungsten). These three bands, however, overlap, so that at first sight they appear as one single band. Since the contributions of the three kinds of nuclear recoils are different, however, the band is expected to be asymmetric.

In Fig.5.22 the nuclear recoil band of the plot of Fig.5.21 is shown in greater detail. Darker regions indicate a higher density of events. The distribution is centered at ~ 0.1 . The main contribution is given by oxygen recoils, due to the larger cross section and to the higher number of oxygen atoms in

CaWO₄. At low energies (< 100 keV), the asymmetry of the band is particularly evident: the region with a high density of events extends asymmetrically into the direction of low light yield, because of the contributions of calcium and tungsten. For 11 MeV neutrons, the tungsten contribution is significant up to ~ 200 keV (see section 4.1.3).

5.3.2 Quenching Factors for Oxygen and Calcium

The histogram of Fig.5.23 (bottom) represents the light yield of nuclear recoil events in the energy interval 200-240 keV; the events reported in the histogram are the ones marked in gray in the plot of the top panel of Fig.5.23. Using the results of the calculation of the recoil spectra described in section 4.1.2, the number of calcium events in this energy interval is expected to be $\sim 15\%$ of the number of oxygen recoils. The contribution of tungsten is expected to be $\sim 3\%$, and is considered negligible.

By fitting the histogram with the sum of two Gaussians (equation 5.4),

$$f(x) = a_1 \cdot e^{\left(\frac{-(x-b_1)}{c_1}\right)^2} + a_2 \cdot e^{\left(\frac{-(x-b_2)}{c_2}\right)^2} \quad (5.4)$$

the two contributions can be separated, obtaining the values of the light yield for oxygen and calcium in this energy interval. The result of this fit (with all 6 parameters free) is also shown in Fig.5.23: the curve that best fits the data is the red (full) line. The blue (dotted) and green (dashed) curves are the two Gaussians that represent the contributions of oxygen and of calcium, respectively. The amplitudes are given by a_1 and a_2 . The positions (b_1 and b_2) of the Gaussians give the values for the light yields ($1/b_1$ and $1/b_2$ are the QFs of oxygen and calcium, respectively). The widths of the Gaussians are characterized by c_1 and c_2 .

For each of the measurements performed (the two measurements with the 11 MeV neutron beam and the measurements with the ²⁵²Cf and ²⁴¹Am-Be neutron sources), several energy intervals have been selected, and the method of the double-Gaussian fit has been applied to the light-yield histograms.

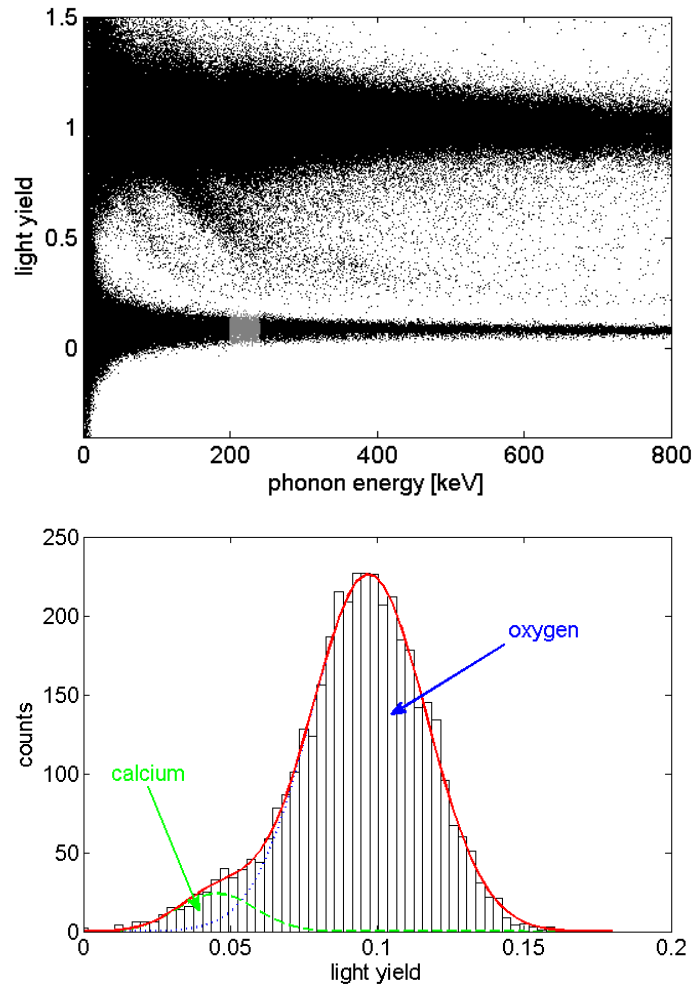


Figure 5.23: Top: plot of the light yield versus the phonon energy for a measurement with the 11 MeV neutron beam. Bottom: histogram of the light yield for nuclear recoil events in the energy interval 200-240 keV (marked by the gray area in the top panel). The histogram is fitted with a curve obtained as the sum of two Gaussians (red, full line). The blue (dotted) and green (dashed) curves are the Gaussians that compose the red (full) curve. They represent the contributions to the spectrum from oxygen recoils (blue, dotted curve) and from calcium recoils (green, dashed curve).

At low energies, the widths of the distributions increase, because of the low photon statistics. Below ~ 100 keV the widths are such that the different contributions cannot be separated any more.

As shown in table 4.1, depending on the source, the contributions of the different recoiling nuclei to the spectrum are different. In the measurements with the ^{252}Cf and $^{241}\text{Am-Be}$ sources the contribution of tungsten is negligible down to ~ 100 keV, which is also the minimum energy at which the different QFs can be evaluated. In this case, the fit with the sum of two Gaussians has been performed for various energy intervals at energies from 100 keV up to 350 keV for the measurement with the ^{252}Cf source and to 450 keV for the measurement with the $^{241}\text{Am-Be}$ source. The number of events strongly depends on the energy, so that the width of the energy intervals was chosen in such a way to have, in the yield histogram, enough events to perform a reliable fit. Intervals of 20 keV were chosen at low energies. At higher energies, where the statistic decreases, intervals of 40-60 keV had to be taken. In the case of the ^{252}Cf measurements, above 350 keV the statistic was so low that the fit could not be performed any more.

In Fig.5.24, the values of the QFs of oxygen and calcium obtained by fitting the yield histogram with the sum of two Gaussians are plotted as a function of the energy. The errors on the QFs are the statistical errors from the fit and do not take into account possible systematic errors. In the case of calcium, the values of the QFs from different measurements are consistent, but for oxygen, this is not the case: The QFs of oxygen determined from the ^{252}Cf and from the $^{241}\text{Am-Be}$ data are in good agreement. The values obtained from the neutron beam measurements, on the other hand, are systematically higher by 5-10%.

From the distribution of the QFs, some hypotheses on the origin of systematic errors can be made. The measurements with the ^{252}Cf and $^{241}\text{Am-Be}$ sources (denoted as Cf 0308 and AmBe 0308) and the first measurement with the 11 MeV neutron beam (the one of February, denoted as beam 0208) have been performed within a time range of three weeks, without changing the

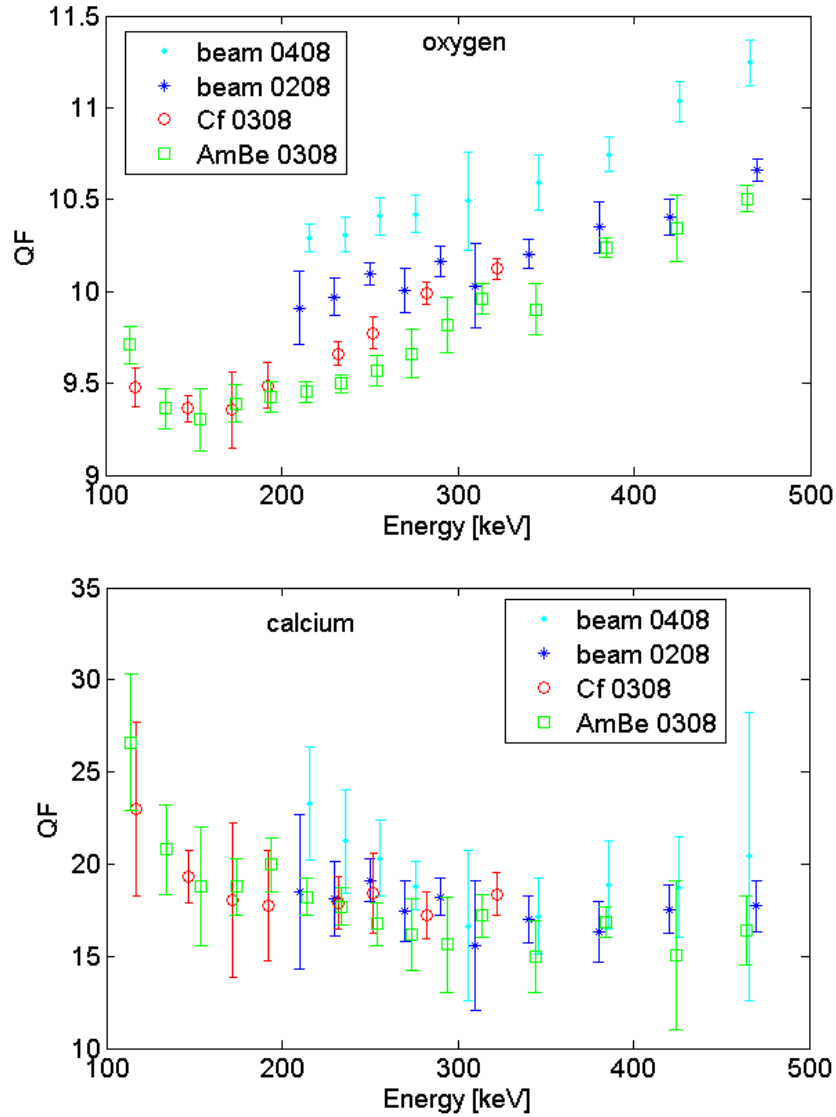


Figure 5.24: QF of oxygen (top panel) and calcium (bottom panel). The values shown here are obtained by fitting the yield histogram with the sum of two Gaussians for events from several energy intervals. The energy intervals have different widths, due to the different intensities of the recoil spectrum at different energies (see text). The error bars of the QFs only include the statistical error from the fit.

working points (temperature and bias current) of the phonon and light detectors. Before the second beam measurement (beam 0408, about one month after the end of the first set of measurements) the cryostat was warmed up, so that the working point had to be set again. The systematic discrepancy of the results amounts to $\sim 5\%$. It is not yet clarified if the different working points were the main cause of this discrepancy.

Another contribution to the discrepancy between the values of the QFs obtained in the different measurements, could arise from the dependence of the signal amplitude from the position in the CaWO_4 crystal where the interaction takes place. An indication for this effect is the observation that the QF from the measurements with beam are always higher than those from the measurements with standard sources. In Fig.5.25, a schematic of the relative positions of the detector and the beam, and of the detector and the neutron sources is shown. The beam irradiates the detector from the front side, and the target cell is at a distance of ~ 15 cm from the detector. The detector is 20 mm in diameter, which means that the neutron flux changes by $\sim 25\%$ from the entrance to the back side of the detector crystal, just by the different solid angle. Thus, in a measurement with the neutron beam, the probability of interaction is not uniformly distributed in the detector, but it is higher on the side facing the target cell.

The standard neutron sources were placed at a lower position, at a distance of ~ 20 cm and irradiate the detector from the bottom. In this case, the detector is exposed to a more uniform neutron flux, and the probability of interaction is almost the same over the complete volume.

Also the light collection can be affected by the position of the interaction, i.e., an interaction further away from the central part of the detector could produce smaller light pulses. If the interaction probability is not uniformly distributed (as in the case with the beam measurements) this can result in a lower average amplitude of the light pulses. Smaller light pulses mean higher QFs, as observed in the measurement with the 11 MeV neutron beam. In order to investigate this phenomenon in greater detail, Monte Carlo simulations

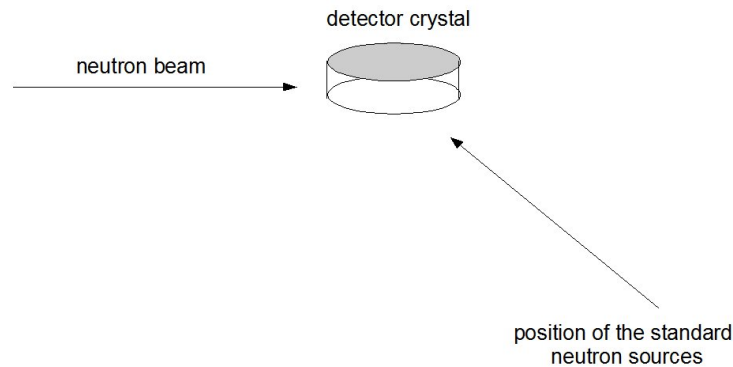


Figure 5.25: Schematic of the relative positions of the detector and the different neutron sources used for the measurements. The neutron beam irradiates the detector crystal from the side, while the $^{241}\text{Am-Be}$ and ^{252}Cf sources were placed at a lower position, so that they irradiate the crystal from the bottom.

have to be performed.

An energy dependence is also observable in the values of the QFs for oxygen. However, since this dependence is a $\sim 10\%$ effect, it cannot be excluded that it has a similar origin as the systematic discrepancies between the different measurements, that are of the same order. It is possible that this dependence is an artifact originating from the calibration. For the calibration of the phonon channel it has been assumed that events with the same energy have the same integral, independently of the kind of interaction (electron or nuclear recoil). This assumption, in the case of different pulse shapes, is only exact if the complete pulse is recorded and if no saturation effects are present. In our case, these two conditions are not fulfilled, but their effect was considered to be negligible because of the little difference in the pulse shape (see Fig.5.13). However, at higher energies, the saturation effects are more pronounced and the part of the pulse that is not acquired is more significant, so that the approximation might not be valid any more and lead to the observed effect. In the case of calcium such a dependence is not observed, but this could be due to the fact that the statistical errors in this case are of the same order as a possible energy dependence.

5.3.3 Quenching Factor for Tungsten

In the measurements with the neutron beam, below 200 keV the contribution of the tungsten recoils is high enough to perform a fit with three Gaussians, in order to evaluate also its QF. The contribution of tungsten is relatively low (about 5 - 7% of that of oxygen), and a fit with three Gaussians has 9 free parameters. When leaving all parameters free, it is rather difficult that the fit converges. On the other hand, from the fits at other energies and from the results shown in Fig.5.24, we have information on the parameters of the distributions of the oxygen and calcium events.

In Fig.5.26 the histogram of the yield for events with an energy in the range of 160-180 keV is shown. In this case, it was possible to have the three-Gaussian fit converge by fixing only the widths of the oxygen and calcium distributions. The values of the widths were chosen according to those obtained in the two-Gaussian fits applied in the same energy interval to the ^{252}Cf and $^{241}\text{Am-Be}$ events: the values of c (see equation 5.4) for the curves representing oxygen and calcium were fixed at 0.03 (oxygen) and 0.02 (calcium).

All the other parameters (positions and amplitudes of the oxygen and calcium distributions, and all the parameters of the tungsten distribution) were left free. The curve that best fits the histogram and the three Gaussians of which it is composed are also plotted in Fig.5.26. The values for the QFs obtained from this fit are the following:

$$\text{QF(O)} = 10.0 \pm 0.1, \quad \text{QF(Ca)} = 19.0 \pm 2.5, \quad \text{QF(W)} = 35 \begin{matrix} +19 \\ -9 \end{matrix}$$

The ratios of the areas of the Gaussians obtained from the fit, should be in agreement with the ratios calculated from the stoichiometric composition and the cross sections (see section 4.1.2 and Fig.4.8). The fitted ratios are 100, 12 ± 3 , and 2.7 ± 3.7 whereas the calculated ratios are 100, 15, and 7 for oxygen, calcium and tungsten, respectively. Although the values are still compatible within the error bars, the fitted areas for calcium and tungsten are systematically lower than the calculated ones. This discrepancy could

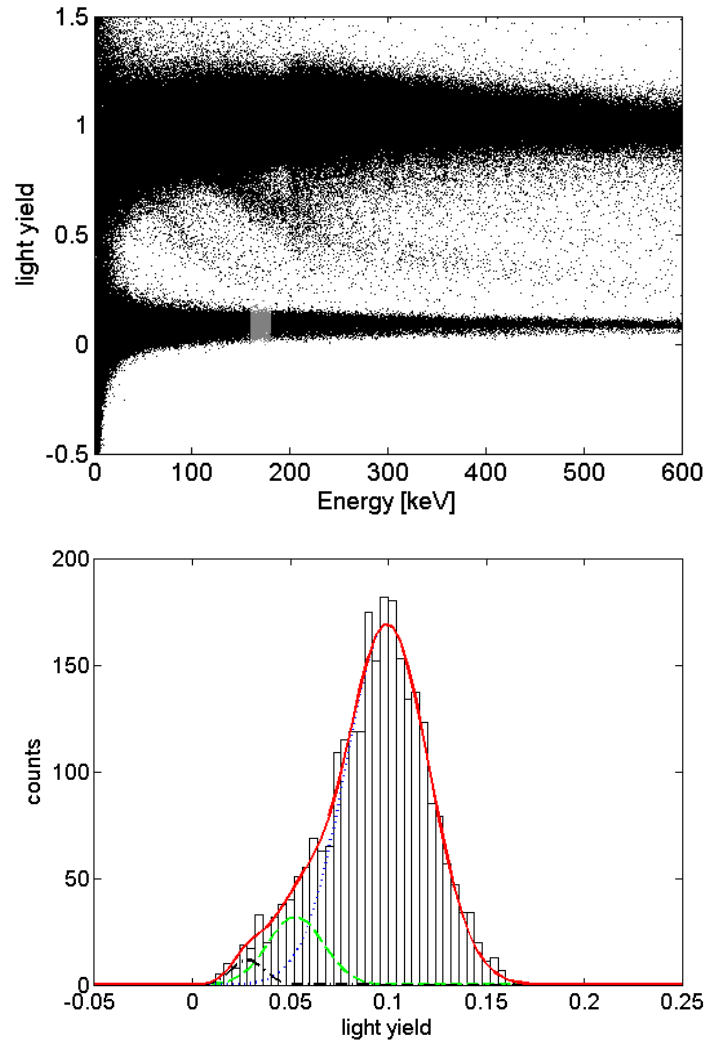


Figure 5.26: Top: light yield vs energy for a measurement performed with the 11 MeV neutron beam. Bottom: histogram of the light yield for nuclear recoil events of energies in the range 160-180 keV (marked in gray in the top panel). The histogram has been fitted with the sum of three Gaussians (red, full line): blue, dotted line for oxygen; green, dashed curve for calcium, and black, dashed-dotted line for tungsten. To perform the fit, two parameters (the widths of the oxygen and of the calcium distributions) have been fixed (see text). The values of the quenching factors obtained from this fit are $QF(O) = 10.0 \pm 0.1$, $QF(Ca) = 19.0 \pm 2.5$ and $QF(W) = 35^{+19}_{-9}$.

partly be due to double scattering in the crystal. According to table 4.2, the probability of multiple scattering in the crystal used for the measurement (20 mm diameter and 5 mm height) is $\sim 7\%$. In most of the cases of double scattering, at least one of the two interactions will be an oxygen recoil. Given the higher light output of oxygen recoils, double scattering events where one of the interactions was a calcium or a tungsten recoil, will be removed from the calcium or the tungsten contributions and will be added to the oxygen contribution. In this way the ratio between the intensities of the three contributions is significantly changed. For a quantitative analysis, Monte Carlo simulations are necessary.

In Fig.5.27 the results for the QFs for oxygen and calcium obtained with the three-Gaussian fit in the energy range 160-180 keV are plotted together with the QF values obtained at higher energies for the same measurement. The agreement is satisfactory within the error bars. This again confirms the reliability of the three-Gaussian fit.

Since the values of the QFs of calcium determined in different measurements and energy intervals are randomly distributed (see Fig.5.24), as QF for calcium the average, weighted with the statistical errors, has been taken. In the case of oxygen, the values are not randomly distributed, but present an energy dependence and systematical discrepancies between different measurements. Since, as explained in section 5.3.2, it is not sure if the observed energy dependence is a property of the crystal or an artifact of the data analysis, for the QF of oxygen a representative value of $\text{QF}(\text{O}) = 10 \pm 1$ has been taken. The error has been estimated to include the systematic discrepancies that are clearly larger than the statistical errors. For the tungsten only the value obtained by the fit of Fig.5.26 is available. To conclude, the values of the QFs obtained with the set of neutron measurements described are those reported in table 5.2.

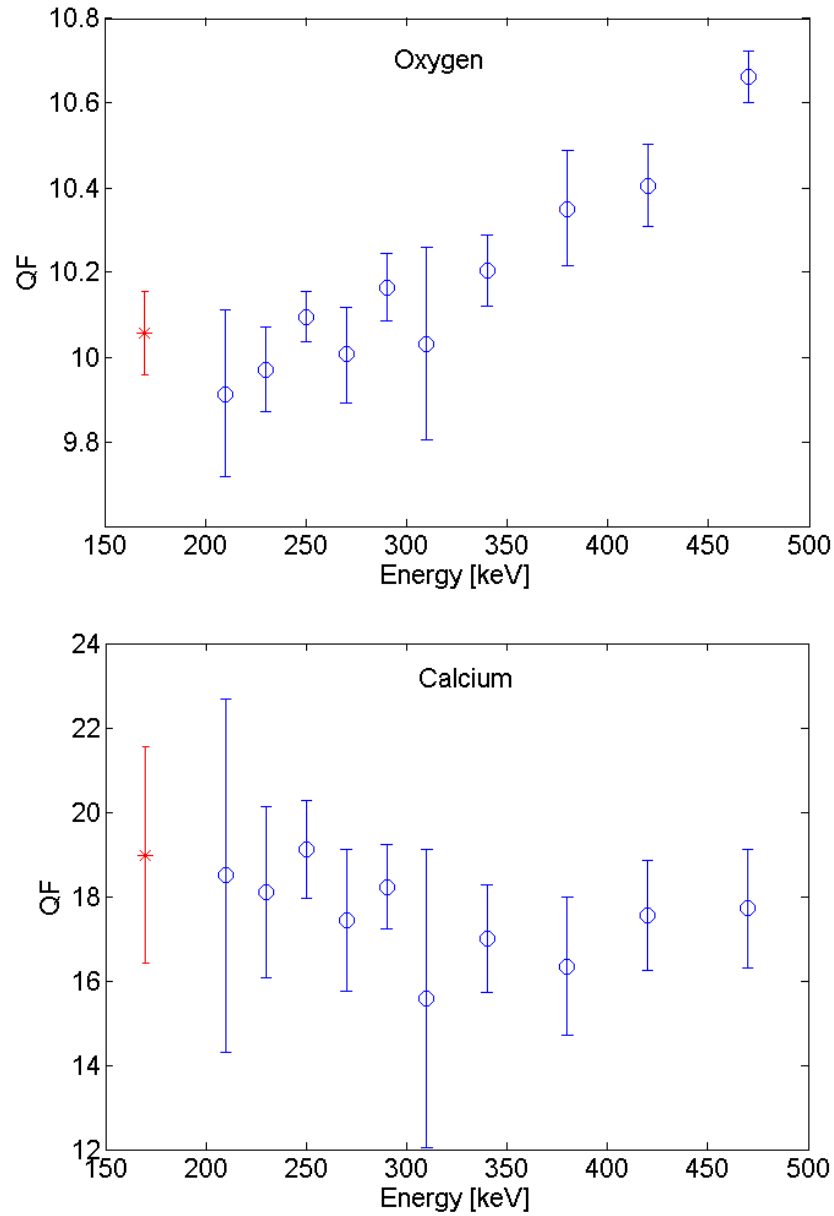


Figure 5.27: QFs of oxygen (top) and calcium (bottom) from the first measurement with the neutron beam (“beam 0208” in Fig.5.24). The blue open circles represent the values which are also shown in Fig.5.24, the red stars are the values of the QFs of oxygen and calcium obtained from the three-Gaussian fit illustrated in Fig.5.26.

nucleus	QF
O	10 ± 1
Ca	17.9 ± 0.2
W	35^{+19}_{-9}

Table 5.2: Values of the QFs of oxygen, calcium and tungsten at ~ 50 mK. The values for oxygen and calcium are average values from four separate measurements and for the energy range 100-500 keV. The QF of tungsten is that determined by the fit shown in Fig.5.26.

5.3.4 Overview of the Quenching-Factor Results

Measurements of the QFs for CaWO_4 have been performed also with other methods, as has already been illustrated in sections 3.2.1 and 3.2.2.

In Fig.5.28, together with the new results (represented by the orange, open circles and denoted as “Neutrons on cryodetector”), those of previous measurements of the QFs are shown [53]. The results denoted as “Ninkovic” and “Huff” are obtained with the method of ion irradiation [63] (a brief description of the measurement technique is given in section 3.2.2). The name “Garching” denotes the values of the QFs for oxygen and calcium obtained with the neutron scattering experiment at room temperature [60] (see section 3.2.1 for a brief description of the measurement). The values marked in red (full) circles for ^4He and Pb have been determined from ^{210}Po decays, during a prototype measurement of CRESST in the Gran Sasso underground laboratory [45].

It is important to notice that the values of the QFs plotted in Fig.5.28, have been measured at different temperatures and with different recoil energies. The values denoted “Garching” are measured at room temperature, with recoil energies between 1-2 MeV for oxygen and 0.5-1 MeV for calcium. The ion irradiation measurements (“Ninkovic” and “Huff”) have been performed at room temperature, with a maximum energy of the ions of 18 keV. In the mass range 25-150 amu, the QFs indicated by “Ninković” are systematically larger than those obtained with the other measurements. It is

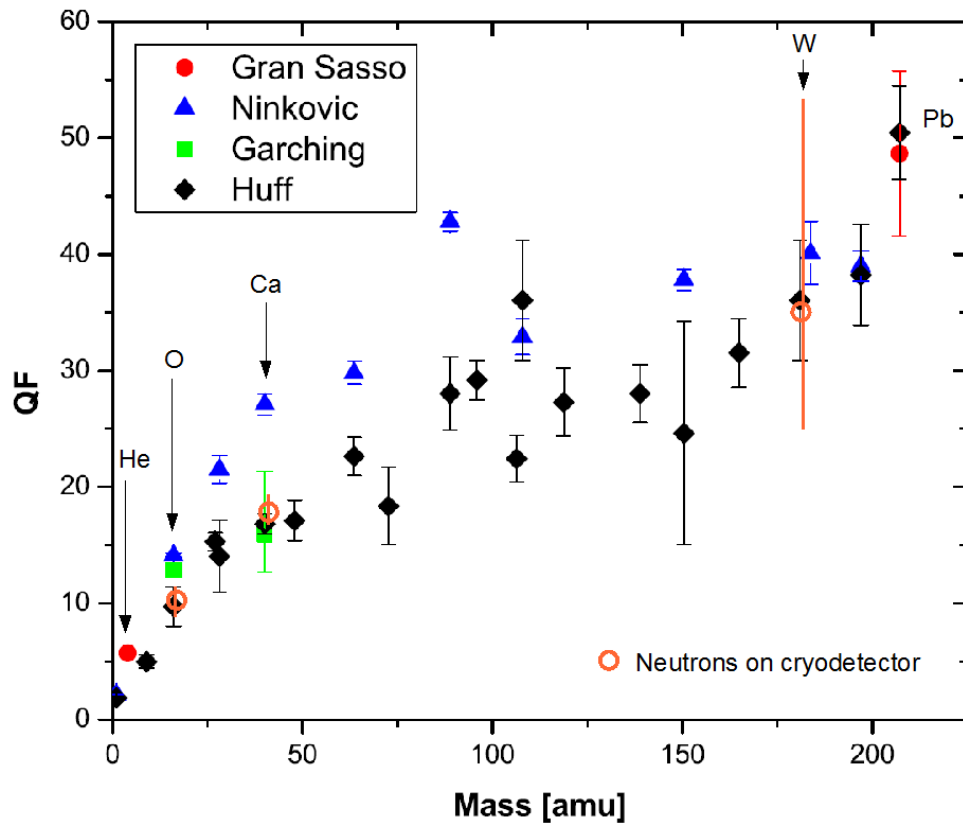


Figure 5.28: Results for the QFs from previous measurements [53], [63], [60], [45] are plotted together with the results presented in the sections 5.3.2 and 5.3.3 (orange, open circles, denoted by “Neutrons on cryodetector”).

expected that the difference comes from a systematic error in the γ calibration [77]. The values of the QFs determined in this work, with neutron induced nuclear recoils, are measured at a temperature of ~ 50 mK in the energy range 100-500 keV. The good agreement of all these values (except for those of the Ninković series mentioned above) indicates that there is rather little dependence of the QFs on the temperature and on the energy. The energy dependence observed for the values of the QFs of oxygen described in section 5.3.2 (see Fig.5.24) is a $\sim 10\%$ effect. This effect is small compared with the errors on the measurements presented in Fig.5.28.

In [78] and [79], preliminary results of a measurement performed with the setup described in section 4.2 are reported. The preliminary values of the QFs found in this first measurement are the following:

$$\text{QF(O)} = 8.5 \pm 1, \quad \text{QF(Ca)} = 14.5 \pm 0.2, \quad \text{QF(W)} = 39 \begin{smallmatrix} +18 \\ -10 \end{smallmatrix}$$

During this first measurement some parts of the setup were not yet in the configuration described in section 4.2. In particular, the ^{55}Fe source was not yet mounted, thus it was not possible to calibrate the light detector. For this reason the values of the QFs are not as reliable as the ones presented in the present work.

5.4 Phonon Quenching

For the data analysis performed up to now, the phonon quenching (defined in section 5.2) has been neglected. In this section it will be shown how it can be estimated.

Applying the calibration obtained for the electron recoil band to the nuclear recoil events, has the consequence that the energy attributed to nuclear recoil events is higher than the real energy of the interaction. This effect has been called phonon quenching. In order to evaluate this difference, at least one group of nuclear recoil events with known energy is necessary. This is normally difficult to achieve, because nuclear recoils produced by neutrons

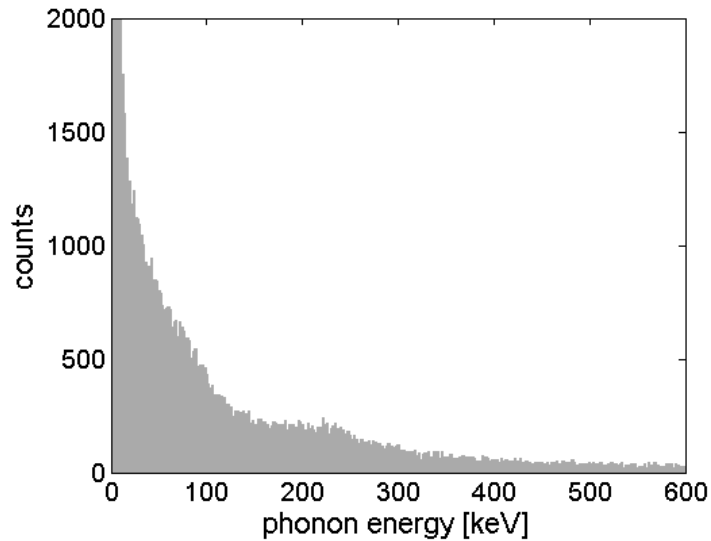


Figure 5.29: Nuclear recoil spectrum for a measurement with the 11 MeV neutron beam. A structure is visible at ~ 240 keV.

always have a continuous spectrum of energies, unless one has the possibility to fix the scattering angle.

In Fig.5.29 the histogram of the nuclear recoil events for a measurement with the neutron beam is shown. The spectrum has a clear structure at ~ 240 keV. This is the structure that has been shown and discussed in section 4.1.2. As explained there, it is due to a nuclear resonance in the cross section of oxygen, so that its energy is defined, independently of the details of the incoming neutron spectrum.

Since this feature is clearly visible in the measured spectrum, it can be used to determine the effect of phonon quenching on the nuclear recoil events. In Fig.5.30 the calculated spectrum (full line) is compared to the measured spectrum of Fig.5.29. Above ~ 60 keV, the calculated spectrum reproduces the measured one quite well, but clearly there is a shift in the position of the structure at ~ 220 keV.

The phonon quenching produces a shift of the nuclear recoil events to higher energies by a factor $1/PQ$ where PQ is defined in section 5.2. The value of PQ can be found by multiplying the calibrated amplitude of the

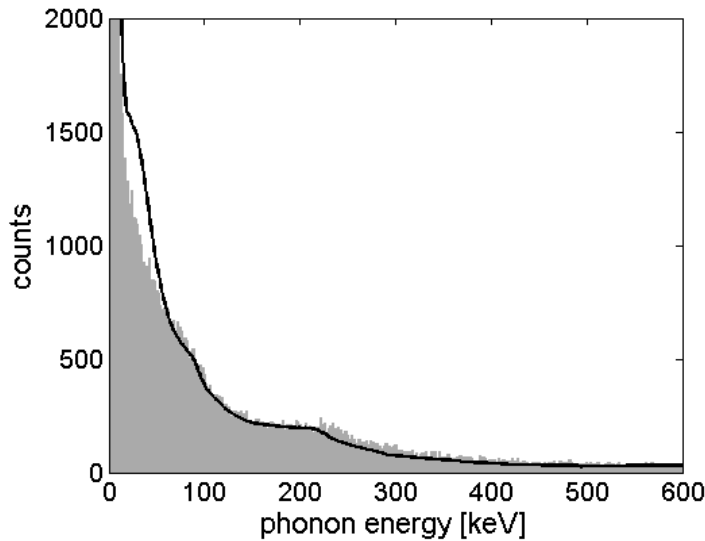


Figure 5.30: Measured recoil spectrum (histogram) and calculated recoil spectrum (full line). The calculated spectrum reproduces well the measured one above 60 keV, but it is slightly shifted, as can clearly be seen when looking at the bump at ~ 220 keV.

nuclear recoil events, by a factor X until they fit the calculated spectrum in the region of the bump. This fit has been performed, by taking the calculated curve in the range 100-400 keV (the low-energy part has been cut out, because in this region the theoretical curve does not reproduce the measured spectrum well enough). The results of the fit, performed for the different measurements, gives a factor $PQ = 0.92 \pm 0.05$. In Fig.5.31, the measured spectrum corrected for the phonon quenching is shown, together with the calculated spectrum. The agreement is very good.

The calculation, the result of which is represented by the full line in Figs. 5.30, 5.31, is based on the assumption of elastic scattering and on the application of equations 3.1 and 3.2. However, it has not yet been clarified if the presence of the resonances in the n - ^{16}O elastic cross section (see Fig.4.3) is responsible for additional mechanisms that influence the recoil energy of the nucleus in a different way than that described by equations 3.1 and 3.2. On the other hand, the generally good agreement between the calculated spectrum

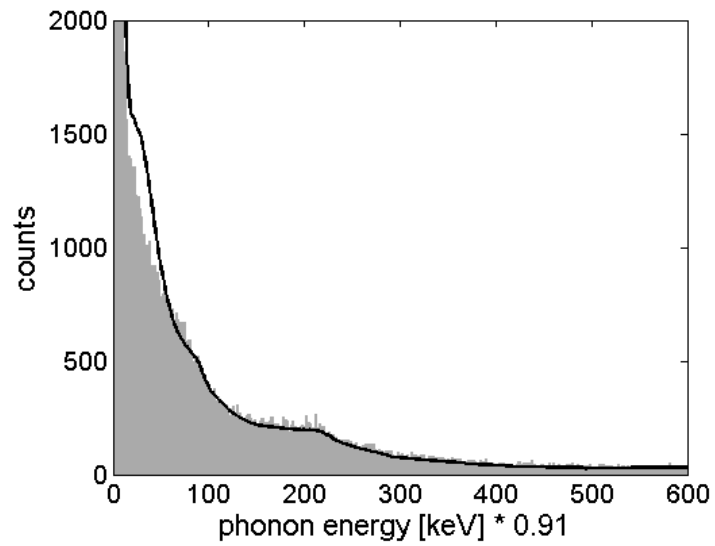


Figure 5.31: Nuclear recoil spectrum corrected for the phonon quenching. The correction has been found by fitting the measured data to the calculated curve. The correction factor in this case results to be $PQ = 0.915$. The agreement between the corrected measured spectrum and the calculated one (black line) is very good.

and the measured one gives us confidence that such additional mechanisms are probably negligible.

The value of PQ indicates that in an electron recoil event, $8 \pm 5\%$ less energy is converted into phonons than in a nuclear recoil event. It is interesting to see if all the phonon energy “missing” in electron recoil events with respect to nuclear recoil events, is converted into light.

The part of the total energy converted into light in an electron recoil event can be evaluated by investigating the light yield of electron recoil events of known energy (e.g. events from γ sources).

In Fig.5.32 the light yield of electron recoil events in the energy range 200-500 keV is shown. The ^{137}Ba line at 356.0 keV is visible as vertical structure in the plot (also other structures are visible, corresponding to the weaker lines at 276.4 keV, 302.9 keV and 383.8 keV). One can notice that the lines are not exactly vertical, but are slightly tilted. This is due to the fact that the distribution of the energy between light and phonons is not the same for all the events: events with a higher light yield will necessarily have a lower phonon energy and vice versa since the total energy is the same. By evaluating the tilt of the structure and extrapolating to the point of zero light yield, one can determine what part of the energy is converted into light for these events [47].

The line at 356 keV was chosen for the evaluation of the tilt, since it is particularly intense. The energy range 340-375 keV was selected, and the light yield was divided into bins. For each bin of the light yield, the position of the line was determined with a Gaussian fit, and a linear fit of the positions as a function of the light yield was performed. The line that best fits the positions is shown in Fig.5.33. The result for the fraction of energy that is converted into light is $(3.9 \pm 1.6\%)$.

This means that only about half of the “missing” energy in an electron recoil event is converted into light. The remaining half is probably converted into radiation-less transitions in the CaWO_4 crystal. The same tendency was observed in [47].

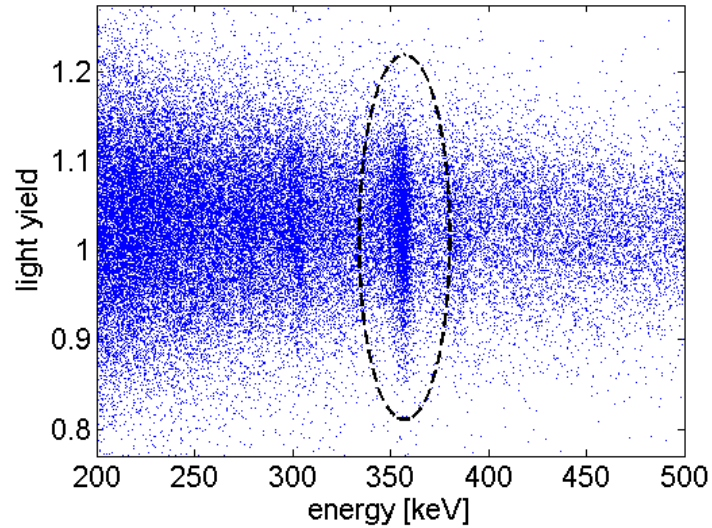


Figure 5.32: Light yield vs total energy for electron-recoil events (200 keV-500 keV) for a measurement with ^{133}Ba . The 356 keV line of ^{133}Ba is marked with the dashed ellipse.

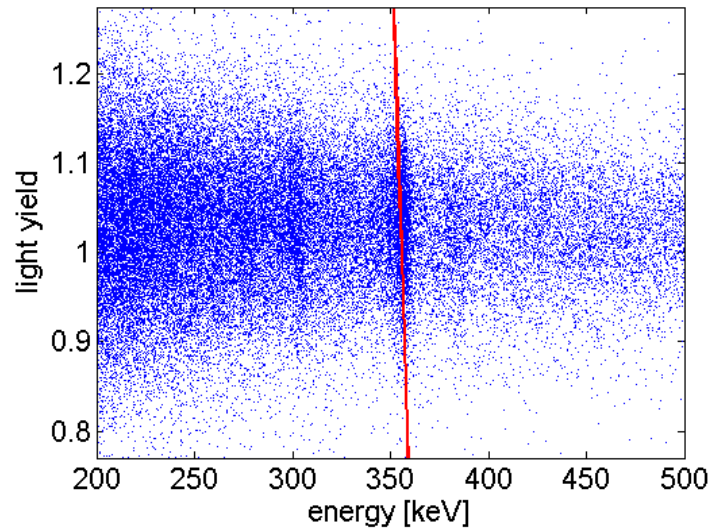


Figure 5.33: Light yield vs total energy for electron-recoil events (200 keV-500 keV) for a measurement with ^{133}Ba . The red, full line is the result of a fit of the position of the 356.0 keV ^{133}Ba line at different light yields. The line is tilted, because of the different distribution of the energy between the light and the phonon signal.

Due to the presence of the iron source, it is also possible to determine the fraction of the total energy of an interaction that is actually collected by the light detector. The ^{55}Fe source allows an absolute calibration of the light detector, since the complete energy of the quanta is detected. If the pulses are small enough and no saturation takes place, the integral of the pulse is proportional to the energy detected. This is the case for the pulses produced by the Al X-rays, that have an energy of 1.49 keV. By comparing the integral of such pulses with the integral of light pulses produced by an interaction in the crystal, it is possible to determine the absolute energy detected by the light detector. We find that an interaction with an energy of ~ 150 keV in the crystal is needed to have a light pulse of the same intensity (integral) as produced by the 1.49 keV Al X-rays. Thus, the fraction of energy detected as light is only $\sim 1\%$ of the total energy of the interaction.

Comparing this result (also investigated in [47] and [73]) with the derived fraction of energy that is converted into light ($3.9 \pm 1.6\%$) indicates that a non-negligible fraction of the light produced ($> 50\%$) is lost, leading to a loss in resolution for the light signals. Such a loss should be avoided since the resolution is crucial for the discrimination of the different nuclear recoils in the detector, and as a consequence for the discrimination of the neutron background in CRESST.

Chapter 6

Summary and Outlook

The study of the response of cryogenic detectors to the different kinds of interactions is crucial for the interpretation of the results of a rare-event experiment like CRESST.

In the CRESST experiment, CaWO_4 single crystals are used as target for the direct detection of dark matter particles. The energy of an interaction is determined by the measurement of the phonon signal. The simultaneous measurement of the light signal allows the discrimination of electron recoil events for interaction energies above ~ 10 keV on the basis of the quenching factor (QF). The QF is a parameter that accounts for the light yield of an interaction.

It has been found that also nuclear recoils have different QFs depending on the mass of the recoiling nuclei. The possibility to distinguish the different nuclear recoils is crucial for the discrimination of the neutron background. At the Maier-Leibnitz-Laboratorium (MLL) in Garching a setup for the investigation of the response of cryodetectors to neutron-induced nuclear recoils has been installed. The measurements presented in this work are aimed at a determination of the QF of oxygen, calcium and tungsten in CaWO_4 single crystals at mK temperatures.

Nuclear recoils in the bulk of the CaWO_4 target have been induced with neutrons. Measurements with a monoenergetic 11 MeV neutron beam pro-

duced at the tandem accelerator of the MLL have been performed, as well as measurements with standard neutron sources (^{252}Cf and $^{241}\text{Am-Be}$). The QFs of oxygen and calcium have been determined for several energy intervals in the range from 100 keV to 500 keV. The mean values found are the following:

- $\text{QF}(\text{O}) = 10 \pm 1$
- $\text{QF}(\text{Ca}) = 17.9 \pm 0.2$

A value of the QF of tungsten has been determined in the energy interval 160-180 keV:

- $\text{QF}(\text{W}) = 35 \begin{smallmatrix} +19 \\ -9 \end{smallmatrix}$

The measurements presented in this work provide, for the first time, values of the bulk nuclear QFs for CaWO_4 at mK temperatures, i.e., the operating temperature of the detectors.

From the study of the nuclear recoil spectrum and of the light yield of electron recoil events of known energy, the distribution of the energy between the phonon and the light signal has been determined. In particular, the phonon quenching (ratio between the phonon energy of an electron recoil event and the phonon energy of a nuclear recoil event with the same recoil energy) has been found to be 0.92 ± 0.05 .

The nuclear recoils produced by neutrons present a continuous spectrum, also in the case of monoenergetic neutrons, that makes the separation of the different recoiling nuclei difficult. The relatively big error of the value of the QF of tungsten is a direct consequence of this difficulty to separate the rather small tungsten contribution from the large contributions of oxygen and calcium.

For a complete separation of the different kinds of events, additionally to the use of a monoenergetic neutron beam, the scattering angle has to be fixed. For this purpose the setup at the MLL is implemented with a system of 40 neutron detectors. By means of a coincidence measurement between the signal of the accelerator (production of the neutrons), the signal in the

cryodetector and the signal from the hit neutron detector, it will be possible in the future to fix the scattering angle, to identify the recoiling nucleus, and to determine the recoil energy via the time-of-flight method. The new coincidence electronics is presently being installed and will be described in [76].

The neutron scattering setup in its complete configuration will represent an internationally unique facility for the investigation of the properties of nuclear recoils in different materials. This will be particularly interesting for EURECA [37], a projected direct-search dark matter experiment with a total target mass of ~ 1 ton. EURECA will also use cryodetectors and, in particular, will provide the possibility to use a variety of different target materials.

Bibliography

- [1] F. Zwicky, *Astroph. J.* **86**, 217 (1937).
- [2] S. W. Allen, P. R. W. Schmidt, and A. C. Fabian, *Mon. Not. R. Astron. Soc.* **334**, L11 (2002).
- [3] C. S. Kochanek *et al.*, *Astroph. J.* **585**, 161 (2003).
- [4] A. Vikhlinin *et al.*, *Astroph. J.* **640**, 691 (2006).
- [5] E. Corbelli and P. Salucci, *Mon. Not. R. Astron. Soc.* **311**, 441 (2000).
- [6] D. Clowe *et al.*, *Astroph. J. Lett.* **648**, L109 (2006).
- [7] C. L. Bennett *et al.*, *Astroph. J. Suppl. S.* **148**, 1 (2003).
- [8] D. N. Spergel *et al.*, *Astroph. J. Suppl. S.* **170**, 377 (2007).
- [9] C. Kraus *et al.*, *Eur. Phys. J. C* **40**, 447 (2005).
- [10] K. Zioutas *et al.*, *Phys. Rev. Lett.* **94**, 121301 (2005).
- [11] C. A. S. T. collaboration, *Journal of Cosmology and Astroparticle Physics* **02**, 008 (2009).
- [12] L. J. Rosenberg and K. A. van Bibber, *Phys. Rep.* **325**, 1 (2000).
- [13] R. Trotta, R. R. de Austri, and L. Roszkowski, *New Astron. Rev.* **51**, 316 (2007).
- [14] G. Alner *et al.*, *Astropart. Phys.* **23**, 44 (2005).

- [15] V. Sanglard *et al.*, Phys. Rev. D **71**, 122002 (2005).
- [16] D. S. Akerib *et al.*, Phys. Rev. Lett. **93**, 211301 (2004).
- [17] T. Bretz, D. Dorner, R. Wagner, and P. Sawallisch, Astropart. Phys. **31**, 92 (2009).
- [18] H. Kubo *et al.*, New Astron. Rev. **48**, 339 (2004).
- [19] H. E. S. S. collaboration, AIP Conf. Proc. **745**, 611 (2005).
- [20] S. D. Hunter *et al.*, Astrophys. J. **481**, 205 (1997).
- [21] W. de Boer, New Astron. Rev. **49**, 213 (2005).
- [22] O. Adriani *et al.*, Nature **458**, 607 (2009).
- [23] J. Gascon, *Direct search for WIMP dark matter*, arXiv:astro-ph/0504241.
- [24] S. Cebrián *et al.*, Astropart. Phys. **10**, 361 (1999).
- [25] O. Martineau *et al.*, Nucl. Instr. and Meth. A **530**, 426 (2004).
- [26] S. Marnieros, A. Juillard, L. Bergé, S. Collin, and L. Dumoulin, Nucl. Instr. Meth. A **520**, 185 (2004).
- [27] Z. Ahmed *et al.*, Phys. Rev. Lett. **102**, 011301 (2009).
- [28] G. Angloher *et al.*, Astropart. Phys. **31**, 270 (2009).
- [29] J. Angle *et al.*, Phys. Rev. Lett. **100**, 021303 (2008).
- [30] P. Benetti *et al.*, Astropart. Phys. **28**, 495 (2008).
- [31] V. N. Lebedenko *et al.*, arXiv:0812.1150[astro-ph] .
- [32] R. Bernabei *et al.*, Nuovo Cimento Rivista Serie **26**, 1 (2003).
- [33] R. Bernabei *et al.*, Eur. Phys. J. C **56**, 333 (2008).

- [34] E. A. Baltz and P. Gondolo, Phys. Rev. D **67**, 063503 (2003).
- [35] R. Brunetti *et al.*, New Astron. Rev. **49**, 265 (2005).
- [36] G. Alner *et al.*, Astropart. Phys. **28**, 287 (2007).
- [37] H. Kraus *et al.*, J. Phys. Conf. Ser. **39**, 139 (2006).
- [38] S. Roth *et al.*, J. Phys. Conf. Ser. **136**, 042085 (2008), arXiv:0809.5183[hep-ph].
- [39] S. Roth *et al.*, to appear in the proceedings of Dark Energy and Dark Matter, Lyon, France, 7 - 11 July 2008.
- [40] D. Akerib *et al.*, Nucl. Instr. and Meth. A **559**, 411 (2006).
- [41] R. Schnee *et al.*, arXiv:astro-ph/0502435 .
- [42] A. Rubbia, J. Phys. Conf. Ser. **39**, 129 (2006).
- [43] E. Aprile *et al.*, arXiv:astro-ph/0207670 (2002).
- [44] G. Angloher *et al.*, Astropart. Phys. **18**, 43 (2002).
- [45] G. Angloher *et al.*, Astropart. Phys. **23**, 325 (2005).
- [46] C. Ciemniak *et al.*, to appear in the proceedings of Dark Energy and Dark Matter, Lyon, France, 7 - 11 July 2008.
- [47] W. Westphal, Development and characterization of cryogenic detectors for the cress experiment, 2008, link <http://www.e15.physik.tu-muenchen.de/fileadmin/downloads/thesis/phd/2008-Wolfgang-Westphal.pdf>.
- [48] R. F. Lang *et al.*, Submitted , arXiv:0903.4687.
- [49] W. Westphal *et al.*, J. Low. Temp. Phys. **151**, 824 (2008).
- [50] R. F. Lang *et al.*, Submitted , arXiv:0905.4282.
- [51] S. Henry *et al.*, JINST **2**, P11003 (2007).

- [52] H. Wulandari, *Study On Neutron-Induced Background in the Dark Matter Experiment CRESST*, PhD thesis, TU München, 2003.
- [53] I. Bavykina *et al.*, *Astropart. Phys.* **28**, 489 (2007).
- [54] R. H. Helm, *Phys. Rev.* **104**, 1466 (1956).
- [55] J.-C. Lanfranchi, T. Lachenmaier, W. Potzel, and F. von Feilitzsch, *Nucl. Instr. and Meth. A* **520**, 135 (2004).
- [56] S. Roth *et al.*, arXiv:0810.0423(astro-ph) , *Optical Materials*, in Press.
- [57] M. Kiefer *et al.*, arXiv:0809.4975(astro-ph) , *Optical Materials*, in Press.
- [58] S. Roth *et al.*, *J. Low. Temp. Phys.* **151**, 216 (2008).
- [59] Los Alamos T-2 Nuclear Information Center, <http://t2.lanl.gov>.
- [60] T. Jagemann, *Measurement of the Scintillation Light Quenching for Nuclear Recoils induced by Neutron Scattering in Detectors for Dark Matter Particles*, PhD thesis, TU München, 2004.
- [61] T. Jagemann *et al.*, *Astropart. Phys.* **26**, 269 (2006).
- [62] V. Mikhailik *et al.*, *Phys. Rev. B* **2004**, 205110 (69).
- [63] J. Ninković *et al.*, *Nucl. Instr. and Meth. A* **564**, 567 (2006).
- [64] J. W. Meadows, *Phys. Rev.* **157**, 1076 (1967).
- [65] R. B. Firestone, *Table of Isotopes* (John Wiley & Sons, Inc., 1996).
- [66] M. Stark, *Detektoren mit effizienter und schneller Phononensammlung für das CRESST-Experiment*, PhD thesis, TU München, 2005.
- [67] T. Jagemann, J. Jochum, and F. Feilitzsch, *Nucl. Instr. and Meth. A* **551**, 245 (2005).
- [68] M. Drosig, *Nucl. Instr. and Meth. A* **254**, 466 (1987).

- [69] C. Pastor, F. Benfranchi, B. Chambon, B. Cheynis, and D. Drain, Nucl. Instr. and Meth. A **227**, 87 (1984).
- [70] S. Roth, *Sputtered Tungsten Thin Films and Composite Detectors for the Application in the Dark Matter Experiments CRESST and EU-RECA*, Master's thesis, TU München, 2007, http://www.e15.physik.tu-muenchen.de/fileadmin/downloads/thesis/dipl/2007_Sabine_Roth.pdf.
- [71] C. Coppi *et al.*, Nucl. Instr. and Meth. A **559**, 396 (2006).
- [72] C. Isaila *et al.*, Nucl. Instr. and Meth. A **559**, 399 (2006).
- [73] W. Westphal *et al.*, Nucl. Instr. and Meth. A **559**, 372 (2006).
- [74] C. Isaila *et al.*, J. Low. Temp. Phys. **151**, 394 (2008).
- [75] J. Schnagl, *Entwicklung von Lichtdetektoren mit Phononendetektoren für das CRESST Experiment*, PhD thesis, TU München, 2001.
- [76] C. Ciemniak, PhD thesis, TU München, in preparation.
- [77] P. Huff, private communication.
- [78] J.-C. Lanfranchi *et al.*, arXiv:0810.0132 , Optical Materials, in Press.
- [79] C. Coppi *et al.*, to appear in the proceedings of Dark Energy and Dark Matter, Lyon, France, 7 - 11 July 2008.

Acknowledgments

In the first place, I want to thank Prof. Dr. Franz von Feilitzsch for giving me the possibility to do my Ph.D. at the physics department E15 and supporting me throughout my work. His enthusiasm together with the nice working atmosphere he has created in his group gave me always motivation also in the difficult moments of my work.

To Prof. Dr. Wolfgang Rau I am very grateful for his engagement as supervisor. He has introduced me to the very interesting field of dark matter and to the experimental techniques at the basis of this work. He always had time for helping and advising me and he kept doing that with interesting and useful discussion also from the other side of the ocean.

Dr. Walter Potzel was always there, ready to help when I needed help. He always found the time for a discussion about the several difficulties I had during my work. His advice was a precious help and his enthusiasm always contributed to my motivation. I am also deeply grateful to him for the careful reading of this thesis, often done in his free time.

I thank Dr. Jean-Côme Lanfranchi for his valuable contribution to this work, for his engagement in the installation of the cryostat and in the preparation of the experiment at the accelerator and for the help and support during the beamtimes. I also thank him for finding the time to read this work, contributing with his advice to make it better.

I was really lucky to have Christian Ciemniak as collaborator during my work. Working with him was very stimulating and his skills and insights contributed greatly to the success of our project.

I am deeply sad that I cannot tell Wolfgang Westphal how good it was to have him as colleague. His contribution to this work was fundamental in many aspects: starting with the detector that he made for the neutron scattering experiment, going on with the data analysis programs, and his many useful suggestions and discussions. He was always ready to help, contributing with his experience to solve problems of the most different kind: from the experimental setup to the data analysis to every kind of computer problems.

I thank Sebastian Pfister for his help during the installation of the cryostat and for the support for all computer problems. I was happy to share the office with Christian Isaila, with whom I had also many interesting and stimulating discussions. I thank all the other members of the group, that were always ready to share their experience and to give practical help. All together contributed to create a nice atmosphere that makes the work lighter.

To Marcel Kimmerle, Klemens Rottler, Stephan Scholl, Christof Sailer and Igor Usherov, from the CRESST group in Tübingen, many many thanks for their help during the beamtimes. Their support and experience helped a lot in solving the unexpected problems that appeared. Their presence was also fundamental in making the measurement periods a not too stressing time.

I thank the people of the CRESST group of the Max Planck Institute who were always available to answer my questions.

I thank Hermann Hagn for his invaluable help with all electronics problems, Harald Hess, Erich Seitz and Thomas Richter from our mechanical workshop who always managed to fit my projects into their busy schedules and Norbert Gärtner for being always there to help on technical questions that arise in the course of the laboratory work.

I want to thank all the people of the accelerator, for contributing to make my work there lighter and pleasant. In particular I thank Ludwig Beck, Rudi Lutter, Walter Carli and all the operators of the accelerator for their work and for their readiness to be helpful.

I thank Beatrice van Bellen, Alexandra Földner, Maria Bremberger and Sonja Kraus: their support is indispensable for the success of our work. In

particular, I want to thank Beatrice because, beyond her very efficient and useful professional help, she supported me also as friend.

È impossibile dire in poche parole quanto siano stati preziosi, anche per il successo di questo lavoro, i miei amici, sia quelli in Italia che quelli che ho avuto la fortuna di incontrare qui: in questi anni lontano da casa sono stati per me come una famiglia. In particolare ringrazio Chandra che con la sua saggezza e la sua visione positiva della vita mi ha spesso aiutata ad uscire dai momenti difficili. Un grazie speciale a Eleonora che ha saputo starmi così vicino nonostante la distanza che ci separa.

Grazie alla mia famiglia per avere sempre fiducia in me e per avermi sostenuta e incoraggiata nei momenti di difficoltà.

Infine voglio ringraziare di cuore Peter per la pazienza che ha avuto in questi mesi, in cui starmi accanto non è stato certo facile.